nature photonics

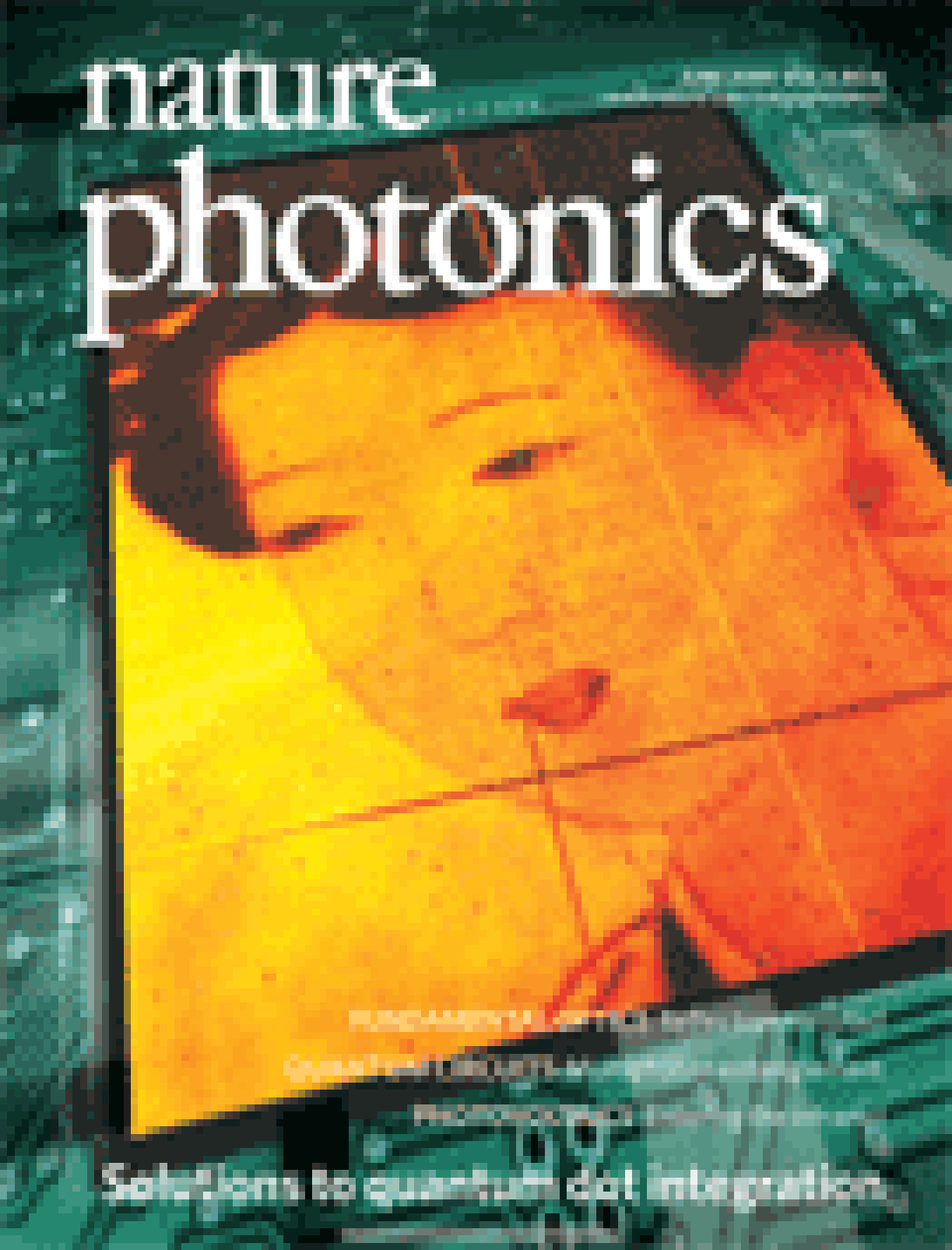

Solutions to quantum dot integration

nature photonics

ORIGINAL RESEARCH TYPESET BY Techset Composition Ltd, www.techset.co.uk
PRINTED BY Wyndeham Grange, www.wyndeham.co.uk

JUNE 2009 VOL 3 ISSUE 6

nature photonics

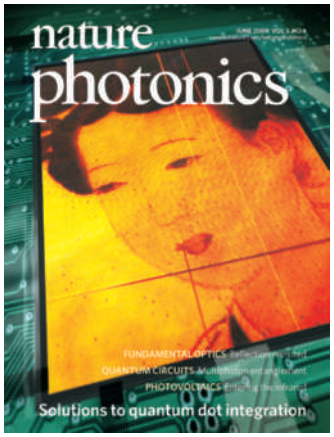

COVER IMAGE

An image from a yellow–red display made from colloidal quantum dots — light-emitting semiconductor nanocrystals held in an organic solution. The attraction of the technology for displays is that it is bright, potentially cheap to manufacture, does not require a backlight and suits use in very thin designs that can be scaled to large sizes.

Article p341;
News & Views p315

ON THE COVER

Fundamental optics
Reflection revisited
Letter p337

Quantum circuits
Multiphoton entanglement
Article p346;
News & Views p317

Photovoltaics
Entering the infrared
Progress Article p325

The Institute of Photonics and Optical Science, which has just opened at the University of Sydney, aims to combine world-class research with educational courses.
News & Views p320

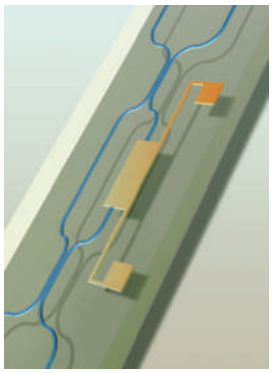

The ability to perform quantum computing on the chip-scale could be a step closer, thanks to the demonstration that an array of miniature waveguide interferometers can perform multiphoton entanglement.
Article p346;
News & Views p317

ARTICLES

PRODUCT FOCUS

INTERVIEW

nature publishing group

Nature Photonics (ISSN 1749-4885) is published monthly by Nature Publishing Group (Porters South, 4 Crinan Street, London N1 9XW, UK). Editorial Office: Chiyoda Building, 5-6th Floor, 2-37 Ichigayatamachi, Shinjuku-ku, Tokyo, 162-0843, Japan. Telephone: +81 (0)3 3267 8751. Fax: +81 (0)3 3267 8754. Email: naturephoton@nature.com. North American Advertising: *Nature Photonics*, 75 Varick Street, 9th Floor, New York, NY, 10013-1917, US. Telephone: +1 212 726 9200. Fax: +1 212 696 9006. European Advertising: *Nature Photonics*, Porters South, 4 Crinan Street, London N1 9XW, UK. Telephone: +44 (0)20 7833 4000. Fax: +44 (0)20 7843 4596. Asia-Pacific Advertising: *Nature Photonics*, Chiyoda Building, 5-6th Floor, 2-37 Ichigayatamachi, Shinjuku-ku, Tokyo, 162-0843, Japan. Telephone: +81 (0)3 3267 8754. Fax: +81 (0)3 3267 8746. New subscriptions/renewals/changes of address/back issues and all other customer service questions should be addressed to - North America: *Nature Photonics*, Subscriptions Department, PO Box 5054, Brentwood, TN 37024-5054, USA. Outside North America: Subscriptions Department, Brunel Road, Basingstoke, Hants. RG21 6XS, UK. Telephone: +44 (0)1256 329242; Fax: +44 (0)1256 812358: Nature Asia-Pacific, Chiyoda Building, 5-6th Floor, 2-37 Ichigayatamachi, Shinjuku-ku, Tokyo, 162-0843, Japan. Telephone +81 (0)3 3267 8751. Annual subscription rates: US/Canada US$3060, Canada add 5% GST (institutional/corporate), US$152, Canada add 5% GST (individual making personal payment); UK/Rest of World (excluding Europe and Japan) £1570 (institutional/corporate), £78 (individual making personal payment); Europe €2430 (institutional/corporate), €121 (individual making personal payment). Back issues: US/Canada $45, Canada add 5% GST; Rest of World: surface mail US$43, air mail US$45. *Nature Photonics* (ISSN 1749-4885) is published monthly by Nature Publishing Group, c/o Mercury Airfreight International Ltd, 365 Blair Road, Avenel, NJ 07001, USA. Periodicals postage is paid at Rahway NJ. Postmaster: send address changes to *Nature Photonics*, c/o Mercury Airfreight International, 365 Blair Road, Avenel, NJ 07001, USA. Reprints: *Nature Photonics* Reprints Department, Porters South, 4 Crinan Street, London N1 9XW, UK. Subscription information is available at the *Nature Photonics* homepage at http://www.nature.com/naturephotonics. Postmaster: send address changes to *Nature Photonics* Subscriptions Department, Brunel Road, Basingstoke, Hants. RG21 6XS, UK or *Nature Photonics* Subscriptions Department PO Box 5054, Brentwood, TN 37024-5054, USA.

The rise of colloidal quantum dots

This issue features a theme on colloidal quantum dots, bringing together primary research findings and overviews, along with articles on the commercialization of this technology.

It is a commonly held belief that a material's composition defines its optoelectronic properties. Although this is indeed often the case, when semiconductors are scaled down in size, they can behave very differently from their bulk counterparts. Indeed, quantum dots — semiconductor nanocrystals with diameters in the range 2–10 nm — show size-dependent optical properties due to the effect of quantum confinement. Perhaps the most striking of these properties is that the monochromatic light emission from quantum dots is not only highly efficient but can be tuned by simply changing their diameter.

Furthermore, suspending such quantum dots in an organic polymer solution allows them to be printed and poured like a photonic ink onto a substrate, opening an avenue to easy, low-cost fabrication. Combined with efficient, narrowband light emission, this means that these tiny suspended semiconductor dots are now being explored for cheap, bright LEDs in lighting and displays, fluorescent labels in biomedical imaging and broadband solar cells, to mention just a few applications.

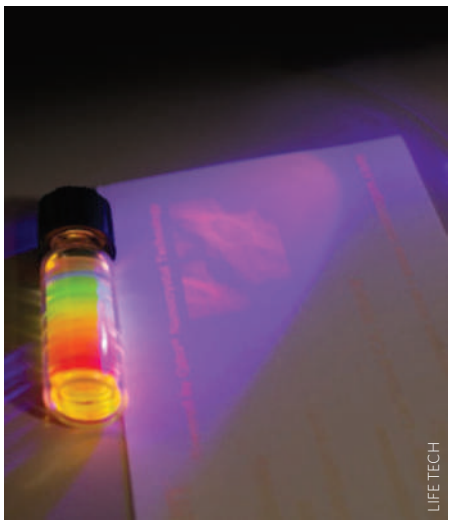

There are currently an impressive number of companies commercializing quantum dots and dot-based devices.

The June issue of *Nature Photonics* has a special theme on colloidal quantum dots, presenting the latest results from several research groups and commercial companies in this area. This theme gathers a collection of two primary research papers on a quantum dot LED display and an image sensor, a progress article on quantum dot photovoltaics, a News and Views article and an Out of the Lab piece charting commercialization of the technology. The compilation clearly demonstrates the great progress that colloidal quantum dots are making, not only in terms of device performance but also towards deployment in a wide variety of applications.

The LED is one of the devices in which quantum dots can be put into good use thanks to their ease of colour tunability, high brightness and narrow emission bandwidth. Nevertheless, large energy barriers for hole and electron injection into the quantum dot layer limit the device performance. On page 341, Kyung-Sang Cho and colleagues from the Samsung Advanced Institute of Technology demonstrate how the energy barriers can be overcome by using specific crosslinking and thermal annealing of the colloidal quantum dot layer and incorporating sol–gel-processed TiO_2 as the electron transport layer[1]. Their device shows a high luminance (12,380 cd m^{-2}), low turn-on voltage (1.9 V) and high power efficiency (2.41 lm W^{-1}). When incorporated into a display device with an active matrix backplane, the approach shows potential for high-performance, easy-to-fabricate, large-area displays and illumination sources.

On the other hand, colloidal quantum dots can also be used to create infrared photodiodes. This capability is detailed on page 332 of this issue by Rauch and colleagues from Siemens AG, University of Linz and Universität Karlsruhe, who have fabricated an array of inorganic–organic hybrid bulk-heterojunction photodiodes containing solution-processed PbS nanocrystalline quantum dots integrated with an amorphous silicon active matrix (a-Si AM) backplane[2]. The image sensor made from the photodiode array shows excellent performance for near-infrared detection up to 1.8 μm, with rectification ratios of ~6,000, minimum lifetimes of one year and external quantum efficiencies up to 51%.

What's interesting about the achievements of these two groups is that they demonstrate that integration of colloidal quantum dot optoelectronics with silicon backplane electronics is practical, which is of great importance if the technology is going to find its way into products.

The findings are put into context by Seth Coe-Sullivan from the quantum dot start-up firm QD Vision in a News and Views article on page 315, where he shares his thoughts on the role played by colloidal quantum dots in vision and sensing in particular, and on the challenges that remain[3].

Indeed, a look at the Out of the Lab article on page 307 immediately tells us that colloidal quantum dot technology has already garnered great attention in the world of commercialization[4]. The race to bring quantum dots to the market in fact started back in the early 2000s, and there are currently an impressive number of companies commercializing quantum dots and dot-based devices.

Firms are now able to mass-produce quantum dots with accurate dimensions and a variety of coatings, and are busy exploring their potential in applications ranging from displays and biomedical imaging to photovoltaics and quantum inks for fighting currency counterfeiting.

The prospects for solution-processed photovoltaics based on colloidal quantum dots are outlined in this month's Progress Article by Edward Sargent from the University of Toronto[5]. As he explains on page 325, the attraction of the technology is that it promises to reduce the cost per area of solar cells and extend their absorption wavelength to infrared region where half of the solar energy lies.

One thing is for sure: the research behind colloidal quantum dots is growing and sooner rather than later will be evident in the world around us in the form of brighter, more colourful displays, energy-efficient lighting and custom-designed fluorescent tags for biological imaging. ❐

References

1. Cho, K.-S. *et al. Nature Photon.* **3,** 341–345 (2009).
2. Rauch, T. *et al. Nature Photon.* **3,** 332–336 (2009).
3. Coe-Sullivan, S. *Nature Photon.* **3,** 315–316 (2009).
4. Graham-Rowe, D. *Nature Photon.* **3,** 307–309 (2009).
5. Sargent, E. H. *Nature Photon.* **3,** 325–331 (2009).

Assessing the viability of solar cells

To the Editor — Economical solar energy has been chosen by the United States National Academy of Engineering as one of the 14 engineering grand challenges facing humans in the twenty-first century[1]. To evaluate the economic viability of a given photovoltaic cell technology, the photovoltaic community commonly uses a convenient figure of merit known as cost (dollars) per peak watt of electricity generated, $\$/W_{peak}$. I would like to explain to readers some reasons why I feel that this term is flawed and alternative figure of merits are required for realistic assessment of this technology.

First, the $\$/W_{peak}$ figure of merit is predicated on the assumption that instantaneous peak power, W_{peak}, is the best way to determine photovoltaic cell performance. However, the terrestrial solar spectrum, irradiance and temperature fluctuate strongly from sunrise to sunset and thus so does the actual power output of a photovoltaic cell. The instantaneous peak power, W_{peak}, is typically measured indoors at a temperature of 25 °C using a lamp to provide a constant perpendicular irradiance of 1,000 W m^{-2} and a spectrum that specifically mimics the atmospheric condition of air mass 1.5 global (AM1.5G). But photovoltaic cells installed around the world rarely operate under precisely these three simultaneous conditions. Therefore, I believe that cells should be tested to determine average power, W_{avg}, produced over at least an 8-hour period with a fluctuating spectrum, irradiance and temperature mimicking a complete sunrise-to-sunset operating envelope. More to the point, cells and modules should be designed for site-specific application and then tested under typical site-specific conditions.

Second, high-purity photovoltaic-grade semiconductors, which constitute our best photovoltaic cell technologies, are a precious resource that must be conserved. The $\$/W_{peak}$ figure of merit provides no direct consideration of material use. Solar photovoltaic (plus solar thermal) energy accounted for only 0.02% of the net generated electricity in the United States in the year 2008 (ref. 2). If we desire to radically increase our use of solar photovoltaic energy worldwide, a massive amount of active photovoltaic and inactive auxiliary material will be required.

To receive the maximum benefit from our resources (solar energy and semiconductor material), it makes sense to develop photovoltaic cells that produce the highest average power during the entire period between sunrise and sunset (rather than highest instantaneous peak power) with the smallest amount of material (m^3) at the lowest cost. This gives rise to a new figure of merit for a photovoltaic cell of $W_{avg}/(m^3\ \$)$.

With wide-scale manufacturing and deployment of photovoltaic modules comes not just economic viability but environmental responsibility. One of the primary attributes of photovoltaic energy is that it is an environmentally friendly approach, without the pollution of fossil fuels or the toxicity of nuclear waste. Therefore, it is inappropriate to develop photovoltaic cells containing potent carcinogens such as arsenic and cadmium (for example GaAs and CdTe cells) while marketing this as a green technology. The European Union developed the restriction of hazardous substances (RoHS) directive in July 2006. One of the goals of the RoHS movement is to reduce cadmium[3]. The California Environmental Protection Agency's Office of Environmental Health Hazard Assessment[4] listed GaAs as a cancer-causing material in August 2008. There are concerns about mercury in fish and lead in consumer electronics. I believe that we should also be concerned about development and large-scale deployment of photovoltaic modules based on serious toxins such as arsenic and cadmium.

Unlike coal and nuclear power plants, which must be located remotely and connected to long-distance electricity transmission lines plagued by resistive losses and high cost, photovoltaic modules are ideally suited for our rooftops and for interfacing with the local electric grid. While flying in and out of various urban airports around the world, a stark observation is that solar photons have travelled ~150 million kilometres only to find millions of barren rooftops. This situation needs to change. ❐

References

1. http://www.engineeringchallenges.org/
2. http://www.eia.doe.gov/cneaf/electricity/epm/tablees1b.html
3. http://www.rohs.gov.uk/
4. http://www.oehha.ca.gov/prop65/prop65_list/080108list.html

Alexander P. Kirk
Purdue University, School of Materials Engineering, 701 West Stadium Avenue, West Lafayette, Indiana 47907, USA.
e-mail: apkirk@purdue.edu

From dots to devices

Quantum dots — semiconductor nanocrystals that have custom designable optical properties — are opening up opportunities in the bio-imaging, display and lighting sectors, reports **Duncan Graham-Rowe**.

The term 'quantum dot' was first coined by Yale physicist Mark Reed in the late 1980s to describe the strange way in which extremely small semiconductor crystals — typically measuring between 2 and 10 nanometres, or about 50 atoms in size — seem to take on the characteristic properties of both bulk materials and discrete atoms. First discovered by Louis E. Brus at Bell Labs a few years previously, quantum dots can be made to absorb light efficiently and respond by emitting very specific wavelengths. But crucially, what makes them so intriguing and alluring is that it is their size and not their material composition that determines the colour of this light.

"It's spectral engineering," says Jason Hartlove, CEO and President of Nanosys in Palo Alto, California, one of several companies that is selling quantum dots. This scaling effect allows you to tune a quantum dot's optical properties to suit a set of specific needs. And because quantum dots can be suspended in a solution (often an organic polymer) they can be injected, painted or stamped like a photonic ink using low-cost printing or coating techniques. In light of this, quantum dots hold huge potential for a wide range of applications, from biomedical imaging, lighting and display technologies to low-cost solar cells and security tagging.

The ability to grow quantum dots in solution means they could be fabcricated cheaply rather than requiring complex and expensive semiconductor growth techniques.

The unusual behaviour of quantum dots results from a phenomenon called quantum confinement. This occurs when semiconductor crystals are grown to be so small that their size falls within the dimensions of a critical quantum limit known as the exciton Bohr radius. "Things start to get interesting at about 10 nm," says Seth Coe-Sullivan, co-founder and chief technology officer of QD Vision, a start-up from Massachusetts Institute of Technology based in Watertown, USA. The firm has received more than $20 million in venture capital funding since its formation in 2004 to develop quantum-dot-based displays. According to Sullivan, what makes quantum dots interesting is that their bandgap becomes dependent on the size of the crystal.

It's a bizarre phenomenon, says Clint Ballinger, CEO of Evident Technologies in Troy, New York, which was set up by three Lockheed Martin scientists in 2000. Evident Technologies has raised more than $23 million in venture capital funding helping it to become one of the earliest companies to start selling quantum dots in 2003. "If you take a bulk semiconductor, it is what it is," he says. Its optical properties are defined by the material from which it is made. "A nanocrystal is the exact same material, but as a crystal of just a few atoms across you get these weird properties because of quantum confinement."

A reason for this is that in a bulk material the electron clouds are shared, resulting in a higher density of states, says Ballinger. But in a quantum dot the physical confinement constrains the energy levels of the electrons to the point that they become discrete and so can no longer be treated as continuous. As a result, when excited by either a photon or an electron they will give off this energy as a discrete energy signature in the form of a photon of a specific wavelength.

This is particularly useful not just because the emission is tunable and narrow, but also because the mechanism has such high quantum efficiencies. In the laboratory these efficiencies are approaching 100%, says Coe-Sullivan, meaning that for optical excitation, every photon absorbed by a dot results in a lower-energy (longer-wavelength) photon being emitted.

Another advantageous property of quantum dots is that they can have a broad band of absorption. Indeed, this is one reason that they are attractive for biomedical imaging applications: it makes their optical excitation easier, as no careful spectral alignment with a laser source is required.

Life Technologies, a large biotechnology company in Eugene, Oregon, is using

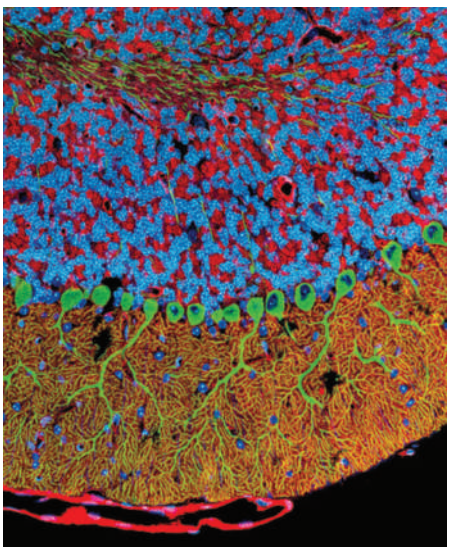

LIFE TECHNOLOGIES

Quantum dots are proving a popular alternative to fluorescent dyes for labelling cells.

One of the biggest potential applications for quantum dots is in LEDs for highly efficient lighting.

quantum dots instead of the more traditional organic dyes for a range of optical screening, labelling and imaging technologies. With a sales record of $3.5 billion and employing more than 9,500 people, Life Technologies (formerly Invitrogen) acquired Quantum Dot Corporation, the company that pioneered the commercialization of the technology in 2005 and now has several quantum-dot-based imaging technologies undergoing clinical trials.

The challenge with this sort of application is to treat the quantum dots to make them biocompatible, says Bob Beltz, senior manager of product development for Life Technologies. The firm has developed a way of coating quantum dots with a biocompatible polymer that allows them to be suspended in blood. It has also developed ways of binding certain molecules to these coatings, such as antibodies, which allow them to be used to target certain types of cell. Then, using techniques such as flow cytometry, the cells can be identified by illuminating them with laser light and monitoring the wavelength of the emissions given off by the quantum dots. Similar approaches are also being used to target cancer cells and help surgeons to ensure that every last cell of a tumour is removed, says Beltz.

In many respects this is similar to how traditional fluorescent dyes are used, says Beltz. "But the key advantage is the brightness of the quantum dots and the fact that they can be excited by a common lighting source," he says. Each conventional dye needs a different laser source to produce the specific wavelength it needs to fluoresce, whereas different quantum dots can be illuminated with one single source. Another advantage with quantum dots is that they are much more stable and so tend not to bleach (that is, lose their emission) quickly.

One of the challenges of using quantum dots in any application is the fact that traditionally they have been made using cadmium-based semiconductors, such as cadmium selenide and cadmium sulphide. With regulatory authorities across the world increasingly banning the use of heavy metals in many goods, there is now a move towards developing so-called cad-free dots instead. Pretty much all companies are working on such alternatives, but, as ever, there are trade-offs, says Vicki Singer, head of global out-licensing for Life Technologies. "It's more difficult to have the same combination of brightness and stability in a cad-free material," she explains.

Other markets for quantum dots include their use as semiconductor materials in traditional electronics, such as for extremely high-density solid-state memory chips, which is one application Nanosys is working on with partners such as Intel, Sharp and NTT Docomo, the Japanese mobile phone company. Similarly, Evident Technologies already has an established market, with revenues of US$4 million from last year alone, selling quantum-dot LEDs in the form of lighting, such as Christmas decorations, or for vehicle indicator lights, says Ballinger.

Although these market drives are carving out serious inroads in the commercialization of the technology, quantum dots are unlikely to enter the mainstream consumer markets until new methods are developed to produce them in greater quantities. "You can normally only make small amounts, literally just milligrams of the material," says Torsten Schanze, operations manager of Nanoco Technologies, a company that was spun out of research at Manchester University, in the United Kingdom. Because of this, the technology has only been open to markets such as biomedical imaging that require small amounts of the stuff.

But Nanoco hopes to change all that with a technique for mass-producing quantum dots, says Schanze. Quantum dots can be made using a variety of epitaxial processes (growing semiconductors layer by layer in a vacuum chamber) but a cheaper and promising approach is to use a colloidal suspension. This is where precursor compounds for making the dots are dissolved in a high-temperature solution of an organic solvent. At a high enough temperature the precursors transform into monomers and become supersaturated. At this stage nanocrystals begin to nucleate and grow. But these high-temperature conditions can be difficult to control precisely and do not lend themselves to mass production, says Schanze.

"The crystal will grow from 2 to 10 nm in as little as 30 seconds," he says. This means if you want to grow a small dot to produce blue light you need to be able to stop the reaction very quickly. But putting the brakes on involves cooling the solution, which at high temperatures is hard to do rapidly. Nanoco's patented molecular seeding approach, the details of which it will not divulge, operates at much lower temperatures, typically 70 °C as opposed to hundreds of degrees. "By growing the crystal at a lower temperature they grow much slower," says Schanze. Taking hours instead of seconds means that Nanoco has a much tighter control over their growth, he says. By exciting the nanocrystals and measuring their emissions as they grow it is possible to monitor the growth and halt the reaction with greater precision.

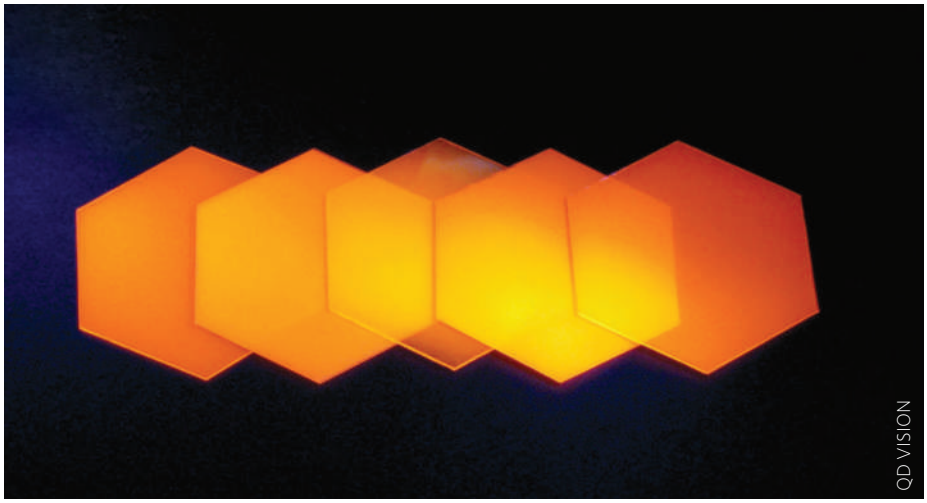

In the future, the hope is to use quantum dots to create flat-panel displays with superior colour and efficiency compared with LEDs.

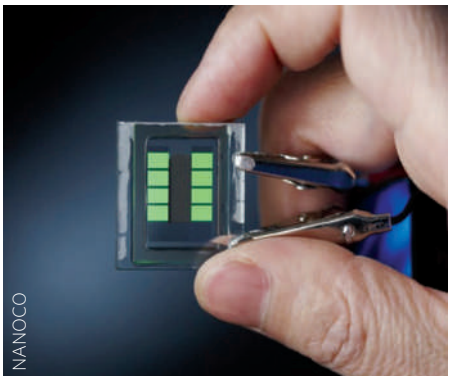

The ease of fabrication of colloidal quantum-dot light emitters is a great attraction of the technology.

"By the end of the year we'll be making batches approaching the kilogram range," says Schanze.

The company is hoping to have a manufacturing plant capable of even larger yields up and running in Japan within the next three years. "With this kind of mass production, consumer products start to become feasible," says Schanze.

Precisely what products will appear first is still open to question. The two front runners are general lighting, to produce quantum-dot-enhanced LEDs (or QD-LEDs) to replace incandescent bulbs, and display technologies. According to Coe-Sullivan, QD Vision is hoping to launch lighting products by the end of the year. The potential here is huge, he says. "People like incandescent light bulbs because they produce the same quality of light as the Sun." But because it's such an inefficient technology, many nations are phasing out these bulbs in favour of compact fluorescent light bulbs which are up to five times as efficient. The trade off with compact fluorescent light is the poor colour quality of light, says Coe-Sullivan. But QD-LED offers the best of both worlds.

"You use a blue 450-nm-emitting LED and add red and green quantum dots," says Schanze. The blue light is used to produce the blue element of the white light while also exciting the dots and causing them to emit red and green light of very specific wavelengths. The result of the colour mixing of the red, green and blue is a white light with very good colour rendering.

It's basically like using quantum dots as a phosphor, says Ballinger, but with a much greater quality of light because of the narrow band of emissions produced by the quantum dots.

The same approach is being used to produce white backlights for displays, where QD-LEDs not only improve the light quality but also improve the power consumption efficiency by at least 50%.

"But the holy grail in quantum-dot displays is to throw away the entire LCD [liquid crystal display]," says Coe-Sullivan. Instead, the aim is to build a display based on RGB emissive dots that are excited electrically, he says. Because of the narrowband emissions that quantum dots offer, such displays would give better colour quality and better contrast than is currently possible with any display. "And the 'off' state would be much blacker," says Coe-Sullivan.

QD Vision is currently collaborating with major manufacturers to develop such displays, but this technology is much further off. It would probably take three years to get prototypes working and up to seven years to bring them to market. Even so, when they do arrive it is feasible to expect these devices to be as much as 10 times as efficient as existing LCD displays, he says.

Another advantage of using quantum dots in lighting devices and displays is the ease with which they can be manufactured. Unlike traditional semiconductors, which require extremely expensive clean-room fabrication facilities, colloidal quantum dots (where the semiconductor nanocrystals are suspended in a polymer solution) can be printed at a fraction of the cost. Because of this, ironically, it may take longer than you might expect for the technology to be wholeheartedly adopted, says Schanze. With companies having already spent hundreds of millions of dollars on silicon clean rooms, it will take some time to convince them to look at alternatives, he says.

By the end of the year we'll be making batches approaching the kilogram range.

But when it comes this feature will unleash a range of other printing-related applications such as photonic ink. Evident Technologies, for example, already produces a photonic paint that appears brown to the naked eye but can emit specific spectral signatures when illuminated with the right light source. Similarly, Evident has developed quantum dots that can emit in the infrared: according to Ballinger, this opens up a whole range of military and security applications, such as glow sticks, target markers or for tagging documents. Some companies are even looking into these kinds of quantum inks to help fight counterfeiting of currency or drugs, says Life Technologies' Singer.

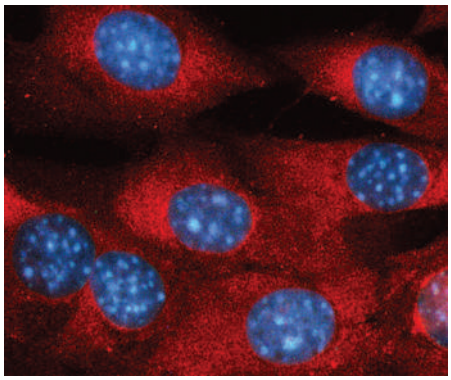

Colloidal quantum dots can be attached to the peptides and antibodies that recognize specific cell types, allowing targeted biological imaging.

One of the least explored but potentially most promising applications, at least in terms of benefit to humanity, is the energy market. Just about all companies involved in quantum dots are now turning their attention towards their use in photovoltaic cells. Again, one reason for this is the potential saving to be made from printing such cells, says Nanosys's Hartlove. In this case the dots are simply designed to work in reverse, producing one or many excitons for each high-energy photon absorbed. Although in some respects such photovoltaic cells are working in the same manner as traditional semiconductor cells, the advantage of using quantum dots is that their tunability makes it possible to tap the high-energy ultraviolet light as well as lower-energy infrared light. In contrast, traditional silicon solar cells can only operate in the visible light range, says Ballinger.

But for any commercially viable application to stand a real chance of taking off, there remains one challenge in particular for quantum dots — stability. Whether they are used in lighting, displays, ink or photovoltaic cells, quantum dots need to be able to last. According to Hartlove, existing dots have a life cycle of about 10,000 hours, which is pretty good. "But it's still not good enough: we need to be getting 50,000 hours," he says. The good news is that this should be achieved within the year, he says. And when this happens we can expect a deluge of dots, whose potential, unlike their physical dimensions, seems to be massive.

Duncan Graham-Rowe is a freelance science and technology journalist based in Brighton, UK.
e-mail: duncangr@gmail.com

METAMATERIALS

Dual guiding

Nano Lett. doi: 10.1021/nl900550j (2009)

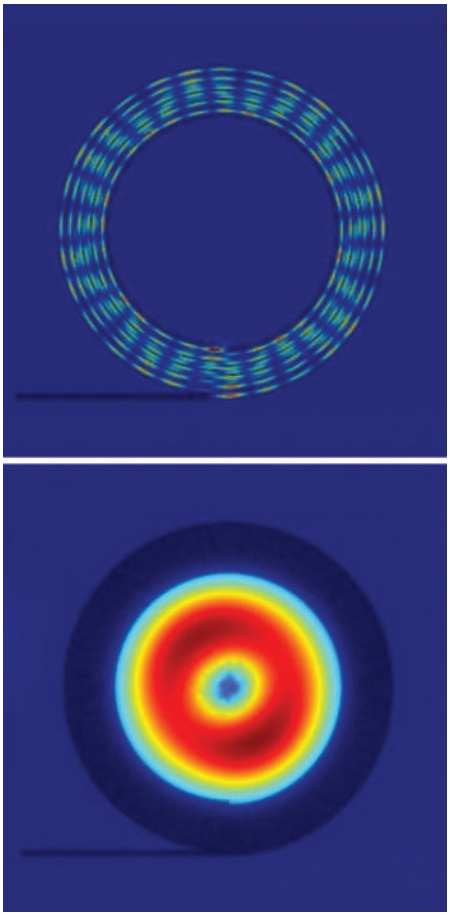

Waveguides come in a variety of shapes and sizes. They include classical solid-core waveguides used in communication devices, low-loss single-mode fibres, and surface plasmon waveguides that can transmit subwavelength information. A team of scientists in Germany and the United States has now proposed a new type of waveguide that combines surface plasmon and classical waveguiding.

Elliot Smith and colleagues have designed a waveguide that is made up of alternating layers of silver and aluminium oxide, which form a plasmonic metamaterial fibre. The waveguide is hollow with an inner radius of 2 μm and a cladding thickness of about 500 nm. Depending on the wavelength of light used (ultraviolet or infrared, for example) and the composition of the metamaterial, simulations show that light can be propagated through the fibre either by surface-plasmon-mediated mechanisms through the waveguide's cladding, or by classical waveguiding through the core. Moreover, by introducing a gas or liquid into the waveguide core, these two different types of modes could be coupled together — something that, the authors hypothesize, could prove useful for sensing applications.

METAMATERIALS

Self-collimation

Phys. Rev. Lett. **102,** 133902 (2009)

In the field of metamaterials, scientists have now shown that a specially engineered negative-index material can be made to strongly collimate light over significant distances. Using a structure made up of alternating layers of photonic crystal and air, it is possible to preserve the shape and size of a beam of light over a distance that is 1,000 times as long as the input wavelength.

The design put forward by Mocella *et al.* consists of a two-dimensional silicon-based photonic crystal, which contains airholes arranged in a hexagonal lattice and lies on a silicon-on-insulator wafer. Light is vertically confined within the structure. By repeatedly alternating striped layers of photonic crystal and air, and slightly modifying the length of each photonic crystal layer, the structure can be engineered to have a nearly zero volume-average refractive index. This near-zero value maximizes light transmission while optimizing coupling of the evanescent portion of the waves. The outcome is that beams are essentially refocused in every stripe as they travel along, becoming strongly self-collimated. This is borne out through experiment: Mocella and colleagues offer a striking demonstration that light beams (of wavelength 1,550 nm) remain well collimated over the entire 2 mm length of their heterostructure sample, with a beam width of about 3 μm.

NANOPHOTONICS

Merry-go-round

Opt. Express **17,** 6230–6238 (2009)

Whispering gallery modes (WGMs) arise when light is confined to a circular volume under certain conditions. But what is perhaps less well known is that a nanoparticle can also be attracted to WGM structures, and can be drawn in so that it gently orbits a WGM ring. In previous studies, biological particles in solution were found to bind together 100 times more when placed near a toroidal WGM structure than would be expected from diffusion and convective transport theory alone. Scientists have now further investigated this effect.

The work published by Arnold *et al.* shows that a WGM toroid generates attractive photonic forces that hold nearby nanoparticles in orbit. Using a silica microsphere with a 53 μm radius that is excited into a WGM with a quality factor of about one million, the researchers observe 140-nm-diameter polystyrene nanoparticles to become trapped in orbit for hundreds of seconds, circumnavigating at a rate of 2.6 μm s^{-1}, for an initial optical power of just 32 μW. When the incident power is reduced to 7.3 μW, particles are disengaged from orbit within 10 seconds.

NEMS TECHNOLOGY

Optics all the way

Nature Nanotech. doi:10.1038/nnano.2009.92 (2009)

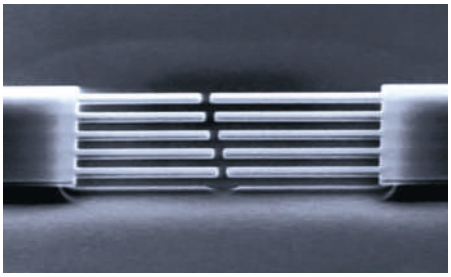

Nanoelectromechanical systems (NEMS) promise to revolutionize measurements of extremely weak forces and extremely small displacements. At the heart of these devices is a nanocantilever — similar to a miniature diving board — that deflects under an applied force. At present NEMS mainly use electrical methods for device operation, but optical methods offer better sensitivity and bandwidth.

Now, Mo Li and colleagues have taken a great step forward by demonstrating the integration of nanocantilevers onto a silicon photonic chip with a non-interferometric, all-optical measurement and read-out scheme. Their device consists of a pair of end-to-end coupled cantilevers that form part of a photonic waveguide, with a nanoscale gap separating the two. The cantilevers are 3 μm long and separated by 200 nm. Laser light passing through the first cantilever waveguide tunnels through the gap and is collected by the receiving cantilever waveguide. Any motion of the cantilever, caused by an external force, modulates the total transmission through the circuit and is detected as a transmitted optical signal. The approach is promising as it does not require a coherent light source, making the approach more feasible for on-chip use and reducing the overall device footprint. Conceivably the scheme could be extended to include several cantilever pairs.

LIQUID CRYSTALS

Beam steering

Appl. Opt. **48,** 1721–1726 (2009)

In phased array optics, the phase of light waves being transmitted or reflected is controlled by an array of adjustable elements. Phased arrays made from liquid crystals show particular promise for beam steering, but the response time of conventional nematic-based devices is typically slow. Researchers in Colorado, USA, have come up with a faster, more efficient beam-steering system that is based on ferroelectric liquid crystal (FLC) spatial light modulators and offers a 200 μs response time.

The advance in beam steering comes through the use of recently developed FLC-based spatial light modulators (SLMs), which offer continuous analog phase modulation, as opposed to traditional FLC-based SLMs, which are inherently binary. The Colorado device allows 700 distinguishable beam-steering angles to be achieved, as well as a much faster response time. The FLCs used are high tilt (with an 82° optic-axis switching), offering nearly full 360° phase modulation. The FLC pixel geometry — created by etching a pattern into an indium tin oxide coating on a glass plate — consists of 32 individual transparent pixel electrodes, each about 10 mm long and 300 μm wide, with a 310 μm pitch. With this new fast beam-steering scheme, the stage is set for compact liquid-crystal-on-silicon optical phased arrays.

QUANTUM DOTS

Plenty to gain

Phys. Rev. Lett. **102,** 127404 (2009)

Although one-dimensional quantum wells can amplify light, theory suggests that the three-dimensional confinement offered by quantum dots should improve performance. But the past two decades of work seemed to suggest that optical gain was not possible with particles smaller than 2.3 nm.

Now research from Canadian scientists looks set to change this view. The team apply a technique to the quantum dot known as state-resolved optical pumping, in which the wavelength of the pump pulse is tuned into resonance with specific initial excitonic (electron–hole) states. It turns out that in previous experiments, which were done without such state-resolved pumping, the conditions were ripe for masking the system's true optical gain. What Cooney *et al.* show is that gain is intrinsic to quantum dots and is independent of their size, verifying longstanding theoretical predictions. The authors have shown they can spectroscopically prescribe specific single and multi-excitonic states that can create, block and ultimately control the gain spectra of quantum dots.

LITHOGRAPHY

RAPID progress

Science doi:10.1126/science.1168996 (2009)

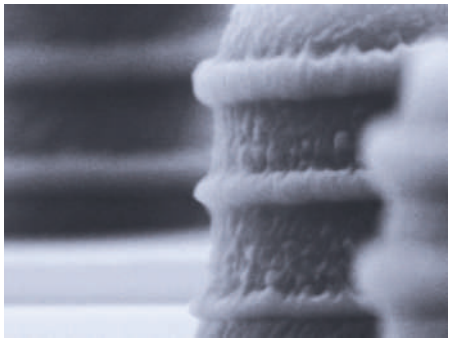

In conventional photolithography, diffraction limits the resolution to about one-quarter of the wavelength of the light used. Now Linjie Li and co-workers at the University of Maryland have reported a new technique, RAPID (resolution augmentation through photoinduced deactivation) lithography, which offers a resolution of one-twentieth of the wavelength, and the ability to produce features as small as 40 nm using 800-nm-wavelength light.

One pulsed laser beam is used to initiate polymerization in a photoresist (through the absorption of multiple photons) and a second continuous-wave beam is used to turn it off (through the absorption of a single photon). By shaping the phase of the deactivation beam spatially, the authors can fabricate features with varying resolution along the beam axis that are far smaller than the incident wavelength. Key to the success of this approach is the choice of a suitable photoinitiator — a compound that controls the polymerization process — to ensure that the deactivation beam actually inhibits polymerization instead of enhancing it. Because polymerization can be turned on with femtosecond-long pulses and off with much longer pulses, the technique can be performed using just a single ultrafast laser. The hope is that RAPID lithography could be used to create arrays of two- and three-dimensional optical structures with ultrasmall features.

IMAGING

Shrinking zooms

Opt. Express **17,** 6118–6127 (2009)

Zoom lenses are immensely popular and offer photographers great versatility. The problem is that the design of traditional zoom lenses introduces defocus and variations in optical aberrations that need correcting. Defocus is overcome by the use of a moving lens (a compensator), and additional lenses are used to overcome aberration. But by introducing extra elements to solve these issues, it becomes harder to miniaturize the zoom lens, something that is becoming increasingly important for devices such as mobile phones.

Mads Demenikov and co-workers' analysis of zoom lenses suggests that by making the image sensor size smaller and extending the depth of field, the size of zoom lenses can in principle be reduced considerably. Using ray tracing, they describe how intelligent use of a miniaturized detector array and a wavefront coding technique could produce a zoom lens that would be just 10 mm long, yet have a zoom factor of 2.3. This represents a reduction in size of three orders of magnitude compared with the equivalent 35 mm film technology. Although still at the design stage, the work could advance miniature camera technology.

MEDICAL OPTICS

Brain wave

Science **324,** 354–359 (2009)

Parkinson's disease is a debilitating brain disorder that causes muscle rigidity, tremors and movement problems. Deep brain stimulation (DBS) is used to treat Parkinson's disease, but its therapeutic mechanisms are not well understood, mainly because it is unclear which brain circuitry is involved in the treatment. Stanford University researchers are using optical technology to pinpoint the exact circuits involved.

Typically, electrical currents are used for DBS. But Viviana Gradinaru and colleagues take a different tack and use light. First, they genetically engineer the brain neurons of rats that are afflicted with Parkinson's so that they either fire or don't fire when exposed to light. Second, they use an optical delivery system — fibre optics and laser diodes — to deliver light into the rat brains. With this combination, different sections of the diseased brain circuit can be probed one at a time, with a millisecond response. Gradinaru *et al.* find that a region known as the subthalamic nucleus, a small lens-shaped part of the basal ganglia system, is a direct target of DBS in Parkinson's therapy. Although a cure is some way off, and treatment is extraordinarily complex, studies like this are helping to shed new light on this disease.

METROLOGY

Combs rule

The ability to measure distances with high precision is of fundamental importance. Femtosecond optical frequency combs offer an intriguing solution to the problem and could prove invaluable in space satellite missions of the future.

Seung-Woo Kim

Length is a basic physical quantity and its precise measurement is of fundamental significance in science and technology. The ability to determine the absolute distance to an object — ranging — is important for applications such as large-scale manufacturing and future space satellite missions involving tight formation-flying, where fast, accurate measurements of distance are critical for maintaining the relative pointing and position of individual satellites. Reporting on page 351 of this issue[1], researchers at the National Institute of Standards and Technology in the United States describe a laser ranging system that offers a unique combination of length precision, recording speed and large measurement range.

Distance measurement has come on in leaps and bounds since Albert A. Michelson first proposed using the wavelength of light as a ruler in 1887. Today, optical interferometers are commonly used to measure distances with an accuracy better than an optical wavelength; indeed, in extreme cases, such as gravitational wave detection, which calls for ultra-sensitivity, the accuracy can be many orders of magnitude below the wavelength. Figure 1 summarizes key milestones in the development of optical interferometers. In 1983, the SI definition of a metre was redefined as the distance travelled by light in vacuum during 1/299,792,458th of a second, with the consequence that the wavelength of any optical radiation used in length metrology can be most precisely determined by calibrating its frequency with respect to the time standard. The current SI definition of time states that the second is 9,192,631,770 periods of the radiation emitted from the transition between the two hyperfine levels of the ground state of a caesium-133 atom. But because optical frequencies are several hundreds of terahertz, their calibration with reference to the microwave-frequency caesium clock has presented considerable challenges, until the recent advent of clockwork making use of the frequency comb of a mode-locked femtosecond laser.

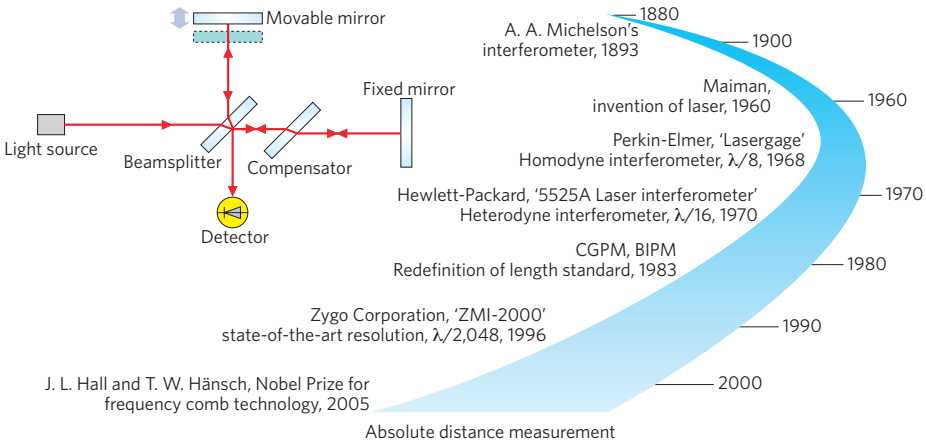

Figure 1 | Milestones in the development of optical interferometers for distance measurements. Michelson's interferometer first used red light emitted from a cadmium-isotope lamp to measure the standard metre. (Inset: the configuration of Michelson's interferometer used to measure the metre in 1983.) Nowadays, helium–neon lasers are used extensively in commercial interferometer systems to measure distances over ranges larger than a few tens of metres with subwavelength precision. But it is the recent advent of femtosecond lasers that is paving the way for innovative ways of measuring distance based on the frequency comb technology. CGPM, General Conference on Weights and Measures; BIPM, International Bureau of Weights and Measures.

Generally speaking, laser ranging determines the phase shift of a signal after it has travelled a certain distance. Conventional laser interferometry techniques use continuous-wave lasers to measure the phase of optical wavelengths to attain subwavelength-resolution over ranges exceeding a few tens of metres. But measurements are limited to relative range changes (it is not possible to determine directly the absolute value of the distance being measured), meaning that this type of approach yields a small ambiguity range (range window) of just half the wavelength used. Laser radar (LIDAR) techniques, on the other hand, measure distance through pulsed or radiofrequency-modulated waveforms. Such systems offer large measuring ranges but poorer resolution (50–100 μm).

In pursuit of the best of both worlds — larger ambiguity range and good resolution — multiple wavelengths can be combined to generate a longer 'synthetic wavelength'. Unfortunately, this requires either a tunable laser source or multiple laser sources to generate stable, accurate optical wavelengths over a wide spectral range. As such, the accuracy of absolute distance measurements is greatly affected by the individual precision of the wavelengths used.

The recent advent of femtosecond lasers has heralded metrology breakthroughs. First, it has led to the practical realization of the current international definition of the metre that was established in 1983, making it possible to bridge the gap between laser frequencies and the microwave time standard. Second, it has paved the way for absolute distance measurements involving versatile new measuring principles based on frequency combs as precision rulers.

A frequency comb is a series of multiple optical modes that are equally spaced in frequency, with each mode offering excellent absolute frequency accuracy along with an extremely narrow linewidth. Since early

work by Minoshima *et al.*[2] that used higher harmonics of a femtosecond laser to extend the ambiguity range to a few hundred metres, combs have been incorporated into precision-ranging systems in various ways. In particular, the comb output has been used directly in several experiments to take advantage of its coherence in both the radiofrequency and optical domains[3]. Other research has included time-of-flight proposals that use pulse repetition rate control combined with low-coherence pulse interferometry[4], and dual-wavelength sources produced using combs that generate synthetic wavelengths from tens of micrometres to several metres[5].

Buildling on this and other work, Ian Coddington and colleagues now demonstrate a new comb-based LIDAR technique[1]. Their approach combines the advantages of both time-of-flight and interferometric approaches to provide absolute distance measurements simultaneously from multiple reflectors and at low power. They use a pair of stabilized broadband, fibre-based, femtosecond-laser frequency combs with pulse trains of slightly different repetition rates (100.021 and 100.016 MHz). One comb acts as the 'signal' source and samples a distance path defined by reflections off a target and reference plane; the other acts as a broadband local oscillator and recovers range information in an approach equivalent to linear optical sampling. In this way, pulse time-of-flight information can be obtained, yielding 3-μm distance precision with a 1.5-m ambiguity range in 200 μs. Through the optical carrier phase, the measurement accuracy improves to better than 5 nm in 60 ms, and through the radiofrequency phase the ambiguity range can be extended to 30 km, potentially providing ranging with an accuracy of 2 parts in 10^{13} at long distances.

Unlike standard multi-wavelength interferometry methods, the technique devised by Coddington *et al.* is robust to systematic shifts due to, for example, spurious reflections, which have been a significant source of error in other experiments. Furthermore, there are no assumptions about the initial pulse shape. As such, the work offers a sound technological underpinning to the next generation of formation-flying satellite missions and their metrological needs. At present, we are a long way off launching such a mission, as much engineering will be needed to space-qualify such a system. Although optical frequency combs have been suggested for use in space missions using optical clocks, existing combs remain mostly laboratory instruments and will require further development before they can go up in space. Nevertheless, this latest comb-based advance boasts a range of powerful features that existing techniques just cannot offer. ❐

Seung-Woo Kim is in the Department of Mechanical Engineering, Korea Advanced Institute of Science and Technology (KAIST), Science Town, Daejeon 305-701, South Korea.
e-mail: swk@kaist.ac.kr

References

1. Coddington, I., Swann, W. C., Nenadovic, L. & Newbury, N. R. *Nature Photon.* **3**, 351–356 (2009).
2. Minoshima, K. & Matsumoto, H. *Appl. Opt.* **39,** 5512–5517 (2000).
3. Joo, K.-N., Kim, Y. & Kim, S.-W. *Opt. Express* **16,** 19799–19806 (2008).
4. Ye, J. *Opt. Lett.* **29,** 1153–1155 (2004).
5. Schuhler, N., Salvadé, Y., Lévêque, S., Dändliker, R. & Holzwarth, R. *Opt. Lett.* **31,** 3101–3103 (2006).

MATERIALS

Transparent nanofibre paper

A type of paper that has the thermal properties of glass but is flexible, foldable and optically transparent has been fabricated by scientists in Japan (*Adv. Mater.* **21,** 1595–1598; 2009). The key to the paper's enticing properties is that it is made from cellulose pulp fibres that are orders of magnitude smaller (left image) than the microscale structure found in ordinary paper (right image).

Conventional paper (centre image: the white disk) is not transparent because the size of its fibres and associated voids means that they are very efficient at scattering visible light. In contrast, the nanofibre paper (centre image: the clear disk) made by Masaya Nogi and co-workers from Kyoto University is chemically the same as conventional paper but with a miniaturized physical structure. Because the fibres are smaller than the wavelength of light and densely packed, the nanofibre paper behaves effectively as a homogeneous medium with little scatter and appears transparent.

The nanofibre paper is made from wood flour of the North American variety of the Douglas-fir. It is prepared in a water slurry and then turned into sheets, which are dried and polished with a fine sandpaper. The chemical process breaks down the wood fibres' original structure into much smaller cellulose nanofibres.

Experiments show that a 55-μm-thick sheet of nanofibre paper transmits between 60% and 80% of visible light (in the wavelength range 400 to 800 nm). As well as being transparent, the material offers some important advantages over other optically transparent materials. For example, glass has good thermal characteristics but is fragile and rigid, whereas plastics, which can be flexible, are typically not thermally stable and are prone to unwanted expansion and deformation. The nanofibre paper has the thermal characteristics of glass but is flexible and as foldable as ordinary paper.

Future research needs to explore issues such as the flammability and hydrophilic nature of nanofibre paper, but it is expected that these can be addressed by additional processing. As the nanofibre paper can be produced using existing paper-making facilities, it should be cost-effective and easy to mass-produce. Perhaps it may not be long before it finds its way into applications such as transparent electronics or flexible substrates, and as a host material for flexible displays including e-paper.

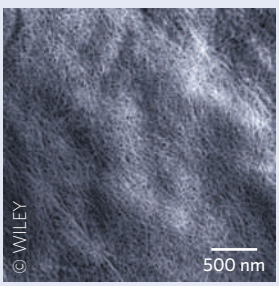

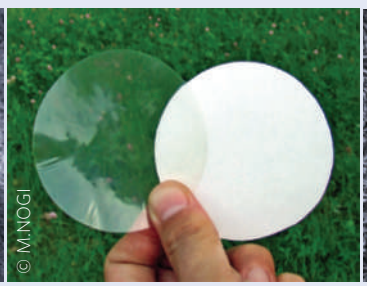

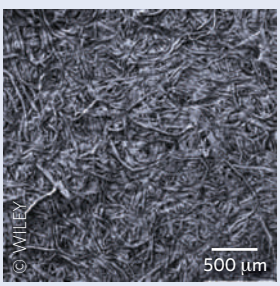

DAVID PILE

OPTOELECTRONICS

Quantum dot developments

Liquid suspensions of semiconductor nanocrystals that can be printed or coated onto a substrate promise a new era of low-cost optoelectronics. The demonstration of infrared image sensors and displays based on this approach and fully integrated with silicon electronics suggests that the technology is maturing rapidly.

Seth Coe-Sullivan

Vision is perhaps the most important way in which we interact with our environment, not only providing us with information on our surroundings, but also influencing how we live, work and feel every day. In an increasingly digital world, electronic capture, storage and presentation of images is of growing importance. As a result, the concept of high-performance image sensors and displays that can be mass-produced at very low cost is of great appeal.

A technology that is promising for meeting these needs is that of colloidal quantum dots[1] — nanoscale semiconductor crystals held in a liquid suspension. Because of the promise of improved colour quality from their light emission, combined with power-efficient operation and cost-effective solution-based processing, colloidal quantum dots are attracting intense academic study[2] and commercialization efforts[3].

Two articles in this issue show the great potential of colloidal quantum dot technology for image sensor and display applications. On page 332, Rauch *et al.*[4] demonstrate a large-area active-matrix array of near-infrared imaging photodiodes made from PbS quantum dots in an organic semiconductor matrix, and on page 341 Cho *et. al.*[5] demonstrate a large-area active-matrix array of red light-emitting devices (LEDs) based on colloidal CdSe/CdS/ZnS quantum dots combined with both organic and inorganic semiconductor layers.

Rauch and collaborators take a substantial step forward in the development of quantum dot image sensors by demonstrating high-performance (>50% external quantum efficiency) near-infrared detectors that can be directly integrated onto standard electronics. The results make use of all three of the main benefits of quantum dots: colour tunability to allow near-infrared imaging, highly efficient detection from low-voltage photodiodes, and solution-processing along with direct integration onto an amorphous-silicon (a-Si) backplane. The efficiency performance gain is achieved by the use of both hole- and electron-transporting organic materials carefully blended together with the quantum dots within the device.

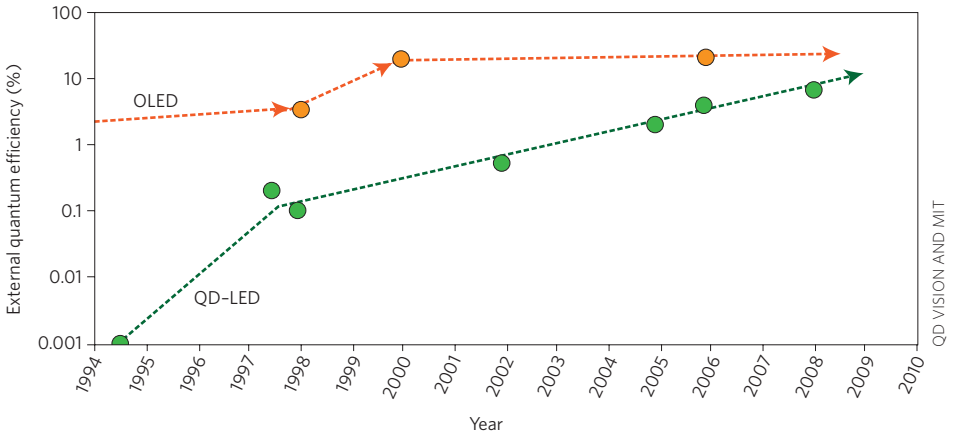

Figure 1 | Evolution of the efficiency of QD-LEDs (green circles) over their history, and comparison with OLEDs (orange circles).

Similarly, Cho *et al.* use the solution-processable nature of quantum dots to integrate an array of LEDs directly onto an a-Si backplane to produce a display image with saturated monochrome colour and respectable power efficiency. The authors take great care in tuning the energy levels of the quantum dots through choice of different ligand chemistries. In neither the Rauch nor the Cho paper is the reported performance competitive yet with other commercially available and mature technologies, but both are important steps towards achieving those performance levels, and both demonstrate that colloidal quantum dot devices can be integrated onto commercially available electronics.

Quantum dots owe their unique light emission and absorption properties to their small size and resulting quantum confinement[6]. By simply changing the particle size, it is possible to tune their bandgap, emission colour and absorption spectrum throughout the visible and infrared wavelengths. Because the absorption is broadband, quantum dots are interesting for photodetector and photovoltaic applications[7]. At the same time, the emission is narrowband or saturated, making them extremely useful in displays, optical labelling and barcoding, and lighting applications[8].

Furthermore, their tiny size enables them to be manipulated in solution, so quantum dots can be processed using a range of liquid-based methods such as inkjet printing and spin coating[9]. In general, these processing techniques are lower in cost, and amenable to large-area processing in ways that vacuum-based processes associated with normal semiconductor devices are not. Thus quantum dots are an inorganic semiconductor technology that can be extended to large-area manufacturing such as required by the display industry, and that can be directly integrated onto existing backplane technology. Conventional semiconductor devices must be grown in vacuum using expensive epitaxial growth techniques that cannot be performed over large areas; in contrast, colloidal quantum dots can simply be poured over a suitable substrate.

Quantum-dot LED (QD-LED) technology is progressing at a rapid pace, and continues to close the performance gap with organic LEDs (OLEDs) and liquid crystal displays (LCDs). Figure 1 shows the evolution of quantum dot LED peak efficiency over time, from the early demonstration[10] of 0.001% efficient electroluminescence in 1994 to

QD Vision's recent report[11] of devices with 7% external quantum efficiency (and as high as 14 lm W^{-1}). Clearly the technology is rapidly approaching the efficiency of OLEDs, and a device stability chart would show a similar trend. In this issue, Cho *et al.* from Samsung[5] report that their display has a lifetime of 50 hours at 1,000 nits brightness (that of a typical television), an achievement made possible by careful selection of inorganic charge-transport materials as well as careful control of processing conditions. The colour saturation demonstrated is already far better than can be achieved using OLEDs, or LCDs with conventional backlight units.

What truly drives intensive research is the potential of QD-LEDs to be a remarkably efficient and stable display technology. Quantum dots, like phosphorescent OLEDs, can convert 100% of the created excited states into light, can be synthesized to be extremely efficient (>90% quantum yield) and in addition, because of their narrowband saturated colour, can have best-in-class luminous efficiency. Being inorganic materials, their limits of stability are far superior to those of organic molecules and polymers. The achievable colour gamut is better than any flat-panel display technology on the market today.

Quantum-dot photodetectors have similarly impressive performance potential. Most attractive is that the absorption band edge of the detector is a tunable property of the material, and that the solution-processable layers can be integrated directly onto silicon backplanes, without the need for complicated interconnection schemes. Both of these key properties are elegantly combined in the demonstration by Tobias Rauch from Siemens and his collaborators[4]. Not only have they integrated quantum-dot photodetectors directly onto an a-Si backplane without any need for interconnects, but the array is operating at a wavelength of 1,310 nm in the near-infrared. The processing required for a conventional semiconductor photodiode array sensitive to 1,310 nm light would be completely incompatible with silicon circuitry processing, requiring expensive fabrication of separate semiconductor chips which would then need to be bonded together, pushing up the price. Thus, colloidal quantum dot photodiode arrays could prove commercially useful where cost is a more important factor than ultimate performance.

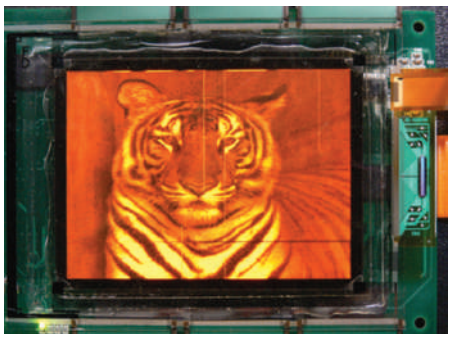

Figure 2 | Prototype colloidal quantum dot LED display built by Cho and colleagues[5].

Aside from applications in the display and detector sectors, colloidal quantum dots have already found a popular outlet in biology and medicine as fluorescent tags and markers. In biology, much R&D is now focused on ensuring that the materials are safe for use in living organisms and on opening up uses in diagnostic medicine. Human health and safety concerns are a hurdle for commercialization in this area, although continued innovations in heavy-metal-free or renal-clearable quantum dot materials are charting a possible path to large-scale applications[12].

In the optoelectronics area, small businesses such as QD Vision, Nanoco, Evident and Solexant and larger companies such as Siemens and Samsung are all racing to be the first to launch an important mainstream product, be it a display, detector or improved LED for lighting. It is likely that quantum dot technology will first go to market in applications where colour, power and design matter most.

While commercialization ramps up, the R&D community continues to focus on challenges where quantum dot technology has not yet reached its full potential. In displays, this is in improving efficiency and lifetime of the individual devices, and in developing manufacturing techniques that will scale to the large areas necessary for cost competition with LCDs. In photodetectors, maintaining efficiency of the devices while increasing their absorption is important for achieving mainstream success. For many applications, quantum dots must operate at high temperatures while maintaining performance, and so there is a need for more research to improve the state-of-the-art in temperature stability.

In the world around us, displays are becoming ever more pervasive in mobile phones, laptops and even automobiles and refrigerators. Digital detector arrays proliferate in a similar range of devices including portable still and video cameras, and laptop webcams. In all of these devices, quantum dot technology could considerably impact colour, power consumption and design. The appeal of full-colour video is unquestionable, and more efficient use of power translates to better battery life or savings in household energy bills. Some of the larger televisions on the market today will cost more to operate over the life of the product than to buy. Finally, technologies that offer lower costs of manufacture and ease of integration can drive industrial design and bring new concepts to consumer purchases. For example, webcams did not reach mainstream acceptability until they could be made small enough to be integrated directly into laptop screens. Colloidal quantum dot technology will support the continual adoption of displays, detectors and other optoelectronic devices into new products. ❐

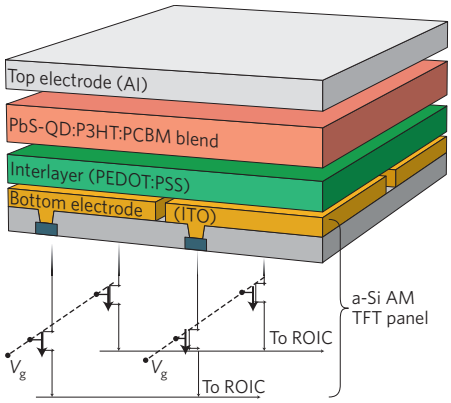

Figure 3 | Geometry of a colloidal quantum-dot photodiode array including its silicon readout backplane, as demonstrated by Rauch and colleagues[4]. AM TFT, active matrix thin-film transistor; ITO, indium tin oxide; ROIC, read-out integrated circuit; P3HT, poly(3-hexylthiophene); PCBM, [6,6]-phenyl-C61-butyric acid methyl ester; PEDOT:PSS, poly(3,4-ethylene-dioxythiophene:poly(styrene sulphonate).

Seth Coe-Sullivan is co-founder and chief technology officer at QD Vision, 313 Pleasant Street, Watertown, Massachusetts 02472, USA.
e-mail: scoe-sullivan@QDVision.com

References

1. Dabbousi, B. O. *et al. J. Phys. Chem. B* **101,** 9463 (1997).
2. Wood, V. *et al. Adv. Mater.* **21,** 1–5 (2009).
3. *Nature Photon.* **3,** 307–309 (2009).
4. Rauch, T. *et al. Nature Photon.* **3,** 332–336 (2009).
5. Cho, K. *et al. Nature Photon.* **3,** 341–345 (2009).
6. Brus, L. E. *J. Chem. Phys.* **80,** 4403–4407 (1984).
7. Huynh, W. U. *et al. Adv. Funct. Mater.* **13,** 73–79 (2003).
8. Coe, S., Woo, W.-K., Bawendi, M. & Bulovi, V. *Nature* **420,** 800 (2002).
9. Coe-Sullivan, S., Steckel, J. S., Woo, W. K., Bawendi, M. G. & Bulović, V. *Adv. Funct. Mater.* **15,** 1117–1124 (2005).
10. Colvin, V. L., Schlamp, M. C. & Alivisatos, A. P. *Nature* **370,** 354–357 (1994).
11. http://www.qdvision.com/news_090206.html
12. Choi, H. S. *et al. Nature Biotechnol.* **25,** 1165–1170 (2007).

OPTICAL TRAPPING

Microassembly

Using their expertise in optical tweezers research and two-photon polymerization (2PP), researchers from Denmark and Hungary have now demonstrated an optical assembly system that can build reconfigurable microenvironments for cells (*Opt. Express* **17,** 6578–6583; 2009).

Their system allows miniature three-dimensional polymer scaffolding of an arbitrary shape to be easily constructed. The work will help investigations into the role that the local environment plays in influencing biological behaviours, such as cell growth and function.

Jesper Glückstad and colleagues use multiple counter-propagating laser beams to trap and move microstructures made by 2PP into user-defined configurations or reconfigurable scaffolds in real time.

As their first proof of principle, the team fabricated and then manipulated microscale dumbbells (two spheres, 3.8 μm in diameter, connected by a cylindrical rod with a length and diameter of 5.4 μm and 2.2 μm, respectively) and square blocks (8 μm thick and 17.5 μm side length) featuring four circular holes with a diameter of 5 μm. The microcomponents were made from an epoxy-based resin by 2PP and then organized and connected together with the aid of multiple optical traps.

The traps were formed by passing a 1,064-nm continuous-wave fibre laser beam through a spatial light modulator to produce two matched sets of counter-propagating beam traps which were incident on the sample chamber from opposing directions. Quadruplets of counter-propagating traps were also generated to move the micro-blocks. The traps can be simultaneously configured by a computer graphical user interface, offering real-time, three-dimensional control by adjusting the power of the light beams.

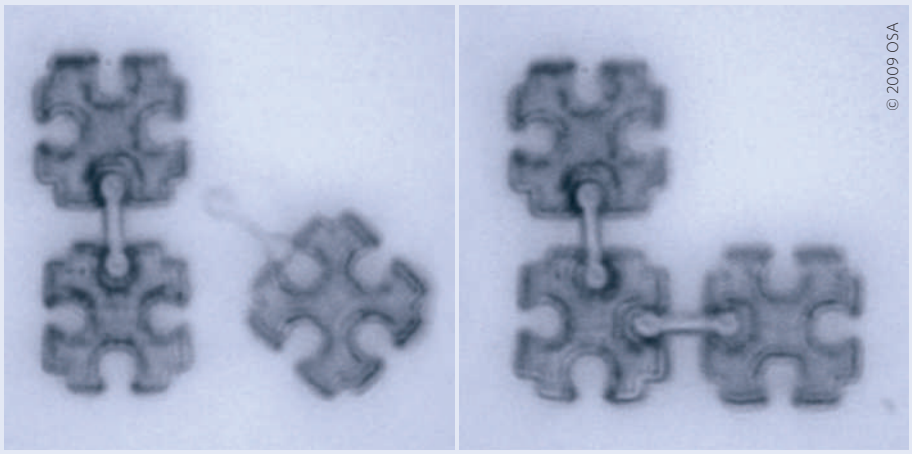

The researchers showed that the multiple-trapping scheme can be used to translate and rotate the micro-blocks and dumbbells and assemble them into composite structures. What's more, they are confident that the scheme could be applied to structures made from other materials and in other shapes.

"Building blocks made from different materials and with nanometric features can be fabricated and reconfigured to trigger cellular reactions and facilitate selective chemical functionalization," Glückstad says. He also points out that by adding in advanced spectroscopic techniques, their optical assembly platform could be used for biochemical probing. "With a generalized microassembly platform, we see no problem in assembling different microdevices and micromachines in one system," says Glückstad.

RACHEL WON

QUANTUM PHOTONICS

Quantum optics on a chip

Researchers have demonstrated a reconfigurable photonic circuit on a chip that can create a four-photon entangled state. The scalability and compactness of the device opens the door towards practical quantum computation.

Dominic W. Berry and Howard M. Wiseman

In the latest work from the quantum photonics group at the University of Bristol, described on page 346 of this issue, Jonathan Matthews and colleagues report the construction of a reconfigurable quantum optical circuit on a chip and the control of entangled states with up to four photons[1]. The heart of their device is a simple heating element that changes the phase in one arm of an interferometer. This circuit serves as a building block for potentially constructing arbitrarily large quantum optical circuits, an important step in the quest for quantum computation[2].

Quantum computation is part of the broader field of quantum information, which aims to develop a range of new technologies based on manipulating quantum systems, usually those with two levels, known as quantum bits, or qubits. Quantum key distribution, also widely known as quantum cryptography, is at present the best developed of these, and is available commercially. Its successful commercialization is partly because it requires only one qubit at a time. In contrast, quantum computation would require hundreds of qubits or more to exist simultaneously in an entangled state. Entangled states involving multiple photons,

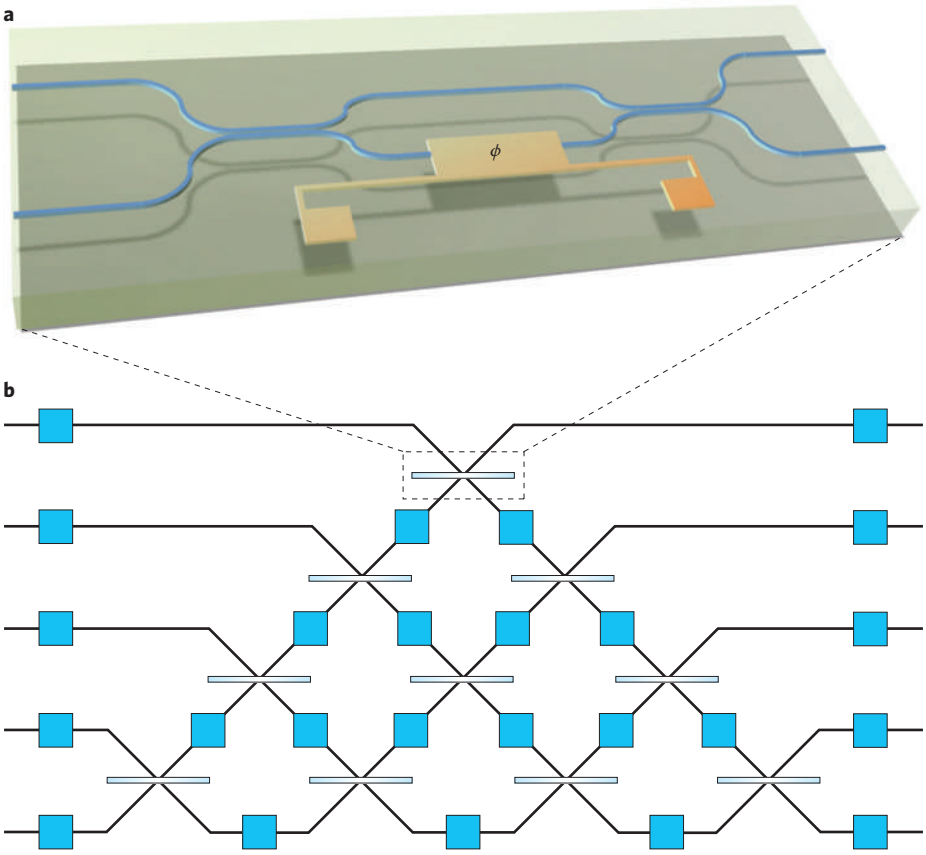

Figure 1 | The new device and its proposed use for general interferometers. **a**, The device used by Matthews *et al.*[1] is a Mach–Zehnder interferometer on a chip, with the addition of a heating element in one arm that adjusts the phase shift, ϕ. The photons pass from left to right through the waveguides, and a coupling equivalent to a 50/50 beamsplitter is achieved where the waveguides meet. **b**, A general interferometer can be achieved by a network of beamsplitters and phase shifters (blue squares). The new device is equivalent to a variable beamsplitter, so using these devices as the beamsplitters yields a general quantum optical circuit that is readily reconfigurable.

such as the 'NOON' states[3] (Schrödinger-cat-like states that are in a superposition of all the photons being in one location and all being in a second location), are of great interest for obtaining better resolution in interferometry.

Previous experiments have successfully made use of multiple qubits, creating entangled states of up to eight qubits[4] and performing simple quantum algorithms[5], but the drawback is that these experiments have typically used very bulky equipment. For example, manipulation of just a few optical qubits has required equipment that occupies an entire optical table. Manipulation of hundreds of qubits, as would be required for a quantum computer, would seem to be totally infeasible with such an approach. This is where integrated photonics comes in. Just as integrated electrical circuits greatly reduced the physical resources needed for classical computers, integrated photonic circuits, in which the optical paths are etched on a chip, have the potential to allow manipulation of large numbers of qubits.

For optical quantum information processing, the qubits are typically represented by a single photon in one of two modes. The attraction of photons is that they are good at keeping their coherence and thus preserving quantum information; for example, photons travelling from distant galaxies have maintained coherence for billions of years (which is why astronomical interferometry works). Although single-qubit operations can be achieved easily, it is far more difficult to achieve two-qubit operations because photons do not directly interact. Two-qubit operations can, however, be engineered using ingenious schemes involving measurements[6,7], and it is this principle that has been used to perform simple quantum algorithms using optics[5].

The Bristol group pioneered the miniaturization of these experiments and previously demonstrated an optical controlled-NOT gate (CNOT) on a chip[7]. That experiment was limited though, because the circuit could not be changed. It would be far more useful if a quantum information processor could be reconfigured to be able to carry out a range of tasks and switch between them. Normally, on an optical table, these different tasks would be achieved by adjusting individual components, but that is not possible when the optical circuit is permanently etched on a silicon chip.

To solve this problem, Matthews *et al.* have incorporated a thermo-optic switch into one arm of an interferometer integrated into a chip, as shown in Fig. 1a. The switch is driven by a resistive heater which causes one of the silica waveguides to change its temperature. As the refractive index of silica is temperature-dependent, an optical phase shift results. It might be thought that this is a bad thing — after all, excess heat is a well-known problem with computer chips. But it turns out that because of the small scales involved, only a small amount of heat is required to induce the phase shift, and it is possible to put considerable numbers of these devices on a chip without problems. In addition, the small scale means that the thermal switching can be done in milliseconds.

For the device that the authors have constructed, a single photon in the input encodes a qubit, and the device can be used to perform a logical NOT on this qubit, or indeed any reversible single-qubit operation of this class. On its own this device could seem to be limited. However, the authors propose using this as a building block to construct arbitrary quantum optical circuits that are easily reconfigurable. A general multimode interferometer can be realized using a triangular array of beamsplitters and phase shifters[8] as shown in Fig. 1b. To be able to reconfigure this interferometer, it would usually be necessary to vary both the phase shifts and the reflectivities of the beamsplitters, which would be a problem. Obtaining even fixed beamsplitters with the required reflectivities (such as 1/3) has been a perennial challenge in quantum information. But, as the authors point out, that is not really necessary. Instead, the device they have constructed can be used as a variable beamsplitter. Using their device in place of the beamsplitters in Fig. 1b gives a general interferometer that can be reconfigured using just thermo-optic switches.

Their device can be used for more than just processing a single qubit; they have also demonstrated two- and four-photon entangled states on the chip. These states are close to the NOON states[3],

which are popular for phase measurement because they give interference fringes like light of a higher frequency (shorter wavelength). For example, the NOON state with four infrared photons at 780 nm gives interference fringes like those of a single ultraviolet photon of wavelength 195 nm. This means that NOON states have the potential to provide far more accurate phase measurements than those possible with the unentangled states that are usually used. Indeed, the Bristol group used the increased phase resolution of their two-photon NOON state to calibrate their thermo-optic switch — probably the first practical application of such non-classical fringes. The four-photon state that the authors create is not quite a NOON state; it has an additional component. But that component does not contribute to the detections that they consider, so they obtain the same high-frequency fringes as for a NOON state. These states have been demonstrated before[9], but this is the first time they have been created on a chip, and the authors have obtained even better visibility than the experiments performed with table-top optics.

With this work it may soon be possible to place all components on a silicon chip, allowing truly compact optical quantum information processing. Essentially the only parts of this experiment that are not on the chip are the photon detectors and the photon source. Photon detectors are solid-state devices, so there is no reason why they could not be on-chip. In addition, researchers are developing solid-state single-photon sources, such as those based on quantum dots[10], that could also be placed on the chip. Normally, much of the photon loss is due to imperfect coupling between separate components (for example between free space and optical fibres), and placing the full photon path on the chip would eliminate this problem, potentially allowing far more reliable operation. Solid-state photon sources would also have the advantage of providing photons on demand — that is, when an electrical signal is sent to the source, it produces a single photon. In contrast, current experiments (including this one) use down-conversion, which produces photons at essentially random times.

The most exciting thing about this work is its potential for scalability. The small size of the interferometer means that far greater complexity is possible than with large-scale optics. The next test of this technology will be whether it can be used to perform new tasks that have not yet been achieved with table-top optics ❐

Dominic W. Berry is in the Institute for Quantum Computing at the University of Waterloo, 200 University Avenue West, Waterloo, Ontario N2L 3G1, Canada. Howard M. Wiseman is in the Centre for Quantum Dynamics at Griffith University, Nathan, Brisbane, Queensland 4111, Australia.
e-mail: h.wiseman@griffith.edu.au

References

1. Matthews, J. C. F., Politi, A., Stefanov, A. & O'Brien, J. L. *Nature Photon.* **3,** 346–350 (2009).
2. Kok, P. *et al. Rev. Mod. Phys.* **79,** 135–174 (2007).
3. Kok, P., Lee, H. & Dowling, J. P. *Phys. Rev. A* **65,** 052104 (2002).
4. Häffner, H. *et al. Nature* **438,** 643–646 (2005).
5. Lanyon, B. P. *et al. Phys. Rev. Lett.* **99,** 250505 (2007).
6. Knill, E., Laflamme, R. & Milburn, G. *Nature* **409,** 46–52 (2001).
7. Politi, A., Cryan, M. J., Rarity, J. G., Yu, S. & O'Brien, J. L. *Science* **320,** 646–649 (2008).
8. Reck, M., Zeilinger, A., Bernstein, H. J. & Bertani, P. *Phys. Rev. Lett.* **73,** 58–61 (1994).
9. Nagata, T., Okamoto, R., O'Brien, J. L., Sasaki, K. & Takeuchi, S. *Science* **316,** 726–729 (2007).
10. Strauf, S. *et al. Nature Photon.* **1,** 704–708 (2007).

FUNDAMENTAL OPTICS

Failure of plane waves

Light beams striking a flat surface are commonly considered to reflect with perfect symmetry. But highly precise experiments in the infrared region have now confirmed that this is not truly the case in practice, and the the size of the angular deviation has now been measured.

Günter Nimtz

We are often taught at school that when a ray of light is incident on a flat surface, its reflection leaves the surface at the same point as the incident ray and at a symmetrical but identical angle — the so-called Law of Reflection. This behaviour is indeed the case for the specular reflection of a perfect plane wave and is well described by plane-wave equations penned by the French scientist Augustin-Jean Fresnel (as illustrated in Fig. 1a). For many years, however, it has been known that for real beams this is not actually the case. In practice, a small deviation or 'correction' to both the position and angle of reflection is required (Fig. 1b).

On page 337 of this issue, Merano *et al.*[1] present a set of quantitative experiments in which they demonstrate the first observation of the angular deviation at near-infrared wavelengths, along with a supporting theory. The team's simple but effective recipe for the prediction of angular deviations may be important for the design of modern submicrometre photonic technology and angular metrology.

Interestingly, the first suggestion that the Law of Reflection was not strictly correct came from the English physicist Sir Isaac Newton (1643–1727), who did not accept the wave model of light and instead believed that light was composed of particles. Newton postulated that just such a lateral shift in the point of the reflection would occur in the case of total reflection[2]. His conjecture was confirmed about 250 years later by Goos and Hänchen, who measured a lateral shift between an incoming and reflected beam in an effect now commonly called the Goos–Hänchen shift.

This positional shift has to be stringently considered in the design of modern infrared glass fibre for optical communications. It can be as large as the wavelength of light, although its magnitude depends on polarization and beam diameter[3–5]. However, an exact theory is still not available. Previous expectations for maximum shift at the angle of total reflection and the dependence on the beam diameter were not confirmed experimentally[3,4,6]. Instead, a smooth and continuous transition from total reflection into the incident angle regime of non-specular reflection has recently been observed[7]. Lateral shift D and angular deviation are illustrated in Fig. 1b.

Both the positional shift and angular deviation are a result of the fact that a light beam is not a perfect plane wave but rather can be represented by a sum of plane waves propagating in different directions and hence striking the surface at different angles. Each plane wave constituting the beam therefore experiences a different coefficient of reflection, as shown in Fig. 2, which displays the variation of amplitude reflectivity with

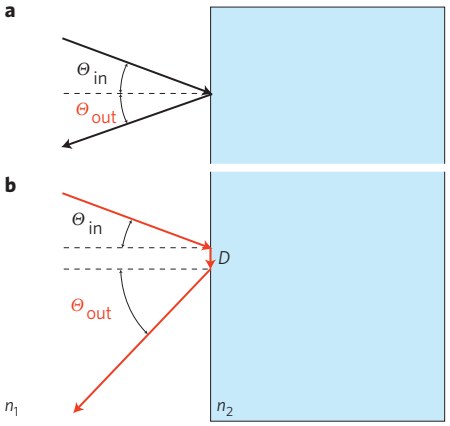

Figure 1 | Sketch of reflection without lateral and angular deviation (black arrows), and with lateral shift D and angular deviation $\Theta_{out} - \Theta_{in}$ (red arrows).

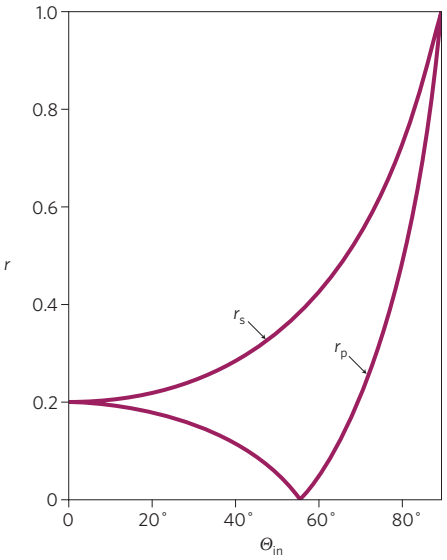

Figure 2 | Functions of amplitude reflectivity versus angle of incidence Θ_{in} of incidence for light polarized parallel, r_p, and perpendicular, r_s, to the plane of incidence. The values are for reflection at a boundary between air with refractive index $n_1 = 1$ and glass with refractive index $n_2 = 1.5$. The reflected intensity is given by $R = r_s^2 + r_p^2$.

angle of incidence for an interface between air and glass (which have refractive indices n of 1 and 1.5 respectively).

This dependence of the reflectivity can be extreme near the Brewster angle, because light polarized parallel to the plane of incidence experiences a zero in reflection (Fig. 2). For instance, varying the angle of incidence from $\Theta_{in} = 80°$ to $\Theta_{in} = 90°$ results in an increase in the reflection (intensity) of about 63%. In this example, which is in the high-reflection regime, the intensity variation gives preference to a shift of the beam direction towards 90°. It is the other regime of low reflection and high transmission, which occurs for smaller angles, that is probed by Merano *et al.* for the first time.

A previous experimental study[7] investigated the angular deviations at microwave frequencies, but in this issue the effect has been investigated with extremely high precision at near-infrared wavelength. In the experiment by Merano *et al.*, the beams were reflected by an air–glass interface and measured using a calibrated split detector at a wavelength of 820 nm and a beam width of less than 10 mm at the collimating objective in front of the light-emitting diode. Beam waists of between 34 and 95 μm were studied. To measure the effect (of the order of 10^{-2} to 10^{-5} radians) accurately, a lateral resolution of just nanometres and an angular resolution of less than a milliradian were required and achieved. Such precise quantitative results were possible only after suppressing various parasitic effects.

The experimental procedure has shown that large far-field beam displacements can occur. The experimental results are supported by a straightforward theory that considers the intensity of plane-wave components of the beam, rather than treating the beam as a single ray. By quantitatively taking the effect into account in any reflection process, it should be possible to improve the level of uncertainty in experimental measurements of angles in the future. ❐

Günter Nimtz is at the II. Physikalisches Institut, Universität zu Köln, Zülpicher Strasse 77, D-50937 Köln, Germany.
e-mail: G.Nimtz@uni-koeln.de

References

1. Merano, M. *et al. Nature Photon.* **3,** 337–340 (2009).
2. Newton, I. *Opticks* (Dover, New York, 1952).
3. Renard, R. H. *J. Opt. Soc. Am.* **54,** 1190–1196 (1964).
4. Ghatak, A., Shenoy, M. R., Goyal, I. C. & Thyagarajan, K. *Opt. Commun.* **56,** 313–317 (1986).
5. Haibel, A., Nimtz, G. & Stahlhofen, A. A. *Phys. Rev. E* **63,** 047601 (2000).
6. Artmann, K. *Ann. Phys. Leipzig* **2,** 87–102 (1948).
7. Müller, D. Tharanga, D. Stahlhofen, A. A. & Nimtz, G. *Europhys. Lett.* **73,** 526–532 (2006).

RESEARCH AND EDUCATION

Committed to optics

The creation of institutes dedicated to combining photonics research and education under one roof is helping the field to thrive. The latest country to embrace the idea is Australia, with the opening of a new institute in Sydney.

Rachel Won

Recent years have witnessed the emergence of institutes devoted entirely to pursuing photonics education and research, in clear recognition of the growing importance of the field. The latest to appear on the scene, the Institute of Photonics and Optical Science (IPOS), has just been launched at the University of Sydney and is the first and only one of its kind in Australia.

The institute was approved by the university in 2007, formally established in 2008 with Benjamin Eggleton as the Director and officially launched on 23 April 2009. It links research and postgraduate teaching programmes across the faculties of Science and Engineering at the University of Sydney to create a world-class centre with more than 30 academic and research staff and 40 postgraduate students. It consolidates a number of strong existing photonics research groups at the University of Sydney, such as the Centre for Ultrahigh-bandwidth Devices for Optical Systems (CUDOS), the former Optical Fibre Technology Centre (OFTC), the Fibre Optics Laboratory, the Astrophotonics group and other groups covering quantum photonics, biophotonics and lasers.

So what are the driving forces for creating such dedicated institutes? The rapid growth in optics research is one of the most prominent, spanning from the development of lasers and waveguiding of light through to

the manipulation of light by subwavelength structures, and the phenomena of slow and superluminal light. At a more commercial level, photonics is also the underlying technology of the Internet with applications in telecommunications, sensing, biomedical uses, astronomy and robotics. Not only that, it is also an important technology for 'green' products, such as solar cells and light-emitting diodes, that help to save or generate energy and improve our quality of life. In light of the impact of optical sciences on the way we live and communicate, many people consider it essential to draw together research and teaching in photonics and optics.

In fact, this point has already been acted on. Back in 1929, the Institute of Optics was launched at the University of Rochester, representing the very first institute to offer an education programme in optics in the United States. Thereafter, other schools, such as the College of Optical Sciences at the University of Arizona and CREOL, the College of Optics and Photonics at the University of Central Florida, were also established. Recent examples in Europe include the Karlsruhe School of Optics and Photonics at the Universität Karlsruhe, which was established in 2006, and the Abbe School of Photonics in Friedrich-Schiller-Universität Jena, established in 2008. The new addition of IPOS reflects yet again the significance of optical sciences in society.

"IPOS is to Australia what the Institute of Optics of the University of Rochester, the College of Optical Sciences of the University of Arizona, and CREOL, the College of Optics and Photonics, are to the USA, as a real point of focus for photonics," said Alan Willner from the University of Southern California, who was the keynote speaker at the launch symposium of IPOS. "Having photonics schools or institutes is imperative as they bring together focus and excellence in photonics under one roof," Willner emphasized.

RACHEL WON

IPOS is temporarily headquartered in the School of Physics, University of Sydney, while waiting for its new home.

Building on a substantial track record of research excellence at the University of Sydney, IPOS has the mission of providing Australia with the innovation, the scientists and the engineers to create and maintain a position of world leadership in the photonics community and industry. According to Eggleton, the director of IPOS as well as the research director of CUDOS, the short-term goals are to consolidate and unify the photonics and optics groups in the University of Sydney into a single organization, launch a new Masters degree in photonics in 2010, establish new photonics laboratories associated with the relocation of staff from the Optical Fibre Technology Centre on the main campus, and build a new home for IPOS (which currently has its headquarters in the School of Physics) over the next 2–3 years.

"The budget based on the research income across the different research groups is approximately four million Australian dollars per annum," revealed Eggleton. He envisages that the budget will increase as the programme grows through the Masters degree, and so will the staff numbers and funding after the opening of the new building.

"In the long run, we aim to create a visible and high-profile flagship research and education institute for Sydney, Australia and the Asia–Pacific region," said Eggleton. The combination of research and teaching of IPOS in breadth and depth of photonics is unique in the Southern Hemisphere, and the institute will be a centre of excellence in the Asia–Pacific region, he added. "Our aim is to grow IPOS into a world-leading research and education institute."

IPOS/UNIVERSITY OF SYDNEY

The official opening of IPOS.

The institute offers three types of education programme, namely a Graduate Diploma and a Masters degree in Photonics and Optical Science, and a PhD programme. The Graduate Diploma programme provides two semesters of coursework, and the Masters degree is a three-semester full-time programme. The latter combines coursework with the opportunity to conduct original research, providing students with a strong mix of high-level conceptual understanding and practical training. The PhD programme is a research-only programme. Diverse research activities can be found in the institute, in areas such as microfluidics, slow-light generation, plasmonics, supercontinuum generation, microstructured optical fibre, nonlinear optical materials, fibre lasers and astrophotonics.

When asked about the impact of IPOS on CUDOS, Eggleton explained that CUDOS is a multi-university research Centre of Excellence (COE) funded by the Australian Research Council from 2003 to 2010, whereas IPOS will be a research and education institute of the University of Sydney. Both will run in parallel and feed off each other. The COE establishes a critical research mass, a research focus and collaborations within Australia. "The Institute is a more permanent vehicle for research, teaching and infrastructure," Eggleton told *Nature Photonics*. "Many of the real challenges are ahead of us as we grow and aim to become a world-leading institute."

"What they are doing in IPOS is a model for the rest of the world, with the government and research leading individuals getting together," said Willner, adding that he hoped to see more examples following a similar path. He also pointed out that more direct involvement from the federal government in the setting up of photonics schools and institutes in the United States is appreciated.

All in all, it is encouraging to see the emergence of new schools and institutes of photonics. It signifies the importance of photonics and optics in the community. The approach should not only be a model for the photonics community, but could also be a generic model for new and emerging sciences and could be used to set 'best practice' for other disciplines. ❐

Rachel Won is an associate editor of Nature Photonics *based in Tokyo, Japan.*
e-mail: r.won@natureasia.com

nature photonics

PROGRESS ARTICLE

PUBLISHED ONLINE: 28 MAY 2009 | DOI: 10.1038/NPHOTON.2009.89

Infrared photovoltaics made by solution processing

Edward H. Sargent[1]

Solution-processed photovoltaics offer a cost-effective path to harvesting the abundant resource that is solar energy. The organic and polymer semiconductors at the heart of these devices generally absorb only visible light; however, half of the Sun's power reaching the Earth's surface lies in the infrared. Flexible solar cells that harvest wavelengths beyond 1 μm were first reported in 2005. In three years they have increased over 10,000-fold in power conversion efficiency. The latest devices achieve power conversion efficiencies in the infrared of more than 4%, values comparable to those of their organic and polymer counterparts in the visible. Here we review the progress and prospects for the field, focusing on new insights into how quantum-dot solar cells operate and how these findings give guidance on optimizing these devices to their full performance potential.

Photonic devices are most readily optimized for narrowband performance[1,2]. In solar energy conversion[3], however, the Sun's broad spectrum (Fig. 1a), spanning the visible, the near-infrared and a considerable portion of the short-wavelength infrared, means a broadband approach to photovoltaics is needed.

It is simplest to make a solar cell using a single semiconductor junction. Photons more energetic than the bandgap of the light-absorbing semiconductor are then absorbed and harvested, whereas those lying below the bandgap remain unabsorbed. Simple analysis of the Sun's power spectrum reaching the Earth implies an optimal choice of bandgap: decreasing the bandgap increases the fraction of the Sun's power absorbed, but comes at the cost of lowering the open-circuit voltage (see Table 1). For unconcentrated rays, the optimal bandgap of such a single-junction cell is 1.13 eV, corresponding to 1.1 μm in the short-wavelength infrared.

Multi-junction solar cells, wherein semiconductors with different bandgaps sequentially extract power from their respective portions of the Sun's broad spectrum, lead to higher overall solar power conversion efficiencies (Fig. 1b). A first large-bandgap cell absorbs higher-energy photons only, and provides a correspondingly large open-circuit voltage; the next cells absorb the lower-energy photons and provide additive contributions to the open-circuit voltage. The optimal bandgap choices for each member of the multi-junction stack are summarized in Fig. 1b. Both layers in the tandem (two-junction) cell are in the infrared, as are two of the three layers of the optimum three-junction photovoltaic stacked device. Use of a triple-junction architecture increases the upper bound on the power conversion efficiency for unconcentrated AM1.5 reference irradiance conditions (see Table 1) from 32% to 49%.

The benefits of matching a solar cell's response to the Sun's spectrum are widely used in commercially available photovoltaics. Silicon offers the optimal single-junction bandgap, although its low absorption from 600 nm out to its bandgap at 1,100 nm necessitates the use of thick absorbing layers and a considerable amount of crystalline silicon. Epitaxially grown triple-junction compound semiconductor devices have reached 41% AM1.5 power conversion efficiency with the aid of optical concentration[4].

The single-crystal solar cells that have led to these performance records have several practical disadvantages: high materials cost, high energy payback time and a lack of physical flexibility. As a result, large-area-compatible photovoltaics, such as those based on amorphous silicon, copper indium gallium selenide, cadmium telluride and photochemical dye-sensitized devices, have seen great advances and now offer impressive performance[5].

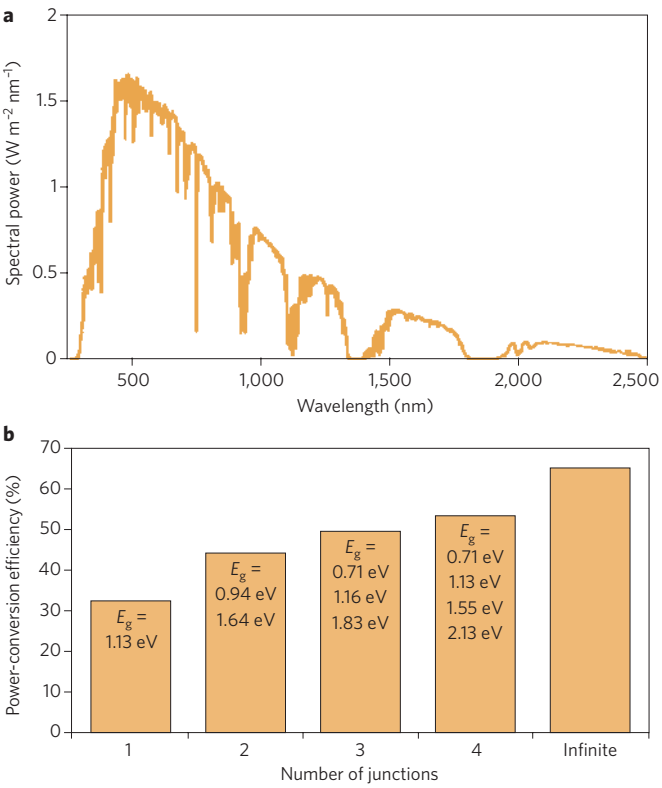

Figure 1 | The Sun's power spectrum reaching the Earth and its consequences for solar cell design. a, The unconcentrated AM1.5 solar spectrum. **b**, The maximum power conversion efficiency[54] that an *n*-junction ($n = 1, 2, 3, \infty$) solar cell can achieve for unconcentrated AM1.5 illumination. The optimal bandgap(s) for the corresponding junction(s) are indicated within the bars of the plot. For example, if only a single bandgap is used, the maximum PCE is 31.5%, and the bandgap is optimally chosen to be 1.13 eV.

Solution-processed materials, where the active light absorber is dispersed in a solvent that evaporates during the photovoltaic manufacturing process, offer particular promise with respect to cost per area. Being typically non-crystalline or polycrystalline, often with functional groups included for the passivation of surfaces, they present no issue of lattice-matching, nor the requirement for a rigid

[1]Department of Electrical and Computer Engineering, University of Toronto, 10 King's College Road, Toronto, Ontario M5S 3G4, Canada.
email: ted.sargent@utoronto.ca

Table 1 | Important terms for photovoltaic performance.

PCE	Power conversion efficiency. The ratio of electrical power provided by the cell to the optical power incident on the device.
AM1.5	Air Mass 1.5. A standard terrestrial solar spectral irradiance distribution.
Isc	Short-circuit current. The current that flows in a photovoltaic device when illuminated, and when its contacts are shorted. This value is generally greater than the actual current it can pass when a real load is powered by the cell.
EQE	External quantum efficiency. The ratio of the number of electrons flowing per second under short-circuit current conditions to the number of photons illuminating the device each second.
IQE	Internal quantum efficiency. Same as for EQE, except that it considers the number of photons absorbed by the device each second.
V_{oc}	Open-circuit voltage. The voltage provided by an illuminated photovoltaic device when no external load is connected.
FF	Fill factor. The ratio of the actual power a solar cell can supply to the maximum predicted by the product of its short-circuit current and its open-circuit voltage.

crystalline substrate. Large-area coverage can be achieved by low-temperature spray-coating or inkjet printing from the solution phase, often combined with roll-to-roll processing[6], leading to coating using continuous-flow methods instead of sequential wafer handling.

Device architecture and performance

This review focuses on recent progress in solution-processed photovoltaics that provide infrared power conversion. This focus is motivated by the urgent need for low-cost solar cells with improved power conversion efficiencies, and the need to incorporate infrared absorption into any solar cell striving to achieve high power conversion efficiencies.

Figure 2 introduces the device architecture and materials processing strategy shared by recent solution-processed infrared photovoltaics[7–11]. The most efficient devices have been made by solution-processing of semiconductor colloidal quantum dots (CQDs) (Fig. 2a, b). These nanoparticles are spectrally tunable through the quantum size effect. They are synthesized in solution with the aid of a ligand such as oleic acid that controls growth, produces a stable colloid and passivates the nanoparticles' surfaces. The long passivating ligands must be replaced by shorter molecules to increase the mobility of charge carriers in thin-film devices. Schottky-contacted solar cells (Fig. 2c) use a transparent ohmic bottom contact followed by the light-absorbing nanocrystal layer and topped with a shallow-work-function metal electrode. A 4×4 array of such devices on a glass substrate of dimensions 2.5 × 2.5 cm is depicted in Fig. 2d.

Progress in solution-processed infrared photovoltaic performance is summarized in Fig. 3 and Table 2. Performance is quantified in terms of the monochromatic power conversion efficiency at specific wavelengths. Because high-efficiency solar cells will require multiple junctions, it is necessary to examine the individual performance of each of the junctions that will become combined in future multi-junction cells. Two infrared bandgaps are of particular interest, corresponding to the two optimal infrared choices in a three-junction multi-junction photovoltaic device: ~1 μm and ~1.5 μm. (Substantial research effort in recent years has extended organic solar cell absorption towards the red within the visible spectrum. An excellent summary is available elsewhere[12]. Herein I focus instead on devices that gather a large portion of the infrared.)

Figure 3 and Table 2 show that, since the first report in 2005, solution-processed infrared solar cells have rapidly progressed to useful efficiencies (>4% monochromatic power conversion efficiency). Near 1 μm wavelength, pure-organic and pure-quantum-dot approaches vie for the performance record; whereas near 1.5 μm, pure-quantum-dot approaches alone have so far provided record efficiencies.

Device mechanisms of operation

The solar cells providing greater than 1% monochromatic power conversion efficiency near 1.5 μm have much in common[7,8,10,11]. Each used a pure quantum-dot active layer, rather than a bulk heterojunction formed by a polymer–nanocrystal mixture. Each relied on forming simple metal contacts — one deep in work function, one shallow — to this light-absorbing semiconductor quantum-dot layer. In the best-performing devices reported so far, no interlayers were required, such as those intended to block one type of carrier and extract another, as used in type-II heterojunction solar cells.

The mechanism of operation of this simple class of devices has recently been investigated in detail[10,13] and is depicted in the spatial band diagrams of Fig. 4c and d. The light-absorbing layer is a p-type semiconductor having a Fermi level that is closely aligned with the work function of the transparent contact. Little band-bending is expected at this junction, and holes can be readily extracted through the junction. In contrast, the p-type semiconductor and shallow-work-function metal contact, such as Al, Mg or Ca, differ by at least 0.6 eV in work function, producing band-bending near this interface. The resultant Schottky barrier[14] favours the extraction of electrons from the device while presenting a barrier to hole withdrawal.

From the perspective of charge-carrier transport, drift and diffusion play important roles in the operation of this device. Figure 4 depicts a drift-dominated device (a, b) and a diffusion-dominated device (e, f) to emphasize the key requirements on transport in these two cases. It also shows the spatial band diagram of a Schottky device in which drift and diffusion play quantitatively comparable roles (Fig. 4c, d). These balanced drift–diffusion devices are representative of the best infrared CQD photovoltaics.

In the light-absorbing semiconductor portion of the metal–intrinsic–metal device of Fig. 4a, the use of asymmetric contacts, one having a deep work function, the other shallow, produces a built-in field across the entirely depleted semiconductor. Under illumination,

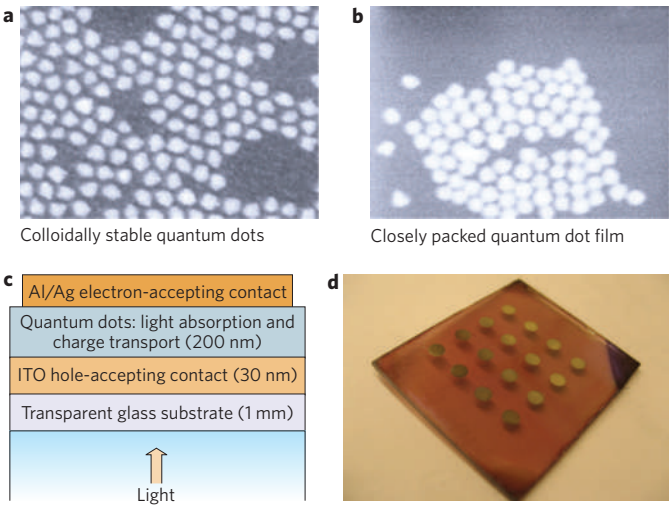

Figure 2 | Architecture of a typical solution-processed infrared photovoltaic cell. a–c Scanning electron micrographs of as-synthesized colloidal quantum dots (**a**) originally capped with long ligands that are processed in solution to provide short-ligand-capped (ligand-exchanged) nanoparticles (**b**). These are then cast to form a device. **c**, Schematic of a Schottky-barrier CQD device using a p-type semiconductor clad by an ohmic transparent bottom contact and a top contact with a shallow work function. ITO, indium tin oxide. **d**, Photograph of a 4×4 array of devices on a glass substrate, 2.5 × 2.5 cm in size.

this built-in field propels photogenerated electron–hole pairs in opposite directions.

For a device to have high internal quantum efficiency, carriers must be extracted before they recombine. This requires that the mobility μ of each carrier exceed $\tau V_{bi}/d^2$, where V_{bi} is the built-in potential, τ is the carrier lifetime, and d is the device thickness. The best recent demonstrations have shown V_{bi} between 240 mV (ref. 10) and 400 mV (ref. 7) with depletion regions ranging from 100 to 150 nm. Radiative lifetimes in Pb-chalcogenide materials have been reported to be as long as 10 μs, with 1–5 μs more typical. Together, these parameters mandate the need for mobilities exceeding 1×10^{-4} cm^2 V^{-1} s^{-1} to achieve efficient transport from the depletion region. Measurements of mobilities in films fabricated identically to those used to make CQD photovoltaic devices have so far yielded at best[9] 2×10^{-3} cm^2 V^{-1} s^{-1}, with 10^{-4} cm^2 V^{-1} s^{-1} more typical of the slower carrier, typically electrons[13]. Thus, although marginal, typical values are sufficient for efficient carrier extraction from the depletion region.

This high efficiency of electron–hole pair extraction from a 100-nm or thicker depletion zone in CQD devices contrasts with the field of polymer photovoltaics. In polymer metal–intrinsic–metal devices, external quantum efficiencies have been low, typically below 1% (ref. 15), compared with the 60% and above recently seen in CQD devices. Two factors explain this contrast. Electron–hole pairs exist as bound excitons in polymers owing to low permittivity of these materials; as a result, in the absence of very rapid charge separation, recombination occurs rapidly, typically on the nanosecond timescale. Although sufficiently high mobilities could overcome this, disordered polymer semiconductors typically show hopping with the lower mobility (electrons) at or below the 1×10^{-4} cm^2 V^{-1} s^{-1} range.

Diffusion of minority carriers also has a important quantitative role in the best CQD photovoltaics. To illustrate this process, Fig. 4e and f shows a pn-junction device in which, as a result of high doping, the depletion region is thin, and most photocarriers are generated in a quasi-neutral region. In these regions, minority carriers are required to diffuse to the junction to have the benefit of transport into their majority carrier regions by means of the built-in field. The minority-carrier diffusion length for each carrier must exceed its quasi-neutral region thickness for diffusion to be an efficient transport process contributing to high quantum efficiency. In CQD devices, estimates of minority carrier diffusion length are typically in the 100-nm range[10,16]. As this is comparable to the depletion depth near the Schottky junction, carrier diffusion contributes appreciably to the extraction of photocarriers in devices such as illustrated in Fig. 4c and d. For comparison, organic photovoltaic devices are highly reliant on diffusion, in their case the diffusion of excitons having a 5–20-nm characteristic diffusion length[17]. In organics, it is this short exciton diffusion length that necessitates the use of bulk heterojunctions[18,19] or nanoporous architectures[20] to overcome the extraction–absorption compromise. Silicon photovoltaics also rely on long-length-scale diffusion of one carrier: although silicon's length scale of hundreds of micrometres for absorption is orders of magnitude greater than that of organics and CQD films, so too is its minority carrier diffusion length, a consequence of the long lifetime of electron–hole pairs in indirect-bandgap silicon, combined with their high mobility.

Challenges and future prospects

Overcoming the absorption–extraction compromise. The best-performing solution-processed devices reported so far absorb only a fraction (10–70%, depending on wavelength) of incident photons with energies greater than the material's quantum-confined bandgap. The obvious solution is to thicken the active region; but it has been found that, although it increases absorbance, this reduces the efficiency with which charge carriers are extracted. We term this the absorption–extraction compromise.

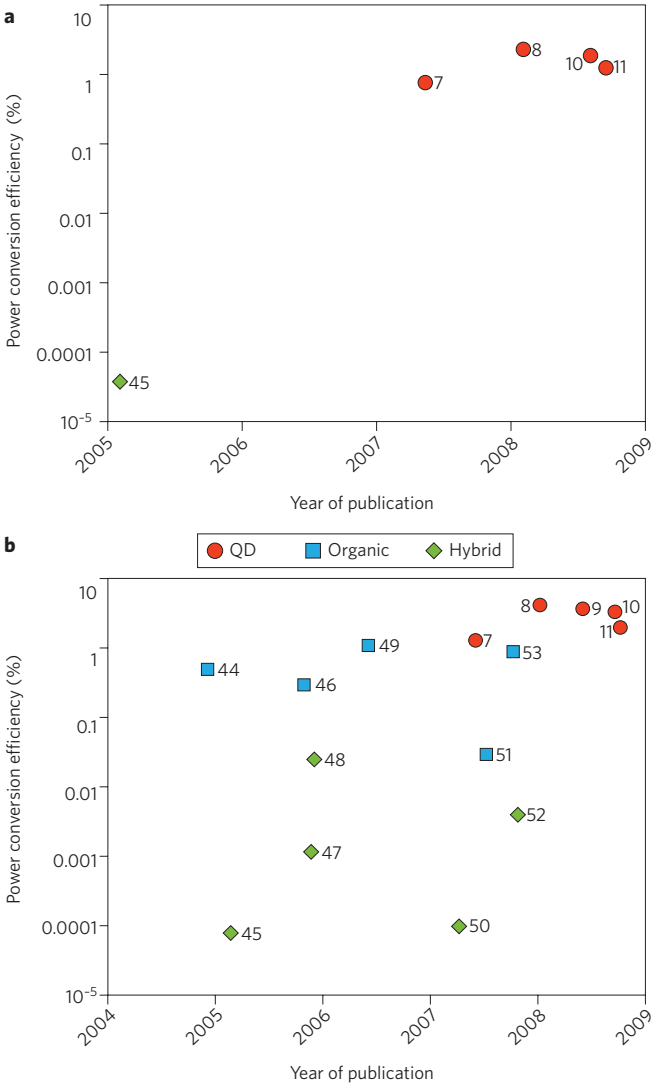

Figure 3 | Progress in infrared monochromatic power conversion efficiency of solution-processed photovoltaics. a, At 1.5 μm wavelength; **b**, at 1 μm wavelength. Organic refers to purely organic or polymer devices; QD refers to devices consisting purely of quantum dots (although they may be passivated or otherwise functionalized using short organic ligands); and hybrid refers to devices that combine an organic/polymer layer with an inorganic layer, or that use a mixture of polymer and quantum dots. Numbers are reference numbers; see also Table 2.

The depletion widths and diffusion lengths recently reported are surprisingly large, at around 100 nm, an order of magnitude greater than in organic semiconductors; and yet are still almost an order of magnitude less than the minimum absorption length for light just above the bandgap in CQD films. High external quantum efficiencies (EQEs) in the visible are therefore achieved, but high EQE is needed across the devices' entire absorbing spectrum. Near the bandgap, the absorbance α is of the order of 10^4 cm^{-1}, demanding the equivalent of ~1 μm of planar material to achieve complete absorption. In such a thickness of CQD materials today, carriers will be lost to recombination due to existing transport limitations.

Within the planar architecture, the solution is to improve mobilities. Ideally carrier mobilities need to be at least two orders of magnitude greater than the typical 1×10^{-4} cm^2 V^{-1} s^{-1} reported in CQD films. Figure 5 illustrates the degrees of freedom available to reach higher carrier mobilities.

Table 2 | Infrared photovoltaic power conversion efficiencies near two key infrared photon energies.

Date	PCE at ~1.5 μm	PCE at ~1 μm	Type	Reference
Nov 2004		0.5%	Org	44
Jan 2005	0.00004%	0.00008%	Hyb	45
Oct 2005		0.3%	Org	46
Nov 2005		0.001%	Hyb	47
Nov 2005		0.025%	Hyb	48
Apr 2006		1.1%	Org	49
Mar 2007		0.0001%	Hyb	50
Apr 2007	0.8%	1.3%	QD	7
Jul 2007		0.03%	Org	51
Sept 2007		0.004%	Hyb	52
Oct 2007		0.9%	Org	53
Jan 2008	2.4%	4.2%	QD	8
Jan 2008		3.7%	QD	9
Jul 2008	1.7%	2.3%	QD	10
Sept 2008	1.3%	2%	QD	11

QD, quantum dot; Org, organic, including small molecule, polymer and C_{60} mixtures; Hyb, a hybrid mixture of quantum dots with organic/polymer. In many cases the monochromatic power conversion efficiency at the wavelength of interest was not reported explicitly in the cited work; however, external quantum efficiency (often in the form of a spectrum), open-circuit voltage and fill factor were provided, and thus PCE was estimated as PCE = EQE × (qV_{oc}/E_{photon}) × FF (see Table 1), where q is the charge of an electron. The highest EQE in the range 950–1,000 nm was used for each reference. In general, EQE, V_{oc} and FF can vary with illumination intensity, yet the measurements in the table were not taken at a single standard illumination intensity.

The spatial separation of the quantum dots, w_b, determines the width of the energetic barrier that carriers must penetrate to reach an adjacent dot. The primary strategy to reduce this has been the replacement of long ligands, used in synthesis, with shorter ligands[21]; recent evidence shows that chemical treatments that improve inter-penetration between the ligand shells surrounding the dots offers similar transport benefits. Reducing the inter-dot barrier height, h_b, has been achieved[22] by using bidentate ligands, sometimes termed linkers, in which the bridging group, such as benzene, provides for delocalization of electrons or holes[23].

Mobilities in the range 10^{-1} to 1 $cm^2\ V^{-1}\ s^{-1}$ have been reported in CQD solids made into field-effect transistor (FET) structures[24]. Here, delocalization of charge carriers among quantum dots was achieved through the formation of an ordered lattice of nanocrystals — a superlattice. Referring to Fig. 5, w_d and w_b were made highly periodic through monodispersity and ordering, increasing the penetration of electron and hole wavefunctions into adjacent dots. Translating these high mobilities into materials that can be combined to form photovoltaic-relevant device architectures remains a challenge for CQD photovoltaics. It seems likely that there exists no fundamental incompatibility between the nanoparticle ordering and ligand chemistries that lead to high mobilities in CQD films; but these demand careful control over film morphology to avoid a low shunt impedance resulting from cracks and pinholes. The influence of mobility-enhancing surface treatments on net doping must be taken into account, and may necessitate changes in device architecture, such as a move to pn-junction devices. In materials possessing high densities of traps, the extent to which these traps are filled determines the effective mobility observed. In FET measurements, the application of a gate bias typically fills many of the deeper traps, with channel modulation revealing the mobility of the shallower traps or the subbands. In contrast, a photovoltaic device's quasi-Fermi levels are determined by the competition between optical generation on one side, and extraction and recombination on the other. This competition generally leads to carriers of at least one type having a quasi-Fermi level considerably removed from their band-edge, thus leaving traps of considerable depth exposed. Traps may in this case dominate mobility under realistic operating conditions.

A strategy complementary to transport enhancement is to break the extraction–absorption compromise. This is achieved by forming a three-dimensional structure in which photogenerated excitations are always close to a charge-separating junction. In contrast with the simple planar Schottky architecture, the active region is structured on the length scale of carrier transport, as in bulk heterojunction (Fig. 6a) and nanoporous (Fig. 6b) architectures.

In the latter case, a porous transparent electrode or electron-acceptor is infiltrated with a light-absorbing material. The device can be made thick, and prospectively fully optically absorbing, while nevertheless ensuring that electron–hole pairs lie within an extraction length (based on drift, diffusion or both) of a charge-separating junction. This approach was recently investigated and found to lead to infrared photovoltaic devices[11] having 2% monochromatic power conversion efficiency in the infrared. Thus, these first attempts have so far led to efficiencies comparable, but not yet superior, to simple planar devices. New mechanistic insights obtained in planar photovoltaic devices now indicate that an improved choice of electrode — such as TiO_2 to form a type-II heterojunction or a shallow-work-function transparent oxide such as n-ZnO to form a Schottky barrier — would offer greater advantages when working with p-type infrared-absorbing CQD semiconductors.

Engineering nanoparticle passivation. Another potential compromise looms in devices made from a collection of colloidal quantum dots. On the one hand, close spacing among nanoparticles is desired for efficient charge carrier transport through the material; on the other, nanoparticles' surfaces are generally thought to require excellent passivation to maximize charge carrier lifetimes, and the molecules used in passivation tend to be bulky and thus stand in the way of dense packing.

Recent studies have clarified the means, and the role, of passivation, and have suggested that very short (significantly less than nanometre-sized) passivating ligands can help[25]. These findings have arisen in the context of an investigation into the precise role of thiol-terminated ligands and crosslinkers in infrared CQD photovoltaic performance. Thiols have been seen to improve performance in a wide range of reports; the principal reason for this was given as improvements in mobility when short thiol-terminated ligands replaced longer original[7,10,16,26,27] ligands. It was realized that such transport enhancements could not, on their own, account for even the majority of the improvement thiols produced[25]. Further investigations showed a marked enhancement in photoluminescence quantum yield of CQD films upon thiol exposure, suggesting a role for improved passivation, especially of deep traps that serve

as recombination centres. (In the picture of Fig. 5, the passivation of deep traps implies that the distribution of trap depths h_t was clustered close to the bands, rather than near the midgap. Midgap traps capture electrons and holes with similar probability, leading to recombination instead of lifetime extension.)These observations suggested a picture of excited photocarriers familiar in organic photovoltaics[28]: excitons can either recombine or dissociate, where the latter outcome produces longer-lived states available for efficient extraction. It has been proposed that shallow traps for carriers of one type can produce such 'way stations' along the route to efficient, separate carrier extraction. These findings resonate with recent discoveries of the role of thiol treatments in photoconductive photodetectors in which thiol-treated samples retained only the short-lived traps associated with comparatively rapid temporal response[29]. Chemically, this is attributed to the reduction in thiols of species such as $PbSO_4$ associated with deep trapping.

Contacts. The metal–semiconductor junction in Schottky barrier devices has the crucial role of establishing a built-in potential, and a field to separate electron–hole pairs. In light of the sub-optimal open-circuit voltages and fill factors seen in devices so far, this junction requires, and has room to benefit from, considerable further optimization.

The first report of a Schottky junction between CQD film and a metal[14] yielded an appreciable built-in potential, but one still noticeably lower than the work function difference between the metal and the p-type semiconductor. This led to the suggestion of Fermi level pinning occurring at the semiconductor–metal interface. Such effects are important in photovoltaics as they limit the open-circuit voltage that a device can provide.

Fermi level pinning at midgap can be explained in terms of deep traps either inherent in the semiconductor or arising because of changes to the semiconductor (such as introduced by sputtering damage during metal deposition) near its surface. Further evidence of this effect was recently provided[10], in which the amplitude and polarity of the open-circuit voltage depended not only on the inherent work function difference between the two contacts, but was influenced by materials processing: the choice of which contact resided on the substrate, and which contact was sputtered atop the film at the end of film processing, influenced the polarity and amplitude of photovoltaic open-circuit voltage. Such effects were explained by invoking the effect of contact deposition technique on surface states and interface layers.

Schottky barrier photovoltaics are in general limited to providing open-circuit voltages of order half of the bandgap[3]. In smaller-bandgap (infrared) devices, this limitation may not substantially lower the open-circuit voltage compared with the idealized pn-junction. In general, however, especially for higher bandgaps, both pn-junction and heterojunction photovoltaics offer the potential of higher open-circuit voltages than in Schottky devices. Realization of a pn-junction device is thus desirable, and should be achievable in view of the ambipolar nature of PbS and PbSe (ref. 24); however, the need for highly reducing treatments, carried out in the solid state, such as those involving hydrazine, suggests that new processes must be developed that can create a controlled junction rather than converting the entire film. Heterojunction devices based on colloidal quantum dots are starting to be explored[30,31] and hold great promise.

Multi-exciton generation. Multi-exciton generation (MEG), also known as carrier multiplication, refers to the creation of two or more electron–hole pairs by a single, energetic absorbed photon[32]. Its potential advantages in solar energy conversion reside in making more efficient use of photons whose energies are well in excess of the light-absorbing semiconductor's bandgap. Initially, the absorption of such photons results in electron–hole pairs having considerably greater energy than bandgap excitons. In the absence of carrier multiplication, the electron and hole rapidly relax, through thermal intraband dissipation of energy, to the

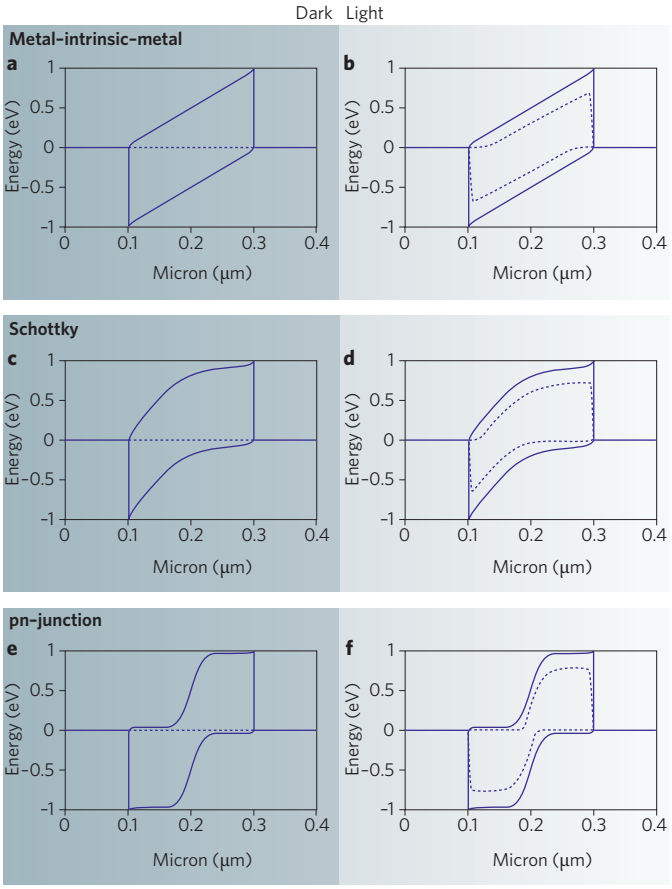

Figure 4 | Drift and diffusion of charge carriers in photovoltaics. The figure provides spatial band diagrams in the dark (left) and under solar illumination (100 mW cm^{-2}, right) for a metal–intrinsic–metal, metal–p-type–metal (Schottky), and pn-junction solar cell. The metal–intrinsic–metal device (**a**,**b**) shows uniform band-bending throughout its extent, produced by the work function difference between its electrical contacts. Electrons and holes are separated and extracted by the action of the resultant field. The Schottky device (**c**,**d**) involves one Schottky contact (produced by a large work-function difference between the shallow work-function metal on the left and the p-type semiconductor) and one substantially ohmic contact on the right. A depletion region forms, but the depletion depth is limited by the doping (in this case 1×10^{17} cm^{-3}) of the semiconductor. In the undepleted quasi-neutral region on the right half of the device, minority electrons generated by photoexcitation are required to diffuse to the edge of the depletion region, where the field sweeps them out. The pn-junction device (**e**,**f**) also forms a depletion region, narrow for the doping levels chosen herein, such that most photocarriers are required first to diffuse in order to reach the charge-separating junction.

bandgap. As a result, they lose the energy they held in excess of the bandgap. This underuse of the Sun's energetic photons accounts for the 31.5% single-junction solar energy conversion limit of Fig. 1. In contrast, in MEG an energetic electron–hole pair well above the bandgap may, for example, produce a pair of bandgap-energy excitons. Although the resultant energy of each exciton is the same as in the preceding case, the number of particles is doubled: if efficiently extracted, these excitons offer an increased short-circuit current density.

In view of the Sun's spectral distribution across the visible and infrared, if MEG is to provide enhanced solar power conversion it will require a small-bandgap light-absorber[33]. Its practical application is therefore of greatest potential interest in infrared CQD solar

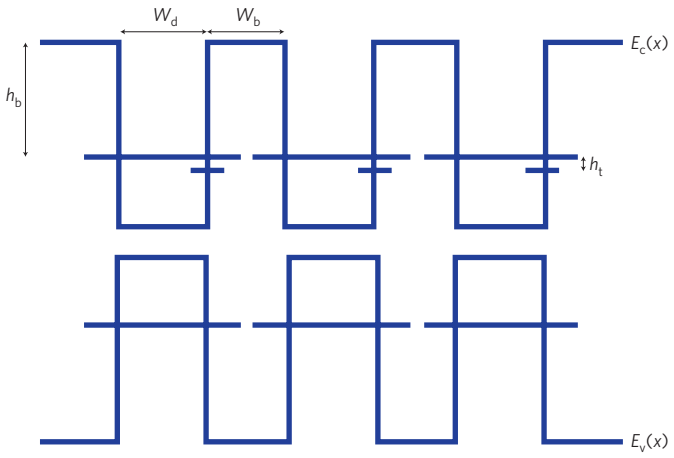

Figure 5 | Spatial band diagram of a colloidal quantum-dot solid. The diameter of the quantum dot is depicted by w_d, the spacing between dots by the barrier width w_b, the height of the barrier measured relative to the first quantum-confined state by h_b, and the energy depth of traps relative to the first quantum-confined state by h_t. E_c and E_v refer to the conduction and valence band edges, respectively, of the constituent materials. Monodispersity of quantum dots leading to a consistent w_d produces energetic alignment of confined states within the solid. A thin, consistent barrier width and height also favour carrier delocalization and transport. Passivating deep traps leaving either no traps, or only shallow traps (h_t < 0.1 eV), also favours efficient transport within a band.

cells. Colloidal quantum-dot materials in which MEG has been reported experimentally include PbS and PbSe[34], PbTe[35], CdSe[36] and Si[37]. In bulk semiconductors, carrier multiplication has been observed for over five decades, including in infrared-bandgap semiconductors such as PbS[38]. There is controversy[32] at present as to the quantitative efficiency and the photon-energy-threshold of carrier multiplication in CQDs and how these compare with bulk semiconductors; but the underlying concept is well accepted, and its prospective value in increasing photovoltaic device efficiency (in the limit, approaching multi-junction performance in a single-junction device) is understood.

An important challenge for making use of MEG is the efficient extraction of the biexcitons and triexcitons that exist within quantum dots. MEG has been reported, based on all-optical spectroscopic data, not only in solution but also in thin solid films. But in spite of numerous attempts within materials systems, and at photon energies, reported to manifest MEG, neither external nor internal quantum efficiency (Table 1) has been shown to exceed 100% (refs 8, 13, 26, 27, 39–41). In particular, one careful and systematic study[42] recently aimed to explore whether a key signature of MEG — an internal quantum efficiency of greater than unity — was observable in the optoelectronic properties of a low-bandgap PbSe CDQ photovoltaic device. Once reflection and absorption were carefully taken into account, internal quantum efficiencies approaching, but not exceeding, 100% were reported.

Two practical obstacles must be overcome to show efficient MEG harvesting in photovoltaic devices. MEG has recently been shown to be sensitive to the chemical nature of the CQD surface; and, as discussed above, so too has photovoltaic device performance. Initial studies[43] indicate that the thiol-based surface treatments, so effective in producing efficient photovoltaic devices, curtail MEG efficiency. Second, carrier extraction of multiple excitons will be considerably more challenging still than when extracting single electron–hole pairs. Whereas single excitons may survive microseconds in PbS CQDs, multiple excitons will recombine through the Auger process within less than 100 ps. In the most optimistic scenario for MEG carrier extraction, in which a significant built-in potential falls

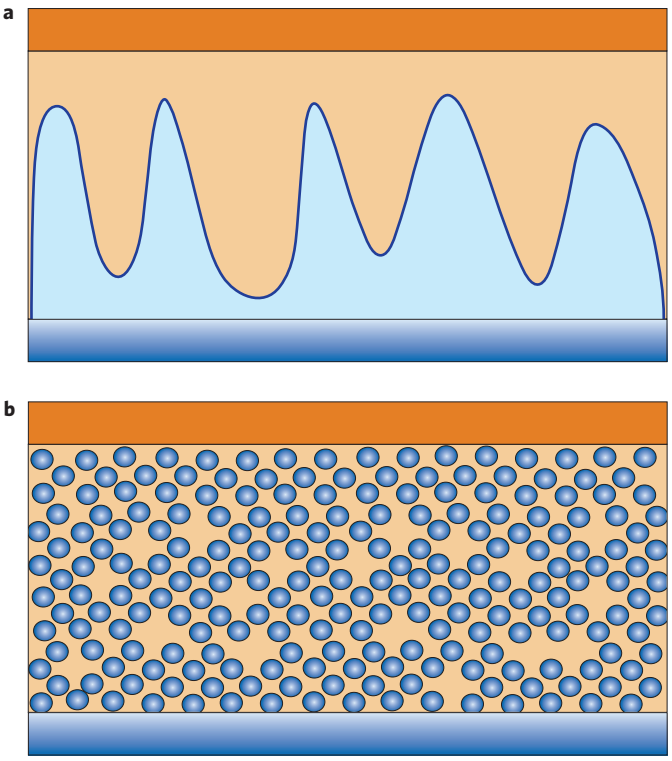

Figure 6 | Breaking the extraction–absorption compromise through nanostructuring. a, Analogue of a bulk heterojunction device, in which two phases form a high-surface-area charge-separating junction. **b**, A nanoporous architecture, in which a transparent electrode (blue) is first formed and then infiltrated with light-absorbing material (orange) such as colloidal quantum dots.

across a single layer of dots, carrier extraction within 50 ps requires an effective mobility of greater than 10^{-2} cm^2 V^{-1} s^{-1}, greater than has so far been reported in CQD photovoltaic devices. Efficient multi-exciton harvesting may, like solution-processed photovoltaic devices in general, therefore depend on further strides in improving charge carrier transport in colloidal quantum-dot solids.

Conclusion

The performance of solution-processed infrared photovoltaics is now within range of doubling the overall solar power conversion of organic photovoltaics by stacking to form a multi-junction cell. The achievement of a all-solid-state solution-processed photovoltaic device with AM1.5 power conversion efficiency of around 10% would offer a new and powerful combination of power conversion efficiency, cost and flexibility. Progress remains to be made on a number of key fronts, drawing on advances in materials chemistry, device fabrication and device modelling, for this ambitious goal to be realized. The rapid rate of progress of the field, combined with the existence of clear further avenues for device optimization, suggests that solution-processed infrared photovoltaics have a promising future.

References

1. Schurig, D. *et al.* Metamaterial electromagnetic cloak at microwave frequencies. *Science* **314,** 977–980 (2006).
2. *Min*, B. *et al.* High-Q surface-plasmon-polariton whispering-gallery microcavity. *Nature* **457,** 455–458 (2009).
3. Nelson, J. in *Physics of Solar Cells* 450 (World Scientific, 2003).
4. King, R. R. Multijunction cells: Record breakers. *Nature Photon.* **2,** 284–286 (2008).
5. Green, M. A., Emery, K., Hishikawa, Y. & Warta, W. Solar cell efficiency tables (Version 33). *Prog. Photovolt. Res. Applic.* **17,** 85–94 (2009).

6. Shah, A., Torres, P., Tscharner, R., Wyrsch, N. & Keppner, H. Photovoltaic technology: The case for thin-film solar cells. *Science* **285,** 692–698 (1999).
7. Klem, E. J. D., MacNeil, D. D., Cyr, P. W., Levina, L. & Sargent, E. H. Efficient solution-processed infrared photovoltaic cells: Planarized all-inorganic bulk heterojunction devices via inter-quantum-dot bridging during growth from solution. *Appl. Phys. Lett.* **90,** 183113 (2007).
8. Johnston, K. W. *et al.* Schottky-quantum dot photovoltaics for efficient infrared power conversion. *Appl. Phys. Lett.* **92,** 151115 (2008).
9. Koleilat, G. *et al.* Efficient, stable infrared photovoltaics based on solution-cast colloidal quantum dots. *ACS Nano* **2,** 833–840 (2008).
10. Luther, J. M. *et al.* Schottky solar cells based on colloidal nanocrystal films. *Nano Lett.* **8,** 3488 (2008).
11. Klem, E. J. D., MacNeil, D. D., Levina, L. & Sargent, E. H. Solution processed photovoltaic devices with 2% infrared monochromatic power conversion efficiency: Performance optimization and oxide formation. *Adv. Mater.* **20,** 3433–3439 (2008).
12. Winder, C. & Sariciftci, N. S. Low bandgap polymers for photon harvesting in bulk heterojunction solar cells. *J. Mater. Chem.* **14,** 1077–1086 (2004).
13. Johnston, K. W. *et al.* Efficient Schottky-quantum-dot photovoltaics: The roles of depletion, drift, and diffusion. *Appl. Phys. Lett.* **92,** 122111 (2008).
14. Clifford, J. P., Johnston, K. W., Levina, L. & Sargent, E. H. Schottky barriers to colloidal quantum dot films. *Appl. Phys. Lett.* **91,** 253117 (2007).
15. Coakley, K. M. & McGehee, M. D. Conjugated polymer photovoltaic cells. *Chem. Mater.***16,** 4533–4542 (2004).
16. Clifford, J. P. *et al.* Fast, sensitive and spectrally tuneable colloidal-quantum-dot photodetectors. *Nature Nanotech.* **4,** 40–44 (2009).
17. Blom, P. W. M., Mihailetchi, V. D., Koster, L. J. A. & Markov, D. E. Device physics of polymer: Fullerene bulk heterojunction solar cells. *Adv. Mater.* **19,** 1551–1566 (2007).
18. Halls, J. J. M. *et al.* Efficient photodiodes from interpenetrating polymer networks. *Nature* **376,** 498–500 (1995).
19. Yu, G., Gao, J., Hummelen, J. C., Wudl, F. & Heeger, A. J. Polymer photovoltaic cells: Enhanced efficiencies via a network of internal donor–acceptor heterojunctions. *Science* **270,** 1789–1791 (1995).
20. O'Regan, B. & Grätzel, M. A low-cost, high-efficiency solar cell based on dye-sensitized colloidal TiO_2 films. *Nature* **353,** 737–740 (1991).
21. Konstantatos, G. *et al.* Ultrasensitive solution-cast quantum dot photodetectors. *Nature* **442,** 180–183 (2006).
22. Hoogland, S. *et al.* Megahertz-frequency large-area optical modulators at 1.55 μm based on solution-cast colloidal quantum dots. *Opt. Express* **16,** 6683–6691 (2008).
23. Dadosh, T. *et al.* Measurement of the conductance of single conjugated molecules. *Nature* **436,** 677–680 (2005).
24. Talapin, D. V. & Murray, C. B. Applied physics: PbSe nanocrystal solids for n- and p-channel thin film field-effect transistors. *Science* **310,** 86–89 (2005).
25. Barkhouse, D. A. R., Pattantyus-Abraham, A. G., Levina, L. & Sargent, E. H. Thiols passivate recombination centers in colloidal quantum dots leading to enhanced photovoltaic device efficiency. *ACS Nano* **2,** 2356–2362 (2008).
26. Koleilat, G. I. *et al.* Efficient, stable infrared photovoltaics based on solution-cast colloidal quantum dots. *ACS Nano* **2,** 833–840 (2008).
27. Luther, J. M. *et al.* Structural, optical, and electrical properties of self-assembled films of PbSe nanocrystals treated with 1,2-ethanedithiol. *ACS Nano* **2,** 271–280 (2008).
28. Westenhoff, S. *et al.* Charge recombination in organic photovoltaic devices with high open-circuit voltages. *J. Am. Chem. Soc.* **130,** 13653–13658 (2008).
29. Konstantatos, G., Levina, L., Fischer, A. & Sargent, E. H. Engineering the temporal response of photoconductive photodetectors via selective introduction of surface trap states. *Nano Lett.* **8,** 1446–1450 (2008).
30. Lee, H. J. *et al.* CdSe quantum dot-sensitized solar cells exceeding efficiency 1% at full-Sun intensity. *J. Phys. Chem. C* **112,** 11600–11608 (2008).
31. Hyun, B. *et al.* Electron injection from colloidal PbS quantum dots into titanium dioxide nanoparticles. *ACS Nano* **2,** 2206–2212 (2008).
32. Nozik, A. J. Multiple exciton generation in semiconductor quantum dots. *Chem. Phys. Lett.* **457,** 3–11 (2008).
33. Klimov, V. I. Detailed-balance power conversion limits of nanocrystal-quantum-dot solar cells in the presence of carrier multiplication. *Appl. Phys. Lett.* **89,** 123118 (2006).
34. Ellingson, R. J. *et al.* Highly efficient multiple exciton generation in colloidal PbSe and PbS quantum dots. *Nano Lett.* **5,** 865–871 (2005).
35. Murphy, J. E. *et al.* PbTe colloidal nanocrystals: Synthesis, characterization, and multiple exciton generation. *J. Am. Chem. Soc.* **128,** 3241–3247 (2006).
36. Schaller, R. D., Sykora, M., Jeong, S. & Klimov, V. I. High-efficiency carrier multiplication and ultrafast charge separation in semiconductor nanocrystals studied via time-resolved photoluminescence. *J. Phys. Chem. B* **110,** 25332–25338 (2006).
37. Beard, M. C. *et al.* Multiple exciton generation in colloidal silicon nanocrystals. *Nano Lett.* **7,** 2506–2512 (2007).
38. Smith, A. & Dutton, D. Behavior of lead sulfide photocells in the ultraviolet. *J. Opt. Soc. Am.* **48,** 1007 (1958).
39. Law, M. *et al.* Structural, optical, and electrical properties of PbSe nanocrystal solids treated thermally or with simple amines. *J. Am. Chem. Soc.* **130,** 5974–5985 (2008).
40. Luque, A., Martí, A. & Nozik, A. J. Solar cells based on quantum dots: Multiple exciton generation and intermediate bands. *MRS Bull.* **32,** 236–241 (2007).
41. Jiang, X. *et al.* PbSe nanocrystal/conducting polymer solar cells with an infrared response to 2 micron. *J. Mater. Res.***22,** 2204–2210 (2007).
42. Law, M. *et al.* Determining the internal quantum efficiency of PbSe nanocrystal solar cells with the aid of an optical model. *Nano Lett.* **8,** 3904 (2008).
43. Beard, M. C. *et al.* Variations in the quantum efficiency of multiple exciton generation for a series of chemically treated PbSe nanocrystal films. *Nano Lett.* **9,** 836–845 (2009).
44. Wang, X. *et al.* Infrared photocurrent spectral response from plastic solar cell with low-band-gap polyfluorene and fullerene derivative. *Appl. Phys. Lett.* **85,** 5081–5083 (2004).
45. Mcdonald, S. A. *et al.* Solution-processed PbS quantum dot infrared photodetectors and photovoltaics. *Nature Mater.* **4,** 138–142 (2005).
46. Wang, X. *et al.* Enhanced photocurrent spectral response in low-bandgap polyfluorene and C_{70}-derivative-based solar cells. *Adv. Funct. Mater.* **15,** 1665–1670 (2005).
47. Zhang, S., Cyr, P. W., McDonald, S. A., Konstantatos, G. & Sargent, E. H. Enhanced infrared photovoltaic efficiency in PbS nanocrystal/semiconducting polymer composites: 600-fold increase in maximum power output via control of the ligand barrier. *Appl. Phys. Lett.* **87,** 1–3 (2005).
48. Maria, A., Cyr, P. W., Klem, E. J. D., Levina, L. & Sargent, E. H. Solution-processed infrared photovoltaic devices with >10% monochromatic internal quantum efficiency. *Appl. Phys. Lett.* **87,** 1–3 (2005).
49. Wienk, M. M., Turbiez, M. G. R., Struijk, M. P., Fonrodona, M. & Janssen, R. A. J. Low-band gap poly(di-2-thienylthienopyrazine):fullerene solar cells. *Appl. Phys. Lett.* **88,** 153511 (2006).
50. Gunes, S. *et al.* Hybrid solar cells using PbS nanoparticles. *Solar Energy Mater. Solar Cells* **91,** 420–423 (2007).
51. Sun, M. *et al.* Near-infrared response photovoltaic device based on novel narrow band gap small molecule and PCBM fabricated by solution processing. *Solar Energy Mater. Solar Cells* **91,** 1681–1687 (2007).
52. Dissanayake, D. M. N. M. *et al.* A PbS nanocrystal–C_{60} photovoltaic device for infrared light harvesting. *Appl. Phys. Lett.* **91,** 133506 (2007).
53. Perzon, E. *et al.* A conjugated polymer for near infrared optoelectronic applications. *Adv. Mater.* **19,** 3308–3311 (2007).
54. Henry, C. H. Limiting efficiencies of ideal single and multiple energy gap terrestrial solar cells. *J. Appl. Phys.* **51,** 4494–4500 (1980).

Acknowledgements

I thank S. Hinds for producing the spatial band diagrams of Fig. 4.

nature photonics

LETTERS

PUBLISHED ONLINE: 17 MAY 2009 | DOI: 10.1038/NPHOTON.2009.72

Near-infrared imaging with quantum-dot-sensitized organic photodiodes

Tobias Rauch[1‡*], Michaela Böberl[2†‡], Sandro F. Tedde[1], Jens Fürst[1†], Maksym V. Kovalenko[3], Günter Hesser[2], Uli Lemmer[4], Wolfgang Heiss[3] and Oliver Hayden[1*]

Solution-processed photodiodes with infrared sensitivities at wavelengths beyond the bandgap of silicon (corresponding to a wavelength of ~1,100 nm) would be a significant advance towards cost-effective imaging. Colloidal quantum dots are highly suitable as infrared absorbers for photodetection, but high quantum yields have only been reported with photoconductors[1–3]. For imaging, photodiodes are required to ensure low-power operation and compatibility to active matrix backplanes[4]. Organic bulk heterojunctions[5] are attractive as solution-processable diodes, but are limited to use in the visible spectrum. Here, we report the fabrication and application of hybrid bulk heterojunction photodiodes containing PbS nanocrystalline quantum dots as sensitizers for near-infrared detection up to 1.8 μm, with rectification ratios of ~6,000, minimum lifetimes of one year and external quantum efficiencies of up to 51%. By integration of the solution-processed devices on amorphous silicon active matrix backplanes, we demonstrate for the first time near-infrared imaging with organic/inorganic hybrid photodiodes.

The growing interest in imaging in the near-infrared (NIR) is related to the increasing number of applications in this spectral region, including optical tomography[6] process monitoring[7] and night vision[8]. The spectral region between 1 and 1.8 μm is of particular commercial interest due to the low water absorption in this range. InGaAs photodiodes are the current choice for NIR imaging applications, and are usually integrated on CMOS-based readout integrated circuits (ROIC)[7]. Alternative approaches to NIR detection include epitaxially grown quantum dots (QDs) and quantum well infrared photodetectors[9,10]. For the fabrication of large-area devices, organic semiconductors have advantages over epitaxial structures because of their simplified process handling. However, neither small molecules nor polymers with low bandgaps are currently available for the manufacture of efficient photodiodes in the spectral region above 1 μm (refs 11–13). In contrast, the sensitivity of devices based on colloidal QDs can be easily tuned into the NIR, as has been repeatedly demonstrated with photoconductors[2,3,14,15]. Inorganic/organic hybrid photodiodes (IO-HPDs) are based on a ternary blend containing PbS–QDs and two organic materials forming a bulk heterojunction. Flat-panel imagers are fabricated by integrating the solution-processed infrared photodiodes on top of amorphous silicon active matrix (a-Si AM) backplanes. Figure 1a presents an exemplary reconstructed image comprising a shadow cast of a slide of a monarch butterfly, obtained under infrared illumination at a wavelength of 1,310 nm. For comparison, the original slide is presented as an inset. Experimental results show that the infrared sensitivity of the imager results from the QDs embedded in the organic photodiode and not from the silicon transistors of the AM backplane (see Supplementary Information).

The NIR photosensitivity of the imagers was provided by a non-structured IO-HPD operating, in contrast to organic visible imagers[16–18], on the concept of charge separation between an infrared sensitizer, the PbS–QDs, and separate electron- or hole-accepting and transporting materials—[6,6]-phenyl-C61-butyric acid methyl ester (PCBM) and poly(3-hexylthiophene) (P3HT) in particular. Poly(3,4-ethylenedioxythiophene):poly(styrenesulphonate) (PEDOT:PSS) interlayers were used to improve the electrical contact to the structured indium tin oxide (ITO) bottom contact. Low-workfunction metals were evaporated to form the top contact (see Fig. 1b for a schematic of the layer sequence and the Methods for details). The low- and high-resolution transmission electron microscope (TEM) images in Fig. 1c show cross-sections of a photodiode and the photoactive layer, respectively. The dispersed colloidal PbS in the IO-HPD corresponds to a QD volume fraction of ~50% (67 wt%). In contrast to reported QD solar cells[1,15,19] and photoconductors[2,20], we have made use of PbS–QDs, as-synthesized with an oleic acid capping (see Methods). Solution-processed diodes were integrated on top of commercially available a-Si AM thin-film transistor (TFT) panels with 256 × 256 pixels, a pixel pitch of 154 μm, and a geometrical fill factor of 83.3%. Pixel pitches were defined by the ITO bottom contact pad and the distance to the neighbouring pixel, as shown in the optical micrograph in the inset of Fig. 1b. Equivalent to a flat-panel detector, the pixel readout scheme transfers the signal to the ROIC using a TFT switch at an applied voltage (V_g) to the gate.

The infrared image quality crucially depends on the characteristics of the hybrid photodiodes. Dark currents and photocurrents of IO-HPDs measuring 4 mm^2 with a 200-nm-thick absorber layer and an aluminium top contact are shown in Fig. 2a on a semi-logarithmic scale. Rectification ratios of ~6,000 at bias voltages of ±2 V are observed. Illumination of the photodiode with monochromatic green light at 532 nm and a power density of 780 μW cm^{-2} increases the current density by three orders of magnitudes at −2 V reverse bias. This sensitivity for green light is related to its absorption by both P3HT and PbS–QDs. To obtain the photocurrent due to QD absorption only, the device was illuminated with polychromatic light of wavelengths greater than 870 nm (see Methods). Polychromatic infrared illumination increases the photocurrent density by a factor of almost 400 from 8.8×10^{-5} mA cm^{-2} to 3.4×10^{-2} mA cm^{-2} at −2 V. The schematic energy band

[1]Siemens AG, Corporate Technology, CT MM1, 91058 Erlangen, Germany, [2]Christian Doppler Laboratory for Surface Optics, Institute of Semiconductor and Solid State Physics, University of Linz, 4040 Linz, Austria, [3]Institute of Semiconductor and Solid State Physics, University of Linz, 4040 Linz, Austria, [4]Light Technology Institute, Universität Karlsruhe (TH), 76128 Karlsruhe, Germany; †Present address: Siemens VAI MT GmbH & Co, I IS MT IR AG T, 4031 Linz, Austria (M.B.); Siemens AG, H IM CVV, 91058 Erlangen, Germany (J.F.); ‡These authors contributed equally to this work.
*e-mail: tobias.rauch.ext@siemens.com; oliver.hayden@siemens.com

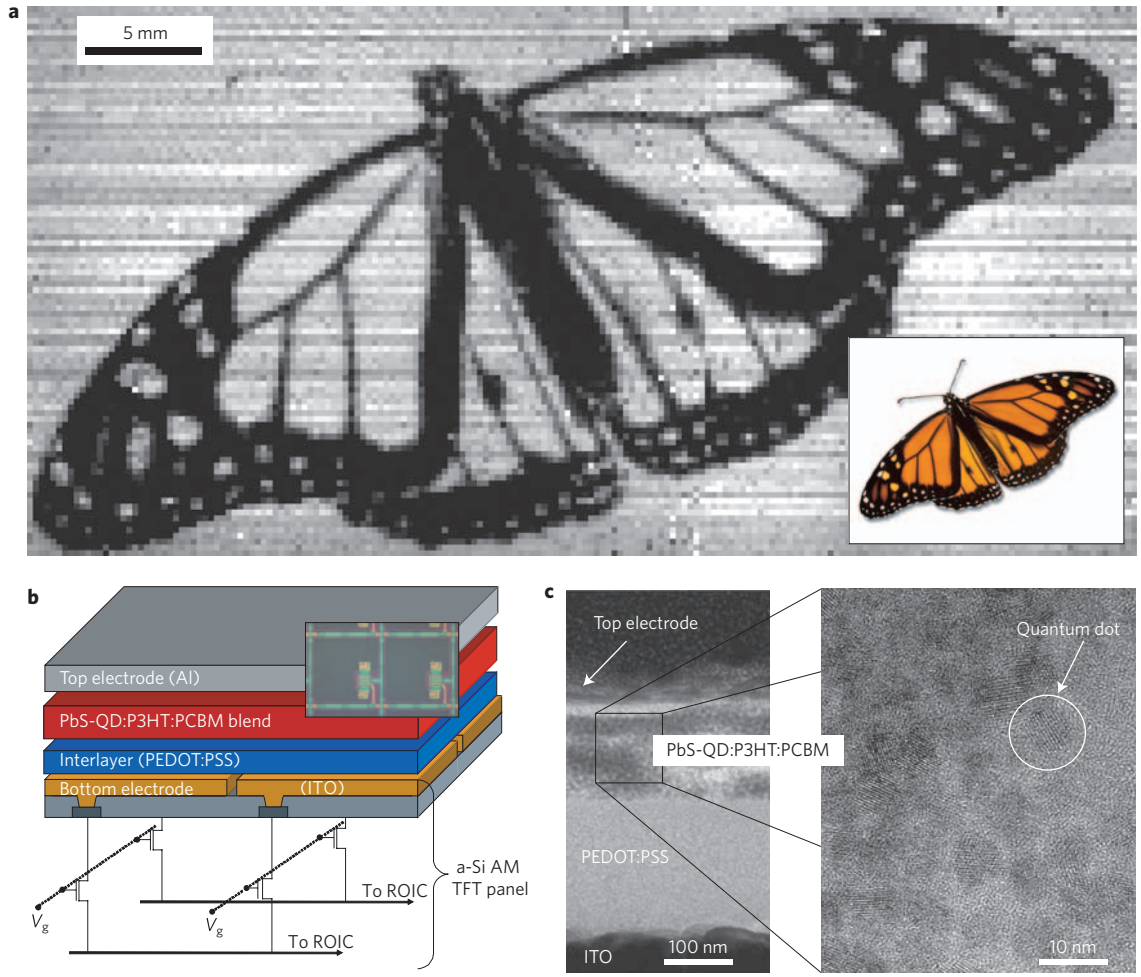

Figure 1 | PbS-QD-sensitized organic NIR imager. a, Infrared shadow cast at 1,310 nm of a slide showing a monarch butterfly (the original slide is shown in the inset for comparison). **b**, Schematic of the imager with an a-Si AM backplane and an unstructured inorganic/organic hybrid frontplane. The inset shows an optical micrograph of two active matrix pixels with a pixel pitch of 154 μm. **c**, TEM cross-section of the hybrid diode layer stack. The high-resolution TEM image shows colloidal QDs distributed in the P3HT:PCBM matrix. a-Si AM, amorphous silicon active matrix; ROIC, readout integrated circuits; TFT, thin-film transistor; P3HT, poly(3-hexylthiophene); PCBM, [6,6]-phenyl-C61-butyric acid methyl ester; PEDOT:PSS, poly(3,4-ethylenedioxythiophene):poly(styrenesulphonate).

diagram of the ternary blend illustrated in the inset of Fig. 2a suggests an almost flat band condition between the lowest unoccupied molecular orbit (LUMO) of the PCBM and the lowest unoccupied quantum dot state of the PbS. Furthermore, the staggered band alignment between P3HT and the QDs allows both electron and hole transfer from the QDs to the PCBM and the P3HT, respectively.

For imaging applications an effective conversion of photons to electrons is crucial; this is characterized by the external quantum efficiency $\mathrm{EQE} = hcI_{\mathrm{ph}}(e\lambda P)^{-1}$, where h is Planck's constant, c the velocity of light, I_{ph} the photocurrent, e the elementary charge, λ the wavelength of the incident light and P the power of the light falling onto the photodetector. Figure 2b shows the EQE of an IO-HPD with an aluminium top electrode and a reverse bias of −5 V. In contrast to organic P3HT/PCBM photodiodes with a cutoff wavelength of 650 nm (ref. 21), the IO-HPD with 4.5-nm diameter PbS–QDs shows infrared sensitivity of up to 1,450 nm. The peak in the sensitivity spectrum at 1,220 nm is attributed to the first excitonic transition in the PbS–QDs and corresponds to an EQE of 16.5% and a responsivity of 0.16 A W^{-1}. Increasing the content of QDs in the IO-HPDs from 50 to 80 wt% results in a gradual increase of both the photoresponse and the dark current by a factor of up to 40 (Fig. 2b, inset). Beyond a QD content of 75 wt% in the IO-HPD, the dark current becomes strongly voltage dependent and increases from 4.6×10^{-3} mA cm^{-2} to 2.5×10^{-2} mA cm^{-2} at −5 V. Thus, a QD content of 67 wt% is the optimum concentration in IO-HPDs, this being a tradeoff between responsivity and dark current (a discussion of performance limitations due to dark currents is given in the Supplementary Information). For the EQE a linear regime from −5 to −8 V can be observed that is related to a photoconductive gain enhancing the EQE up to 51% (Fig. 2c), corresponding to a responsivity of 0.5 A W^{-1}. Noise analysis indicates that this 4-mm^2 diode is shot-noise limited, with a noise equivalent power of 8.7×10^{-11} W and a normalized detectivity of 2.3×10^9 Jones at a modulation frequency of 170 Hz. From experiments with blends of PbS–QDs:PCBM and PbS–QDs:P3HT we observe diode rectification but poor infrared sensitivity, with EQE values of 2.3 and 0.2%, respectively. Thus, the presence of both P3HT and PCBM is necessary for efficient charge carrier separation of the QD excitons and charge transport from the PbS–QD to the top and bottom electrodes. The electron transfer[22] is possible due to the matching LUMO levels (∼−4.3 eV) of PCBM (ref. 23) and PbS–QDs (cf. Fig. 2a, inset), which takes place on a timescale of a few 100 ps (ref. 24). In addition, the major difference in EQE values between the PbS–QDs:PCBM (ref. 25) blend and the IO-HPDs indicates that the presence of P3HT in the blend is critical to facilitate hole transport. This interpretation is confirmed by transport measurements performed with a field-effect transistor geometry, exhibiting

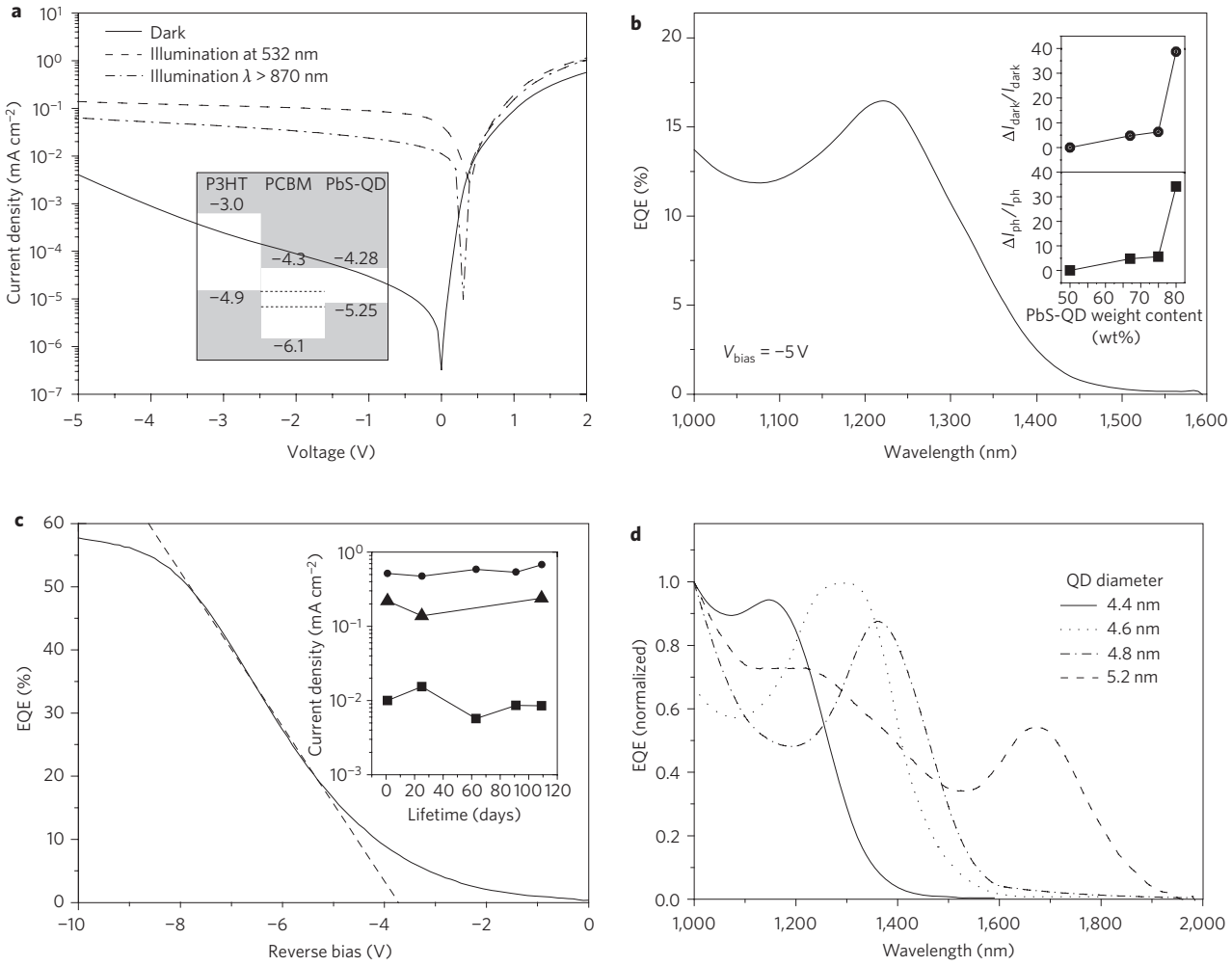

Figure 2 | Current–voltage and spectral properties of IO-HPDs. a, *I–V* characteristics of the device with an active area of 4 mm^2 in the dark (solid), with monochromatic illumination at 532 nm (780 μW cm^{-2}; dashed line) and with polychromatic light ($\lambda > 870$ nm; dash-dotted line). Inset: HOMO/LUMO levels of the organic bulk heterojunction and the approximate bandgap of PbS-QDs. Bulk bandgap of PbS (dotted line). **b**, Spectral sensitivity of a photodiode with ~4.5 nm PbS-QDs with a peak EQE of 16.5% at 1,220 nm, biased at −5 V. Inset: Relative variation of photoresponse at 1,350 nm (squares) and dark current at −5 V (circles) with increasing weight content of PbS-QDs in the P3HT/PCBM matrix. **c**, Voltage dependence of EQE with a linear regime from −5 to −8 V with an EQE of 51%. Inset: lifetime measurements of an IO-HPD (63 days accelerated: 38 °C, 90% RH; 45 days: ambient conditions) showing the fluctuation of photoresponse to illumination at 532 nm (circles), with polychromatic light >870 nm (triangles) and in the dark (squares) at −4 V. **d**, Normalized EQE spectra of hybrid photodiodes sensitized with PbS-QDs of different diameters.

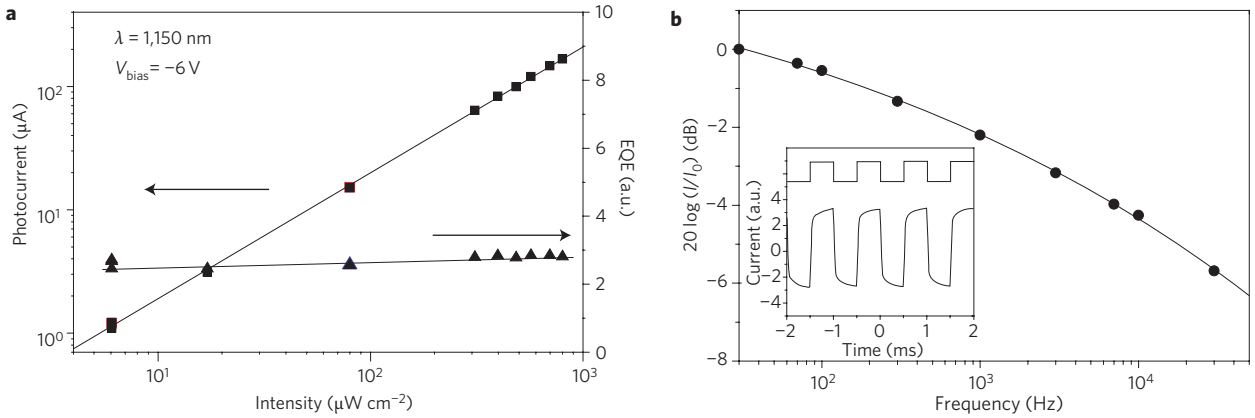

Figure 3 | Photoresponse and dynamic properties of hybrid photodiodes. a, Photocurrent (squares) and EQE (triangles) of a diode biased at −6 V as a function of the light intensity at a wavelength of 1,150 nm. **b**, Frequency response characteristic of a 0.8-mm^2 photodiode. The inset shows a train of photocurrent peaks (1 kHz) concurrent with modulated light at a wavelength of 1,310 nm.

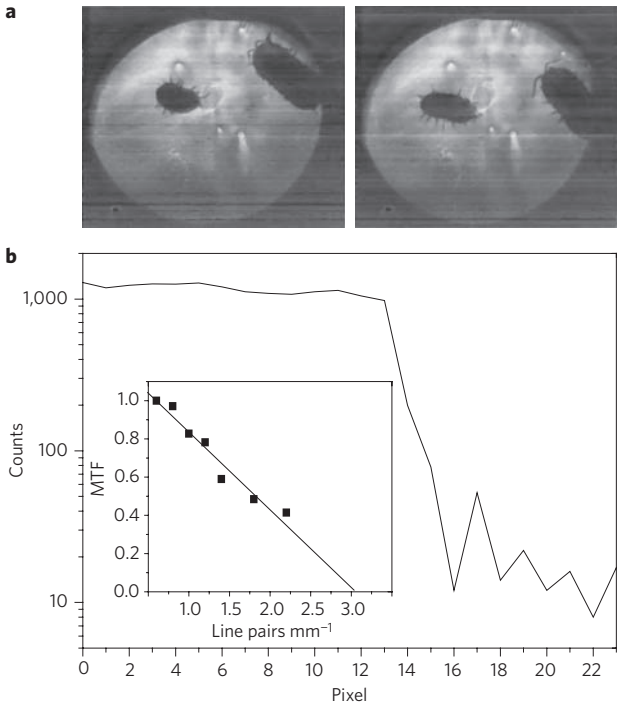

Figure 4 | Characterization of the imager illuminated at 1,310 nm (1.6 mW cm^{-2}). a, Snapshots from a movie with five frames per second showing the shadow cast of two woodlice. **b**, Image crosstalk shown as the response of a pixel row at a sharp metallic edge. Inset: spatial frequency response of the infrared imager.

ambipolar transport for the ternary blend containing oleic-acid capped PbS–QDs, PCBM and P3HT. Hole and electron mobilities in the IO-HPD of up to 4.3×10^{-4} cm^2 V^{-1} s^{-1} and 4.6×10^{-5} cm^2 V^{-1}s^{-1}, respectively, are observed. However, neither pure PbS–QDs (no measureable transport at all) nor composites of PCBM:PbS–QDs (electron transport only) and P3HT:PbS–QDs (hole transport only) demonstrated any ambipolar mobilities (see Supplementary Information for details). Note that the efficient and separate charge carrier transport of electrons and holes is key to the high infrared sensitivity of IO-HPDs, even though long oleic acid ligands are still attached to the QD surfaces. In pure QD photoconductors the replacement of oleic acid ligands from colloidal PbS–QDs with shorter ligands such as butylamine is crucial to achieve photoconductivity and thereby photosensitivity[2]. In strong contrast to QD photoconductors, we observe that oleic acid capped QDs in IO-HPDs show higher EQE values. Because it is not necessary to exchange the oleic acid ligands, the composite has the benefits of superior stability and lifetime compared to other ligands[1]. For a 4-mm^2 diode, accelerated aging test results show minimum lifetimes of one year, as illustrated in the inset of Fig. 2c as current densities of the photoresponse to illumination at 532 nm, to polychromatic light >870 nm and in the dark, over 100 days, under partially accelerated aging conditions (see Methods). Only moderate fluctuations of the photoresponse to illumination at 532 nm and >870 nm around 5×10^{-1} mA cm^{-2} and 2×10^{-1} mA cm^{-2} are observed, respectively. The dark current remains stable at values around 1×10^{-2} mA cm^{-2}. Owing to the quantum size effect in nanocrystals, even the absorption edge and thus the cutoff wavelengths of the IO-HPDs can be tuned by the QD diameter in the ternary blend[26]. Figure 2d shows a summary of EQE spectra for several QD-sensitized diodes with PbS–QD diameters ranging from 4.4 to 5.2 nm (ref. 27), extending the cutoff wavelength of the IO-HPD from 1,350 to 1,850 nm.

Equally important to spectral sensitivity is the linear device response on the incident light intensity for imaging. The dependence of the photocurrent on illumination intensity at 1,150 nm is shown in Fig. 3a. The photocurrent of the hybrid diodes biased at −6 V increases linearly with increasing light intensity from 4 μW cm^{-2} to 0.8 mW cm^{-2}, resulting in a constant EQE over more than two decades. For imaging purposes the frequency response is also important; this was studied in photodiodes with an active area of 0.8 mm^2 under an illumination at 1,310 nm (Fig. 3b). Figures of merit include the frequency at which the amplitude of the photocurrent is decreased to $1/\sqrt{2}$ of the d.c. value (−3 dB frequency) and the frequency at which the amplitude is half of the d.c. amplitude (−6 dB value). Limited by the parasitic capacitances of the thin-film device, the −3 dB frequency of the PbS–QD sensitized photodiode is as high as 2.5 kHz and the −6 dB frequency is 39.5 kHz. The inset of Fig. 3b shows rise and fall times at 1 kHz of 69 and 91 μs, respectively. These temporal responses are suitable for conventional imaging applications such as cell phone imagers with frame rates of 30 Hz.

With the EQE values and temporal responses achieved, the PbS–QD sensitized photodiodes are highly suitable for NIR imaging and video applications. Snapshots of a movie recorded at a frame rate of 5 Hz are shown in Fig. 4a. Two woodlice (*Armadillidium vulgare*) illuminated at 1,310 nm are displayed, even fine features such as limbs and antennae being discernible. The movements of these animals can be captured easily (see Supplementary Information for the whole movie). In Fig. 4b the crosstalk between the pixels of the imager is characterized by illumination over a sharp metal edge covering a region of interest. A 20–80% signal rise of more than 1,200 counts is observed within one pixel pitch of 154 μm. To quantify the resolution, we calculated the contrast at a given spatial frequency by means of the modulation transfer function (MTF) as line pairs per millimetre (lp mm^{-1}). The inset of Fig. 4b shows the MTF of the QD-sensitized organic imager. The measured points are fitted linearly and extrapolated to a maximum resolution of ~3 lp mm^{-1}, which is consistent with pixel pitch.

Methods

Device fabrication. Hybrid photodiodes were fabricated on ITO-coated glass substrates (Merck) or on a-Si AM TFT backplanes with ITO bottom contacts. After cleaning and an oxygen plasma treatment of the substrates, PEDOT:PSS interlayers were spin-coated and baked at 200 °C for 20 min, resulting in a film thickness of 100 nm. If not specified otherwise in the text, the photosensitive layers comprise organic/inorganic blends with a weight ratio of 1:1:4 = P3HT:PCBM:PbS–QDs. The blend was dissolved in chlorobenzene and deposited on the substrate by means of Doctor blading, resulting in film thicknesses of 100–250 nm. Aluminium top contacts were thermally evaporated through a shadow mask. Solvent-free epoxy resin and glass coverslips were used to encapsulate the IO-HPDs. The PbS–QDs capped with oleic acid were synthesized as described by Hines and colleagues[28]. Size dispersions of the QDs had a variation within 10–15%. Photoluminescence and TEM measurements were performed to control QD diameter.

Characterization. Cross-sectioning of the hybrid photodiodes was performed with focused ion beam milling (ZEISS 1540 XB) with 20 keV gallium ions. Electron micrographs of the device cross-section were obtained using a JEOL 2011 FasTEM. The *I*–*V* characteristics of 4-mm^2 diodes were recorded using a Keithley 6487 picoammeter in an electrically and optically shielded box. For illumination of the photodiodes in the visible, a green light-emitting diode with a wavelength of 532 nm and a power density of 780 μW cm^{-2} was used. Infrared illumination was performed with a white light beam of an AM 1.5 Oriel solar simulator with a power density of 100 mW cm^{-2} and a GaAs filter with a cut-on wavelength of 870 nm. EQE spectra were recorded using a lock-in technique using a chopping frequency of 170 Hz and an Oriel Cornerstone 130 1/8 m monochromator. An InGaAs photodiode was used as a reference diode for calibration.

Accelerated lifetime tests were performed within an ESPEC SH-221 climatic chamber for 63 days at 38 °C and 90% relative humidity (acceleration factor 6) and for 45 days under ambient conditions. The aging factor was calculated based on permeation rate determination of sealed substrates by measuring the temporal change of the ohmic behaviour of the calcium contacts[29].

Imaging. For the infrared images the panels were illuminated with a InGaAsP laser diode (ML725B8F) operating at a wavelength of 1,310 nm with a peak intensity

of ~1.6 mW cm^{-2}. The integration/readout time per pixel row was fixed to 20 μs, ending with a 3-ms reset pulse. To exclude undesired response from the a-Si AM TFT panel, reference measurements were performed with identical illumination conditions on an imager with a P3HT:PCBM layer. This device exhibited a signal increase of only eight counts in a defined region of interest of 27 × 48 pixels. The final images were reconstructed by subtracting the dark level from the image. Furthermore, each pixel was flat fielded, meaning that each pixel was divided by the corresponding intensity value (light level–dark level). Counts were the equivalent value of the output bits of the ROIC (14 bits = 16,383 counts, 1 count corresponding to 4,084 electrons). The MTF was determined by the following equation: (maximum signal–minimum signal)/(maximum signal + minimum signal) (ref. 30).

Received 9 December 2008; accepted 7 April 2009; published online 17 May 2009

References

1. Koleilat, G. *et al.* Efficient, stable infrared photovoltaics based on solution-cast colloidal quantum dots. *ACS Nano* **2,** 833–840 (2008).
2. Konstantatos, G. *et al.* Ultrasensitive solution-cast quantum dot photodetectors. *Nature* **442,** 180–183 (2006).
3. McDonald, S. A. *et al.* Solution-processed PbS quantum dot infrared photodetectors and photovoltaics. *Nature Mater.* **4,** 138–142 (2005).
4. Fossum, E. R. CMOS image sensors: electronic camera-on-a-chip. *IEEE Trans. Electron. Dev.* **44,** 1689–1698 (1997).
5. Yu, G., Gao, J., Hummelen, J. C., Wudl, F. & Heeger, A. J. Polymer photovoltaic cells: enhanced efficiencies via a network of internal donor–acceptor heterojunctions. *Science* **270,** 1789–1791 (1995).
6. Schmitt, J. M., Xiang, S. H. & Yung, K. M. Differential absorption imaging with optical coherence tomography. *J. Opt. Soc. Am. A* **15,** 2288–2296 (1998).
7. Barton, J. B., Cannata, R. F. & Petronio, S. M. InGaAs NIR focal plane arrays for imaging and DWDM applications. *Proc. SPIE* **4721,** 37–47 (2002).
8. Källhammer, J.-E. Imaging: The road ahead for car night-vision *Nature Photon.* 12–13 (2006).
9. Chu, L., Zrenner, A., Böhm, G. & Abstreiter, G. Normal-incident intersubband quantum dots photocurrent spectroscopy on InAs/GaAs. *Appl. Phys. Lett.* **75,** 3599–3601 (1999).
10. Liu, H. C. *et al.* A study of GaAs/AlGaAs p-type quantum well infrared photodetectors with different barrier heights. *J. Appl. Phys.* **83,** 585–587 (1998).
11. Hwang, I. W. *et al.* Ultrafast electron transfer and decay dynamics in a small band gap bulk heterojunction material. *Adv. Mater.* **19,** 2307–2312 (2007).
12. Yao, Y. *et al.* Plastic near-infrared photodetectors utilizing low band gap polymer. *Adv. Mater.* **19,** 3979–3983 (2007).
13. Natali, D., Sampietro, M., Arca, M., Denotti, C. & Devillanova, F. A. Wavelength-selective organic photodetectors for near-infrared applications based on novel neutral ditholenes. *Synth. Met.* **137,** 1489–1490 (2003).
14. Böberl, M., Kovalenko, M. V., Gamerith, S., List, E. J. W. & Heiss, W. Inkjet-printed nanocrystal photodetectors operating up to 3 μm wavelengths. *Adv. Mater.* **19,** 3574–3578 (2007).
15. Johnston, K. W. *et al.* Schottky-quantum dot photovoltaics for efficient infrared power conversion. *Appl. Phys. Lett.* **92,** 151115 (2008).
16. Yu, G., Yong, C., Wang, J., McElvain, J. & Heeger, A. J. High sensitivity polymer photosensors for image sensing applications. *Synth. Met.* **102,** 904–907 (1999).
17. Ng, T. N., Wong, W. S., Chabinyc, M. L., Sambandan, S. & Street, R. A. Flexible image sensor array with bulk heterojunction organic photodiode. *Appl. Phys. Lett.* **92,** 213303 (2008).
18. Tedde, S., Zaus, E., Fuerst, J., Henseler, D. & Lugli, P. Active pixel concept combined with organic photodiode for imaging devices. *IEEE Electron. Dev. Lett.* **28,** 893–895 (2007).
19. Ilan Gur, I., Fromer, N. A., Geier, M. L. & Paul Alivisatos, A. P. Air-stable all-inorganic nanocrystal solar cells processed from solution. *Science* **310,** 462–465 (2005).
20. Oertel, D. C., Bawendi, M. G., Arango, A. C. & Bulović, V. Photodetectors based on treated CdSe quantum-dot films. *Appl. Phys. Lett.* **87,** 213505 (2005).
21. Schilinsky, P., Waldauf, C. & Brabec, C. J. Recombination and loss analysis in polythiophene based bulk heterojunction photodetectors. *Appl. Phys. Lett.* **81,** 3885–3887 (2002).
22. Sariciftci, N. S., Smilowitz, L., Heeger, A. J. & Wudl, F. Photoinduced electron transfer from a conducting polymer to buckminsterfullerene. *Science* **258,** 1474–1476 (1992).
23. Soci, C. *et al.* Photoconductivity of a low-bandgap conjugated polymer. *Adv. Funct. Mater.* **17,** 632–636 (2007).
24. Szendrei, K. *et al.* Solution-processable near infrared photodetectors based on electron transfer from PbS nanocrystals to fullerene derivatives. *Adv. Mater.* DOI: 10.1002/adma (adma.200801752).
25. Biebersdorf, A. *et al.* Semiconductor nanocrystals photosensitize C60 crystals. *Nano Lett.* **6,** 1559–1563 (2006).
26. Bawendi, M., Steigerwald, M. L. & Brus, L. E. The quantum mechanics of larger semiconductor clusters ('Quantum Dots'). *Ann. Rev. Phys. Chem.* **41,** 477–496 (1990).
27. Cademartiri, L. *et al.* Size-dependent extinction coefficients of PbS quantum dots. *J. Am. Chem. Soc.* **128,** 10337–10346 (2006).
28. Hines, M. A. & Scholes, G. D. Colloidal PbS nanocrystals with size-tuneable near-infrared emission: observation of post-synthesis self-narrowing of the particle size distribution. *Adv. Mater.* **15,** 1844–1849 (2003).
29. Paetzold, R., Winnacker, A., Henseler, D., Cesari, V. & Heuser, K. Permeation rate measurements by electrical analysis of calcium corrosion. *Rev. Sci. Instrum.* **74,** 5147–5150 (2003).
30. Sitter, D. N., Goddard, J. S. & Ferrell, R. K. Method for the measurement of the modulation transfer function of sampled imaging systems from bar-target patterns. *Appl. Opt.* **34,** 746–751 (1995).

Acknowledgements

W.H. and M.K. are grateful for support from the Austrian Science Fund FWF (projects START Y179 and SFB-Iron).

Additional information

Supplementary information accompanies this paper at www.nature.com/naturephotonics. Reprints and permission information is available online at http://npg.nature.com/reprintsandpermissions/. Correspondence should be addressed to T.R. and requests for materials should be addressed to O.H.

nature photonics

LETTERS

PUBLISHED ONLINE: 17 MAY 2009 | DOI: 10.1038/NPHOTON.2009.75

Observing angular deviations in the specular reflection of a light beam

M. Merano, A. Aiello†, M. P. van Exter and J. P. Woerdman*

The Law of Reflection of a light ray incident upon a mirror ($\theta_{in} = \theta_{out}$) was first formulated by Euclid around 300 BC in his book *Catoptrics*[1]; it has been a tenet of geometrical optics ever since. However, more recently, a small angular deviation of the Law of Reflection has been predicted for a physical light beam when this is regarded as the implementation of a ray[2–5]. The deviation is a diffractive consequence of the angular dependence of the reflectivity and should occur for any mirror with less than 100% reflectivity. We report here experimental proof of this angular deviation by determining the direction of an optical beam after reflection from an air–glass interface, using a position detector with nanometre resolution. Our results are relevant for angular metrology in general and cantilever-based surface microscopies in particular. Analogous angular deviations are expected for reflection of acoustic waves and quantum matter waves.

The reflection of a light beam by a planar dielectric interface has intriguing characteristics that have long been the subject of study[6,7]. Interest has mainly focused on the Goos–Hänchen (GH) shift, which is a positional shift of the beam centre relative to its geometrical optics position[6]. The GH shift is proportional to the angular derivative of the phase of the complex reflectivity r, and occurs in particular under conditions of total internal reflection (TIR), where this derivative can become large[7]. The GH shift has been studied in photonic crystals, plasmonics, near-field optics, nonlinear optics, negative-index media, acoustics and atom optics[8–17].

There is a relatively unknown related effect, namely an angular deviation of the beam axis that occurs only in the case of partial, that is, non-total reflection[2–4,18,19]. This angular shift is proportional to the angular derivative of the amplitude reflectivity $|r|$. Currently available theory[2–4] is deficient in describing this because it addresses a two-dimensional geometry with sheet-shaped light beams; as we show here, a full three-dimensional treatment is essential for incidence near the Brewster angle. Experimentally, angular deviation has been studied in the microwave domain[19]. We report here the first experimental observation of angular deviation in the optical domain and compare this with theory that takes into account the three-dimensional nature of the beam. The optical domain is particularly relevant in view of the importance of optical methodology in science and engineering.

Theoretically, we calculated the magnitude of the angular shift using the intensities and not the amplitudes of the plane waves that constitute the beam. This simplification is valid because only one plane wave contributes to the far field at a given angle, the effect of the other plane waves being cancelled by destructive interference[20] (our experiments are indeed in the far field, as is apparent in the following). For the positional (GH) shift that occurs in the near field, such an intensity-based treatment would be wrong. We have also constructed a general, amplitude-based theory, showing

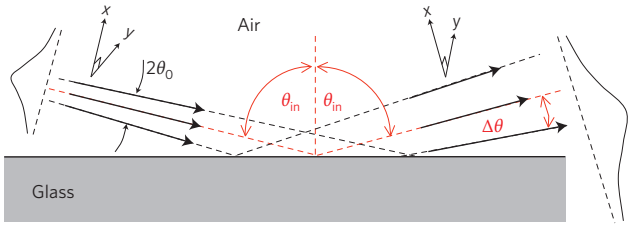

Figure 1 | Schematic representation of non-specular angular reflection. A TEM_{00} Gaussian beam hits an air–glass interface; the beam is modelled as a bundle of rays with a full opening angle $2\theta_0$ and with θ_{in} as the central angle of incidence. Transverse beam coordinates are indicated as (x, y), where x is in the plane of incidence and y perpendicular to it. The reflectivity of a given ray depends on its angle of incidence; the length of a ray arrow symbolizes the ray intensity before and after reflection. The angular deviation of the axis of the reflected beam relative to the specular direction is labelled as $\Delta\theta$.

that the angular and positional shifts are, respectively, the imaginary and real parts of a complex-valued analytical function[5,18]. This theory reduces in the far field to the more intuitively based intensity approach that we present here.

We introduce in Fig. 1 a TEM_{00} beam of wavelength λ, waist parameter w_0 and angular half-width θ_0; these parameters are related by the relation $\theta_0 = 2/(kw_0)$, where $k = 2\pi/\lambda$ (ref. 20). We decompose the intensity of this beam into plane waves ('rays') travelling at angles θ_x and θ_y relative to the beam axis

$$I\left(\theta_x, \theta_y\right) \propto \exp\left[-2\left(\theta_x^2 + \theta_y^2\right)/\theta_0^2\right] \qquad (1)$$

Introducing $R(\theta_x, \theta_y)$ as the intensity reflection coefficient of the plane wave (θ_x, θ_y), we denote the reflected beam as $R(\theta_x, \theta_y)I(\theta_x, \theta_y)$. We define the ('centre-of-mass') angular deviation of the reflected beam, in the plane of incidence as

$$\langle \Delta\theta_x \rangle = \frac{\iint \theta_x R\left(\theta_x, \theta_y\right) I\left(\theta_x, \theta_y\right) \mathrm{d}\theta_x \, \mathrm{d}\theta_y}{\iint R\left(\theta_x, \theta_y\right) I\left(\theta_x, \theta_y\right) \mathrm{d}\theta_x \, \mathrm{d}\theta_y} \qquad (2)$$

The input beam is assumed to be linearly polarized, either s or p (respectively perpendicular or parallel to the plane of incidence). We first assume p-polarization. The finite divergence of the beam unavoidably implies a small admixture of s-polarization; this leads to the expression (see Supplementary information)

$$\langle \Delta\theta_p \rangle \approx \frac{R_p' \theta_0^2}{4R_p + (1/2)R_p''(1+\varepsilon)\theta_0^2} \quad \text{with} \quad \varepsilon \equiv \frac{2\left(R_s - R_p\right)}{R_p'' \tan^2 \theta_{in}} \qquad (3)$$

Huygens Laboratory, Leiden University, PO Box 9504, 2300RA Leiden, The Netherlands; †Present address: Max Planck Institute for the Science of Light, Günther-Scharowsky-Strasse 1/Bau 24, 91058 Erlangen, Germany. *e-mail: woerdman@molphys.leidenuniv.nl

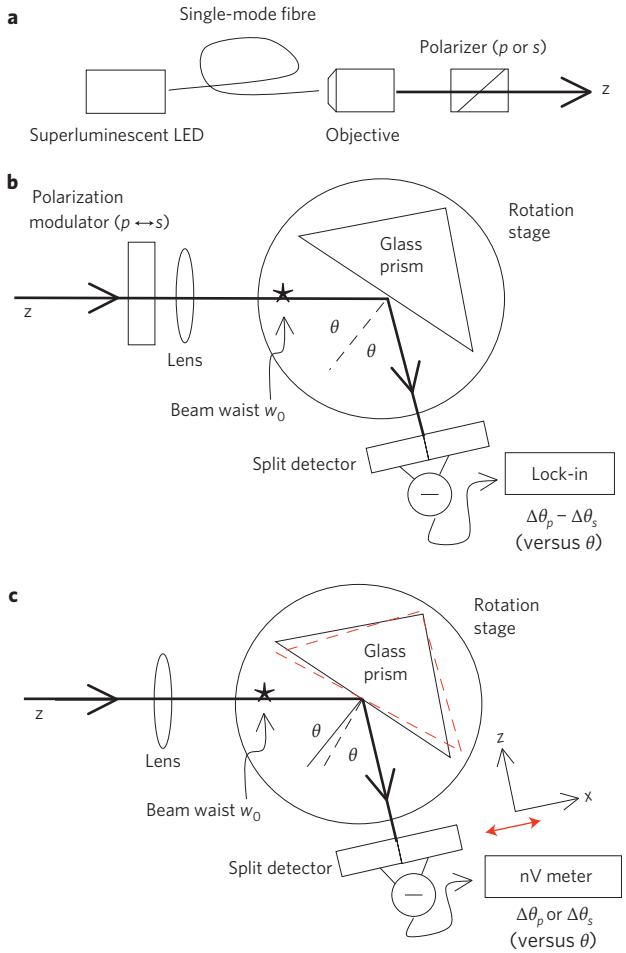

Figure 2 | Experimental set-up. a, Light source. The output of a superluminescent light-emitting diode (SLED) is spatially filtered by a single-mode optical fibre to select the TEM_{00} mode. This is converted into a collimated beam by a microscope objective. The collimated beam is passed through a polarizer to select *p*-polarization. **b**, Set-up to measure non-specular reflection over a wide range of incident angles. Reflection takes place at the surface of a right-angle BK7 glass prism ($n = 1.51$). The (folded) optical axis of the set-up is indicated by *z*. Technical noise is suppressed by switching the polarization of the incident beam between *p* and *s*, followed by synchronous detection of the signal produced by the split detector. This yields the difference of the angular deviation for *p* versus *s* polarization. **c**, Set-up to measure non-specular reflection near the Brewster angle. The incident beam is *p*-polarized. Technical noise is suppressed by using a nulling method: a small, controlled rotation of the glass prism leads to an unbalance of the split detector, which is then nulled by a controlled lateral (*x*) shift of the detector. From the magnitude of this nulling shift we deduce the angular deviation.

Here the suffix *x* in $\langle\Delta\theta_x\rangle$ has been suppressed, R_p and R_s are, respectively, the plane-wave *p* and *s* intensity reflectivities, the partial derivatives of R_p are taken in the θ_x direction (at θ_{in}), and ε accounts for the effect of the *s*-admixture. This admixture becomes relatively important for incidence close to the Brewster angle. If we assume an *s*-polarized input beam, the *p*-admixture has negligible effect:

$$\langle\Delta\theta_s\rangle \approx \frac{R_s'}{4R_s}\theta_0^2 \qquad (4)$$

In the geometrical optics limit ($\lambda \to 0$ or $w_0 \to \infty$) we have $\theta_0 \to 0$, so according to equations (3) and (4) the angular deviation vanishes.

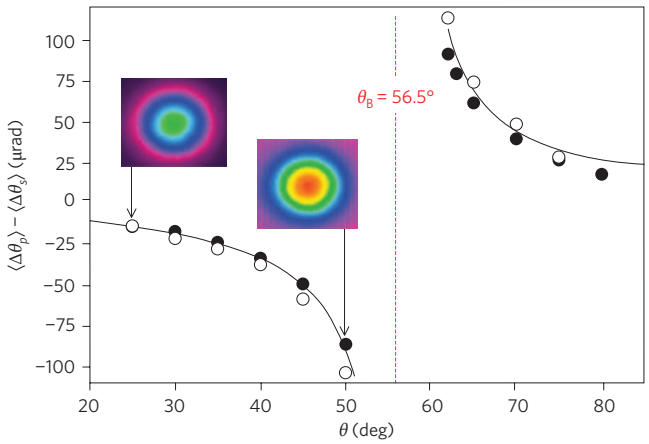

Figure 3 | Angular deviation far from the Brewster angle θ_B. The theoretical curve gives the angular deviation ($\langle\Delta\theta_p\rangle - \langle\Delta\theta_s\rangle$) versus the angle of incidence θ, as deduced from equations (4) and (6). The brackets $\langle\cdots\rangle$ refer to averaging over the angular beam profile. Experimental data were obtained with the set-up of Fig. 2b for two independent experimental runs (open and filled circles), both for a beam waist $w_0 = 59$ μm. The inserts show the observed intensity profile of the reflected beam at $\theta = 25°$ and 50°.

For a *p*-polarized input beam two special cases of equation (3) can be distinguished. First, if the input beam is incident near the Brewster angle θ_B we have R_p proportional to $(\theta_{in} - \theta_B)^2$. This leads to a dispersive resonance in the angular deviation (see Supplementary information)

$$\langle\Delta\theta_p\rangle = \frac{2(\theta_{in} - \theta_B)\theta_0^2}{4(\theta_{in} - \theta_B)^2 + (1+\varepsilon)\theta_0^2} \quad \text{with} \quad \varepsilon = \frac{4n^4}{(1+n^2)^4} \qquad (5)$$

and to a deviation of the reflected beam profile from TEM_{00} (see below). In our experiment $n = 1.51$, leading to $\varepsilon = 0.18$. In the second case the input angle is assumed to be sufficiently far from the Brewster angle, that is, $|\theta_{in} - \theta_B| \gg \theta_0$, leading to

$$\langle\Delta\theta_p\rangle = \frac{R_p'}{4R_p}\theta_0^2 \qquad (6)$$

In this case the deviation of the reflected beam profile from TEM_{00} is very small. Numerically we find that the deviation is less than 1% for $|\theta_{in} - \theta_B| > 2\theta_0$.

We now turn to the experimental set-up shown in Fig. 2 (see Methods for details). We used a TEM_{00} Gaussian light beam with $\lambda = 820$ nm (Fig. 2a). A lens transforms the waist parameter w_0 to a desired value at a *z*-position indicated by the asterisk in Fig. 2b. The beam is then reflected by an air–glass interface and its transverse (*x*) position is measured with a calibrated split detector. The set-up operated in the far field—the distance between the detector and the beam waist being chosen to be at least 10 times larger than the Rayleigh range $\pi(w_0)^2/\lambda$. We switched the incident polarization between *p* and *s* (Fig. 2b) and used synchronous detection to deduce the polarization-differential angular shift of the beam, $\langle\Delta\theta_p\rangle - \langle\Delta\theta_s\rangle$. This was done as a function of the angle of incidence θ (from now on we suppress the suffix 'in' of θ_{in}). Figure 3 shows the data for $\theta = 20$–$80°$ at $w_0 = 59$ μm; the agreement with the theoretical curve based upon equation (4) and (6) is very good (there are no fit parameters). The dispersive singularity at $\theta = \theta_B$ is due to the $\Delta\theta_p$ divergence in equation (6) at $R_p \to 0$. The inserts in Fig. 3 show measured intensity profiles of the reflected beam. We find that for the incident angles θ involved, the reflected beam remains TEM_{00} within experimental accuracy (~1%).

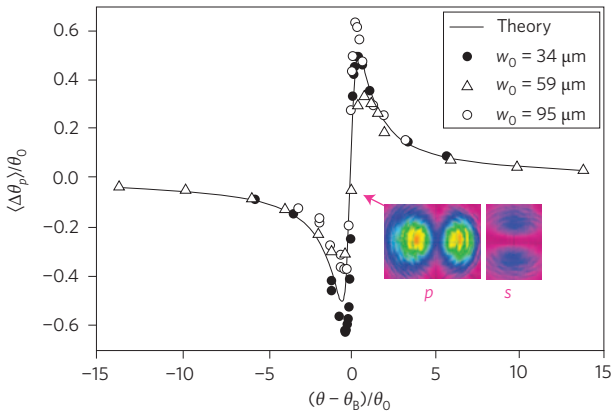

Figure 4 | Angular deviation near the Brewster angle θ_B. The curve shows the theoretical prediction of equation (5) for the angular deviation $\langle\Delta\theta_p\rangle$ versus the angle of incidence θ. The brackets $\langle\cdots\rangle$ refer to averaging over the angular beam spread. Abscissa and ordinate have been made dimensionless by dividing by θ_0, the half-opening angle of the incident TEM_{00} beam. Experimental data were obtained with the set-up of Fig. 2c for three values of the beam waist w_0. The insert shows the polarization-analysed reflected intensity profiles of a beam ($w_0 = 34$ μm) incident at $\theta = \theta_B = 56.5°$.

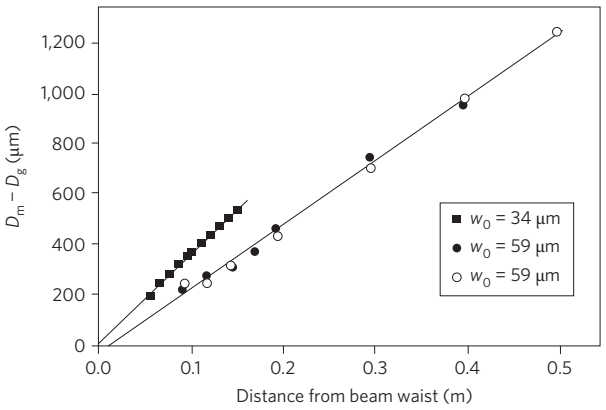

Figure 5 | Verification of the angular nature of the deviation. We plot here $(D_m - D_g)$ as a function of the distance between the beam waist (at the asterisk in Fig. 2c) and the split detector. Experimental data are presented for two values of the beam waist, $w_0 = 34$ and 59 μm, in the latter case for two independent experimental runs. D_m is the beam position measured on the split detector and D_g the corresponding geometrical optics position. For measuring the latter we remove the lens from the set-up of Fig. 2c so that we deal with a collimated incident beam with a very large beam waist, $w_0 = 1.64$ mm; this represents the geometrical optics limit. Spurious shifts due to removing the lens are prevented by ensuring that the lens, before removing it, is exactly centred on the beam; for this centring we use a separate quadrant detector.

We also measured the angular deviation much closer to the Brewster angle ($\theta_B = 56.5°$), now using now the set-up of Fig. 2c where the incident polarization was fixed as *p*. We effectively calibrated the split detector by means of a small, controlled rotation of the air–glass interface which was nulled by a lateral (x) shift of the detector. In Fig. 4 we plot the theoretical prediction of equation (5) as $\langle\Delta\theta_p\rangle/\theta_0$ versus $(\theta - \theta_B)/\theta_0$. In this dimensionless form the dispersive resonance curve is universal in the sense that it is independent of the beam divergence θ_0; the extrema have coordinates (0.5, 0.5) and (–0.5, –0.5). The theory is nicely confirmed by the experimental data for three values of the beam waist $w_0 = 2/(k\theta_0)$. In absolute terms, the measured angular deviation varies between 10^{-5} and 10^{-2} rad.

The inserts in Fig. 4 show the measured polarization-analysed intensity profiles of the reflected beam when the (*p*-polarized) input beam is incident at exactly the Brewster angle. In this case the reflected profile differs greatly from the TEM_{00} input profile. The reflected intensity shows a double-peak structure (this has been observed before[21,22]); according to our theory this is in fact a superposition of a *p*-polarized TEM_{01} profile and an *s*-polarized TEM_{10} profile (see Supplementary information). For the ratio of the corresponding beam powers P_s and P_p at Brewster incidence, our theory gives $(P_s/P_p)_B = \varepsilon = 0.18$ (ε is defined in equation (5)). This value agrees well with our experimental result: $(P_s/P_p)_B = 0.20 \pm 0.05$.

According to our theory the angular deviation is centred at the position of the beam waist and not, as one might naively think, on the glass surface. This can be tested in the set-up of Fig. 2c, where we introduce D_m and D_g as the beam's actual x-position and its geometrical-optics x-position, respectively, both measured at the split detector. Figure 5 shows the differential x-shift $(D_m - D_g)$ measured this way as a function of the distance z between the detector and the beam waist, for two values of the waist. For both values we find proportionality between $(D_m - D_g)$ and θ_{in}, thus confirming the angular nature of the effect.

We emphasize that each plane-wave solution in the angular expansion is governed by Maxwell's equations in the regular manner. The boundary conditions associated with momentum conservation and Snell's Law are satisfied as usual when considering all three plane waves: the incident one, the reflected one and the transmitted (= refracted) one. The fact that in the beam case the (average) in-plane momentum of a reflected photon is different from that of an incident photon does not contradict momentum conservation; the difference is balanced by an opposite difference associated with the transmitted beam (see Supplementary information).

The three key elements required for the occurrence of angular non-specularity can be simply understood in a qualitative sense. The first requirement is a finite-diameter optical beam, because this produces a wavevector spread (due to diffraction). The second is less than 100% reflection, because this leads generally to an angular dependence of the reflectivity (which cannot occur for $R(\theta) = 100\%$). Within a given beam, the more oblique rays then have a different intensity reflectivity than the less oblique ones. This unbalance slightly rotates the centre-of-mass axis of the reflected beam away from the geometrical-optics angle (see Fig. 1). The third requirement is oblique incidence, because at normal incidence the angular deviation vanishes for symmetry reasons.

These three elements occur quite generally in optical implementations of angular metrology. The resulting angular deviation, even if very small, produces, by means of propagation, an unlimited growth in the transverse positional coordinate[5]. This may occur in geodetic surveying, machine-tool operation, torsion pendulum readout[23] and cantilever-based surface microscopies (such as atomic force microscopy, AFM)[24]. Another example is the angular alignment of gravitational wave detectors such as LIGO (a Michelson interferometer where one deals with oblique incidence on a 50%/50% beamsplitter) or LISA (basically a triangular interferometer)[25].

For simplicity we have emphasized in our work the case of an air–glass interface with its associated Brewster resonance. However, angular non-specularity should occur generally for multilayer dielectric stacks and for metal mirrors (which have <100% reflectivity). Moreover, it should also occur in acoustics[16] and quantum mechanics[12], where we deal with scalar waves instead of electromagnetic vector waves. In the scalar case the Brewster resonance does not contribute, so the angular shift is governed by equations (4) and (6) with $R_s(\theta) = R_p(\theta)$. Finally, an argument for the potential impact of angular non-specularity is that the study of its positional 'cousin', namely the GH effect, has broadly

ramified[8–17] (over 300 papers in 1947–2008). It would also be interesting to explore (some of) these issues for the angular case.

Methods

Our light source was a temperature-controlled fibre-pigtailed superluminescent light-emitting diode (SLED) with $P = 2$ mW, $\lambda = 820$ nm and $\Delta\lambda = 25$ nm (InPhenix IPSDD0802). Its large spectral width (compared to a diode laser) helped to eliminate coherent speckle formation in the rest of the optical train; such speckle can easily compromise the high-precision position measurements of a beam. Another advantage of a SLED when compared to a diode laser is the absence of higher-order transverse modes; this leads to superior beam pointing stability (no mode competition). The output of the SLED was sent through a single-mode optical fibre that acted as a spatial filter; the output facet of the fibre was positioned at the focus of a microscope objective (×10). This objective produced a collimated (TEM_{00}) light beam with a Gaussian waist parameter $w_0 = 1.64$ mm. This was passed through a polarizer to select p-polarization, resulting in a useful power of typically 900 μW.

For polarization switching ($p \leftrightarrow s$) of the beam we used a liquid-crystal variable retarder (MeadowLark Optics) with a negligible parasitic angular modulation (<0.3 μrad). The set-up shown in Fig. 2b could not be used near Brewster incidence on the glass prism because depolarization by the liquid-crystal device, although small ($\sim 1 \times 10^{-3}$), prevented measurement of the reflectivity near its Brewster minimum ($R = 1 \times 10^{-5} - 1 \times 10^{-6}$). Another limitation of the polarization switching method near Brewster incidence is the very large difference in p- and s-polarized beam powers; this introduces errors in the measured beam position due to the (weak) nonlinearity of the response of the split detector.

Near Brewster incidence we used the nulling technique shown in Fig. 2c. We took advantage of the fact that close to θ_B the angular deviation of a p-polarized beam shows a strong dependence on the angle of incidence (Fig. 4). Starting from an angle of incidence θ_{start} in the far wing of the resonance (for example, $\theta_B - \theta_{start} = 3^\circ$) we rotated the prism by a quantity $\delta\theta$ (for example, 0.1°) and translated (x) the split detector until we reached the new position of the centre of the reflected beam (Fig. 2c). By repeating this measurement with stepwise increments $\delta\theta$, thus scanning the complete resonance, we reconstructed the curve $\langle\Delta\theta\rangle_{(\theta)} - \langle\Delta\theta\rangle_{(\theta start)}$, which is the desired dependence $\langle\Delta\theta\rangle_{(\theta)}$ apart from an offset $\langle\Delta\theta\rangle_{(\theta start)}$. For this (experimentally unknown) offset we took the value given by equation (6).

For verification of the angular nature of the deviation from geometrical optics (Fig. 5) we again used the nulling method, but without scanning across a whole range of θ values, instead using two values only. We took care to choose these angles, θ_1 and $\theta_2 \equiv \theta_1 + \delta\theta$, on opposite sites of θ_B. In this way we measured for a small $\delta\theta$ a strong deviation from geometrical optics (due to the zero crossing at θ_B the contributions at the two angles of incidence sum) so that we could increase z to 50 cm without exceeding the travel distance of the translation stage on which the split detector was mounted.

We used a large prism, with sides and height of 40 mm, to avoid the situation where multiple reflections of the transmitted beam would hit a prism edge (hitting an edge gives rise to scattered light that can unbalance the split detector). Reproducible results for the angular deviation and the beam profile could only be obtained by regularly cleaning the hypotenuse plane of the prism, in particular when the beam was incident near the Brewster angle. The prism was mounted on a precision rotation stage with a resolution of 9 μrad (Newport URS-BCC). This resolution is at least 10 times better than that required for resolving the Brewster resonance using the nulling method.

We note that a split detector measures in principle the median position instead of the centre-of-mass position of the intensity distribution. This distinction is only relevant close to Brewster incidence where the reflected beam profile differs from Gaussian. However, in this case, numerical simulation shows that, within our limited experimental accuracy (see Fig. 4), the median position coincides with the centre-of-mass position, even for $\theta = \theta_B$.

Our split detector was implemented by pairwise binning of the photodiodes of a quadrant detector (NewFocus 2901). The overall size of the detector was 3 × 3 mm and its photodiodes were separated by a gap of 100 μm. The detector was mounted on a linear translation stage (Newport LTA-HL, resolution 100 nm) orthogonal to the reflected beam. For a step size of $\delta\theta = 0.1^\circ$, the beam displacement at the detector was typically $D = 150$–300 μm, which can be measured in practice with a precision of 1–2 μm.

When working near θ_B, the reflected light power P_p was very low (typically $P_p = 1$–10 nW at θ_B). In this case the voltage offset of the preamplifier of the split detector acted as an error source for the beam positioning in the nulling method. A nanovoltmeter (Keithley 181) was used to read the voltage signal from the preamplifier. Before looking for the beam position, the voltage offset was measured (typically 300 μV) and a corresponding zero set on the nanovoltmeter. The temporal stability of the voltage offset was 2–4 μV, corresponding to a beam positioning resolution of 5–10 μm at the lowest reflected power.

Received 1 February 2009; accepted 22 April 2009; published online 17 May 2009

References

1. Hecht, E. *Optics* 4th edn, 1 (Addison-Wesley, 2002).
2. Ra, J. W., Bertoni, H. L. & Felsen, L. B. Reflection and transmission of beams at a dielectric interface. *SIAM J. Appl. Math.* **24,** 396–413 (1973).
3. Antar, Y. M. & Boerner, W. M. Gaussian beam interaction with a planar dielectric interface. *Can. J. Phys.* **52,** 962–972 (1974).
4. Chan, C. C. & Tamir, C. Angular shift of a Gaussian beam reflected near the Brewster angle. *Opt. Lett.* **10,** 378–380 (1985).
5. Aiello, A. & Woerdman, J. P. Role of beam propagation in Goos–Hänchen and Imbert–Fedorov shifts. *Opt. Lett.* **33,** 1437–1439 (2008).
6. Goos, F. & Hänchen, H. Ein neuer und fundamentaler Versuch zur Totalreflexion. *Ann. Phys.* (*Leipzig*) **1,** 333–346 (1947).
7. Artmann, K. Berechnung der Seitenversetzung des totalreflektierten Strahles. *Ann. Phys.* **2,** 87–102 (1948).
8. Bonnet, C., Chauvat, D., Emile, O., Bretenaker, F. & Le Floch, A. Measurement of positive and negative Goos–Hänchen effects for metallic gratings near Wood anomalies. *Opt. Lett.* **26,** 666–668 (2001).
9. Berman, P. R. Goos–Hänchen shifts in negatively refracting media. *Phys. Rev. E* **66,** 067603 (2002).
10. Bliokh, K. Y., Shadrivov, I. V. & Kivshar, Y. S. Goos–Hänchen and Imbert–Fedorov shifts of polarized vortex beams. *Opt. Lett.* **34,** 389–391 (2009).
11. Jost, B. M., Al-Rashed, A. A. R. & Saleh, B. E. A. Observation of the Goos–Hänchen effect in a phase-conjugate mirror. *Phys. Rev. Lett.* **81,** 2233–2235 (1998).
12. Huang, J., Duan, Z., Ling, H. & Zhang, W. Goos–Hänchen-like shifts in atom optics. *Phys. Rev. A* **77,** 063608 (2008).
13. Felbacq, D., Moreau, A. & Smaâli, R. Goos–Hänchen effect in the gaps of photonic crystals. *Opt. Lett.* **28,** 1633–1635 (2003).
14. Emile, O., Galstyan, T., Le Floch, A. & Bretenaker, F. Measurement of the nonlinear Goos–Hänchen effect for Gaussian optical beams. *Phys. Rev. Lett.* **75,** 1511–1514 (1995).
15. Yin, X. & Hesselink, L. Large positive and negative lateral optical beam displacements due to surface plasmon resonance. *Appl. Phys. Lett.* **85,** 372–374 (2004).
16. Gragg, R. F. The total reflection of a compact wave group: Long-range transmission in a waveguide. *Am. J. Phys.* **56,** 1092–1094 (1988).
17. Merano, M. *et al.* Observation of Goos–Hänchen shifts in metallic reflection. *Opt. Express* **15,** 15928–15934 (2007).
18. Aiello, A. & Woerdman, J. P. Theory of angular Goos–Hänchen shift near Brewster incidence. Preprint at <http://arxiv.org/pdf/0903.3730>.
19. Müller, D., Tharanga D., Stahlhofen, A. A. & Nimtz, G. Nonspecular shifts of microwaves in partial reflection. *Europhys. Lett.* **73,** 526–532 (2006).
20. Mandel, L. & Wolf, E. *Optical Coherence and Quantum Optics* Vol. 143, 271 (Cambridge Univ. Press, 1995).
21. Fainman, Y. & Shamir, J. Polarization of nonplanar wavefronts. *Appl. Opt.* **23,** 3188–3195 (1984).
22. Li, Q. & Vernon, R. J. Theoretical and experimental investigation of Gaussian beam transmission and reflection by a dielectric slab at 110 GHz. *IEEE Trans. Antennas Propag.* **54,** 3449–3457 (2006).
23. Mueller, F., Heugel, S. & Wang, L. J. Femto-newton light force measurement at the thermal noise limit. *Opt. Lett.* **33,** 539–541 (2008).
24. Putman, C. A. J., De Grooth, B. G., Van Hulst, N. F. & Greve, J. A theoretical comparison between interferometric and optical beam deflection technique for the measurement of cantilever displacement in AFM. *Ultramicroscopy* **42,** 1509–1513 (1992).
25. Centrella, J. M. Resource letter: GrW-1: Gravitational waves. *Am. J. Phys.* **71,** 520–524 (2003).

Acknowledgements

This work was supported by the Netherlands Foundation for Fundamental Research of Matter (FOM) and by the Seventh Framework Programme for Research of the European Commission, under the FET-Open grant agreement HIDEAS, no. FP7-ICT-221906. We acknowledge E.R. Eliel and G.'t Hooft for useful discussions.

Additional information

Supplementary information accompanies this paper at www.nature.com/naturephotonics. Reprints and permission information is available online at http://npg.nature.com/reprintsandpermissions/. Correspondence and requests for materials should be addressed to J.P.W.

nature photonics

ARTICLES

PUBLISHED ONLINE: 24 MAY 2009 | DOI: 10.1038/NPHOTON.2009.92

High-performance crosslinked colloidal quantum-dot light-emitting diodes

Kyung-Sang Cho[1], Eun Kyung Lee[1], Won-Jae Joo[2], Eunjoo Jang[2], Tae-Ho Kim[1], Sang Jin Lee[1], Soon-Jae Kwon[2], Jai Yong Han[3], Byung-Ki Kim[2], Byoung Lyong Choi[1]* and Jong Min Kim[1]

Colloidal quantum-dot light-emitting diodes have recently received considerable attention due to their ease of colour tunability, high brightness and narrow emission bandwidth. Although there have been rapid advances in luminance, efficiency and lifetime, device performance is still limited by the large energy barriers for hole and electron injection into the quantum-dot layer. Here, we show that by crosslinking the colloidal quantum-dot layer, the charge injection barrier in a red-light-emitting quantum-dot light-emitting diode may be considerably reduced by using a sol–gel TiO_2 layer for electron transport. The device architecture is compatible with all-solution device fabrication and the resulting device shows a high luminance (12,380 cd m^{-2}), low turn-on voltage (1.9 V) and high power efficiency (2.41 lm W^{-1}). Incorporation of the technology into a display device with an active matrix drive backplane suggests that the approach has promise for use in high-performance, easy-to-fabricate, large-area displays and illumination sources.

Since the first report on colloidal quantum-dot light-emitting diodes (QD-LEDs) in 1994, various approaches have been followed to improve the performance of these devices, including the design of novel device structures, the development of novel QD and transport materials, and the optimization of carrier injection[1–12]. Compared to early structures, which had thick QD layers that acted both as emissive and electron transport layers (ETL)[1,3,4], the luminous efficiency of QD-LEDs has been vastly improved by the use of ordered arrays of QD monolayers[5] that minimize electrical resistance and enable efficient confinement of excitons. As a result, devices with QD monolayers demonstrate record levels of luminance (2,000 cd m^{-2}) and luminous efficiency (1.9 cd A^{-1}). Recent work by other groups has shown that even better QD-LED performance (a maximum luminance of 9,034 cd m^{-2} and luminous efficiency of 2.8 cd A^{-1}) could be achieved by optimizing the thickness of the QD layer and QD purification[11]. Much effort has been made to replace the organic charge transport layers of QD-LEDs with inorganic ones to overcome the persistent drawbacks of organic materials, in particular their thermal instability and moisture/oxygen-induced degradation[9,10,12]. Recently, a colloidal QD-LED with inorganic charge transport layers[12] consisting of a NiO hole transport layer (HTL) and a doped ZnO ETL showed a reasonable maximum luminance of 1,950 cd m^{-2} compared to all-organic-based QD-LEDs, but the luminous efficiency was still low (0.064 cd A^{-1}). Further development of colloidal QD-LEDs featuring inorganic layers could potentially allow for the realization of encapsulation-free QD-LEDs with long lifetimes.

Although the performance of colloidal QD-LEDs has improved dramatically in recent years, control over carrier injection, electron–hole recombination and carrier balance still requires improvement before commercialization. Commonly used II–VI colloidal QDs have intrinsically high valence levels (>6.5 eV); this creates a large potential barrier between the QD valence level and that for the typical transparent anode, ITO (4.5–5.1 eV). This is perhaps the major factor limiting QD-LED performance. Here, we show that crosslinking the QD layer can shift its valence band, thus reducing the band offset with the HTL and substantially improving charge injection. Additionally, thermal annealing of the crosslinked QD layer further improves device luminance and luminous efficiency due to a decrease in the contact resistance through the removal of organic residues in the QD layer. We investigated these treatments and their effect on device performance using a combination of ultraviolet photoelectron spectroscopy (UPS), photoluminescence (PL), thermogravimetric analysis (TGA) and electroluminescence (EL) characteristics.

Results and discussion

Structural design of the QD-LED. A schematic of the device structure and cross-sectional transmission electron microscopy (TEM) image of the QD-LED and corresponding energy band diagram are shown in Fig. 1. The device consists of a patterned ITO anode, a 50-nm poly(ethylenedioxythiophene):polystyrene sulphonate (PEDOT:PSS) hole injection layer (HIL), a 20-nm poly[(9,9-dioctylfluorenyl-2,7-diyl)-co-(4,4′-(*N*-(4-sec-butylphenyl)) diphenylamine)] (TFB) layer as the HTL, a 30-nm QD layer as the emissive layer, a 40-nm TiO_2 layer as the ETL and a 150-nm aluminium layer as the cathode. Highly luminescent, red-light-emitting (PL = 615 nm) CdSe/CdS/ZnS QDs ($\eta_{PL} > 70\%$) were prepared according to a previously reported method[14]. Our QD-LED structure was designed to achieve efficient electron and hole injection from the electrodes to the QDs. We also wanted to effectively block electrons and holes that pass through the QD layer in consideration of the electronic band structure of the constituent layers (Fig. 1b). A small injection barrier of 0.4 eV exists for the injection of electrons from aluminium to the QD layer because the TiO_2 conduction band (3.9 eV; see Supplementary Fig. S1) and the work functions of aluminium are similar. The small step alignment of the highest occupied molecular orbital (HOMO) energy levels of PEDOT and TFB allows for facile injection of holes from the ITO to the QD layer, even though a relatively high barrier exists between the TFB and the QDs. Meanwhile the high lowest unoccupied molecular orbital (LUMO) level of TFB and low valence band level of TiO_2 can effectively block injected electrons and holes and confine them

[1]Frontier Research Lab, Samsung Advanced Institute of Technology, Samsung Electronics, Gyeonggi-Do 446-712, South Korea, [2]Materials Research Lab, Samsung Advanced Institute of Technology, Samsung Electronics, Gyeonggi-Do 446-712, South Korea, [3]Display Lab, Samsung Advanced Institute of Technology, Samsung Electronics, Gyeonggi-Do 446-712, South Korea. *e-mail: choibl@samsung.com

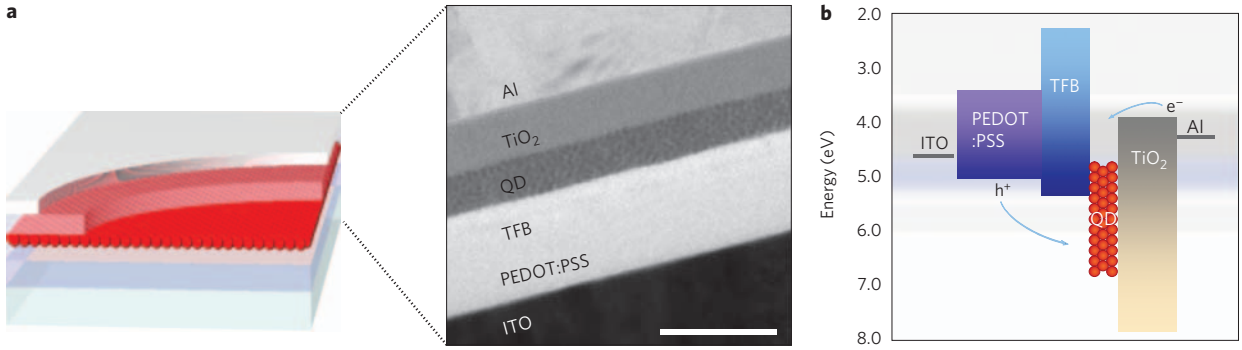

Figure 1 | Structure and energy levels of the QD-LED. a, Device structure (left) and cross-sectional TEM image (right) of the QD-LED. TFB, poly[(9,9-dioctylfluorenyl-2,7-diyl)-co-(4,4′-(*N*-(4-sec-butylphenyl))diphenylamine)]. Scale bar, 100 nm. **b**, Schematic structure with associated energy band diagram. The TFB energy level was estimated from ref. 13. The QD and TiO_2 energy bands were determined from UPS and optical absorption measurements (see Supplementary Figs S1,S2).

within the QD layer, enhancing the probability of carrier recombination. The sol–gel TiO_2 layer was deposited by spin-coating, enabling our QD-LED to be fabricated by means of an all-solution process with the exception of the aluminium electrode layer. Because the TiO_2 layer was annealed at low temperature (<150 °C), it is neither in a crystalline phase nor fully inorganic. Nevertheless, this layer has good semiconducting behavior, with a bandgap of 3.9 eV. Such behaviour has been documented previously in polymer solar cells, the sol–gel TiO_2 layer showing a relatively high carrier mobility of 1.7×10^{-4} cm^2 V^{-1} s^{-1} (ref. 15). Although its characteristics are not well understood, the TiO_2 layer, fabricated in a low-temperature sol–gel process, is useful for various electronic devices, especially plastic ones. As a result of the low-temperature process used for TiO_2 deposition, the QD-LED can also be realized without any degradation of the organic layers.

Carrier transport in the QD-LED. Figure 2 shows a comparison of the electrical properties of the QD-LED with a TiO_2 ETL and those of a reference device without a QD layer and with a QD-LED with an Alq_3 ETL. In the reference device, the slope of the current density–voltage (J–V) curve showed trap-limited behaviour ($J \propto V^n$, $n > 2$) over a relatively small voltage range, which changed to space-charge limited conduction ($J \propto V^2$) as the operating voltage was increased. The TiO_2-based QD-LED, however, demonstrated trap-limited conduction that lasted long beyond the turn-on voltage with much lower current density, suggesting that the QDs act as trap sites[16]. Compared to the organic-based QD-LED using Alq_3 as the ETL, the TiO_2-based QD-LED gives two orders of magnitude larger current density over the entire voltage range, and shows a similar tendency for the long-lasting trap-limited conduction region in the J–V characteristics. From the enlarged current density, we concluded that electron injection into and transport through TiO_2 is superior to that for Alq_3 in our device structure; this becomes self-evident when considering the lower band offset (0.4 eV) for Al/TiO_2 compared to that for Al/Alq_3 (1.2 eV) and the higher electron mobility (1.7×10^{-4} cm^2 V^{-1} s^{-1}) of the sol–gel TiO_2 compared to that for Alq_3 ($\sim 1.0 \times 10^{-5}$ cm^2 V^{-1} s^{-1}) (refs 15,17). For the same reason, the turn-on voltage in the TiO_2-based QD-LED also significantly decreased to 1.9 V, which is smaller than the QD bandgap of 2.1 eV and much lower than that observed for the Alq_3-based device (~4.0 V). The onset of EL occurs after the minority carriers have been injected into the emitting layer. To determine which carriers are dominant in the QD-LED, we adjusted the hole conductivity of the HIL by blending PEDOT polymers with differing amounts of PSS. In Fig. 3a, it can be observed that as the HIL conductivity increases from 3.6×10^{-4} S cm^{-1} to 7.1×10^{-2} S cm^{-1}, the maximum luminance and luminous

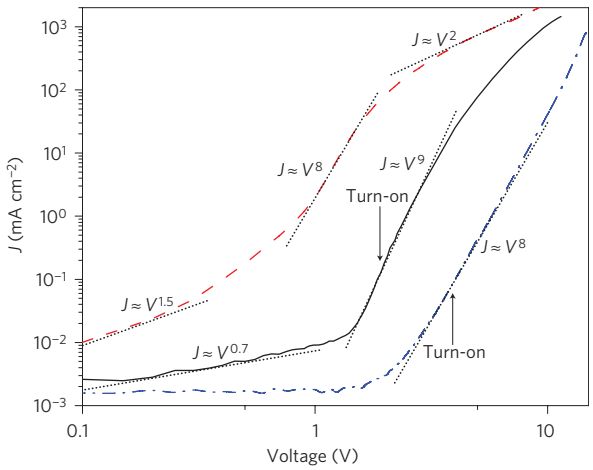

Figure 2 | Current density versus voltage characteristics of the QD-LED. J–V characteristics of a TiO_2-based QD-LED as shown in Fig. 1 (black solid line), a QD-LED with Alq_3 as the ETL (blue broken line), and a reference, TiO_2-based QD-LED without the QD layer (red broken line). Three different conduction regimes are apparent in the reference device (ohmic, trap-limited, and space-charge-limited conduction), whereas the other devices show partial (for the TiO_2-based QD-LED) or no change (for the Alq_3-based QD-LED) from trap- to space-charge-limited conduction due to large trap densities. The device turn-on voltage of the Alq_3-based QD-LED is larger (4.0 V) than the TiO_2-based QD-LED (1.9 V).

efficiency gradually increases and the J–V characteristics remain approximately the same (Fig. 3b). This indicates that our QD-LED is an electron-dominant device and that increasing the hole concentration within the QD layer improves charge balance. At a PEDOT:PSS conductivity of 7.1×10^{-2} S cm^{-1} (sample C), the QD-LED shows maximum luminance and luminous efficiency values of 12,380 cd m^{-2} and 1.67 cd A^{-1}, respectively. Beyond 7.1×10^{-2} S cm^{-1}, further increases in the PEDOT:PSS conductivity did not result in increased luminance and luminous efficiency. The hole concentration is believed to be limited by the hole transport properties of TFB at such high HIL conductivities. All QD-LED devices in this study, unless otherwise mentioned, used unmixed HIL (Baytron AI4083) for convenience of fabrication (conductivity typically $\sim 1 \times 10^{-3}$ S cm^{-1}).

Crosslinking of the QD layer. In QD-LEDs, the energy band position of the QD is located ~1 eV below that for typical organic light-emitting materials. This produces a relatively large band offset between the HTL

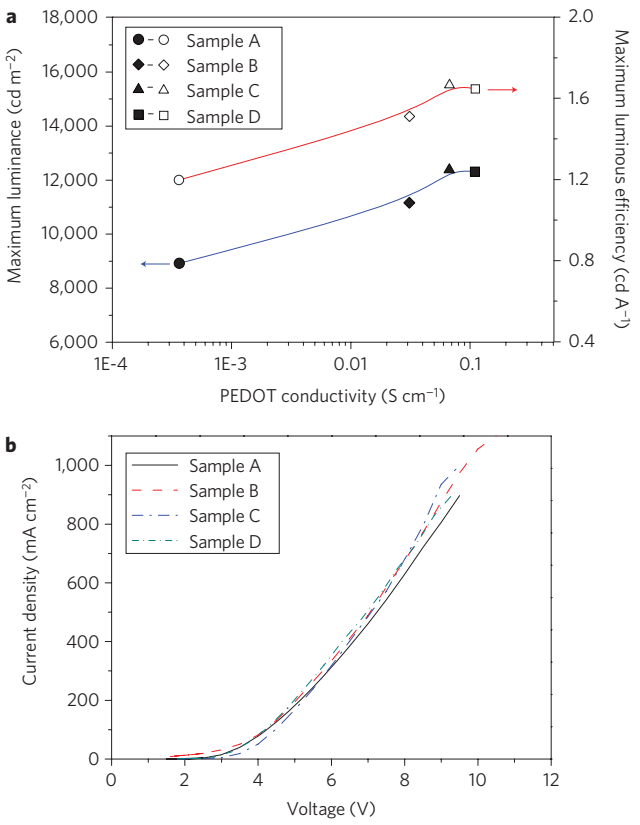

Figure 3 | Performance and *J–V* characteristics for QD-LEDs with different PEDOT:PSS conductivities. a, Maximum luminance and luminous efficiencies of QD-LEDs as a function of PEDOT:PSS conductivity. **b**, *J–V* characteristics for QD-LEDs with different PEDOT:PSS conductivities. The luminance and luminous efficiency gradually increased with PEDOT:PSS conductivity up to 0.07 S cm^{-1}, whereas the *J–V* characteristics were approximately the same; this suggests that the majority carrier of the device is the electron. Beyond 0.07 S cm^{-1}, the luminance and luminous efficiencies no longer increase due to hole concentration restrictions caused by TFB. Sample C showed the highest luminance (12,380 cd m^{-2}).

and the QD layer, which necessitates high operating voltages and leads to low power efficiencies. As shown in Fig. 1b, a relatively high barrier between the TFB and the QD layer also exists in our QD-LED. To reduce the band offset between the HTL and QD layer, we have attempted to shift the valence band of the QD layer upwards using a crosslinking method. During crosslinking, linker molecules become attached to the QD through exchange with pre-existing surfactants or by binding to empty sites on the QD surface. According to Soreni-Harari and colleagues, adsorption of organic molecules can cause energy levels to realign through the formation of microscopic surface dipoles at the QD–surfactant interface[18]. Specifically, the change in energy level is primarily determined by the binding functionality between the anchor group of the crosslinker and the QD surface. A larger energy shift has been experimentally observed for anchor groups with higher electronegativities[18]. For this reason, the amine group is a good candidate as the anchor of the crosslinker and in our experiment the QD layer was crosslinked with 1,7-diaminoheptane followed by thermal annealing. The effects of the crosslinker on the valence band of the QD layer were studied using UPS analysis. We prepared five QD films on silicon substrates with different manipulations: an as-coated QD film without any post-treatment (f1), a QD film that was crosslinked (f2), a crosslinked film annealed at 80 or 180 °C for 30 min (f3 and f4, respectively), and a QD film annealed at 180 °C for 30 min without crosslink (f5). The UPS results for these QD films are presented in detail in Table 1. The ionization potential (valence band level) of the as-coated QD film (f1) was 6.85 V below the vacuum level, which correlates well with other reported values[20] (see Supplementary Fig. S2). A remarkable shift of ~0.6 eV in the QD valence band level towards the vacuum level was observed for crosslinked films (f2–f4). This energy shift is significantly larger than a previously reported result for InAs QDs (0.3 eV) (ref. 18). The magnitude of our shift is reasonable considering the differences in the QD materials and the adsorption conditions of the anchors on the QD surfaces. Because crosslinking was carried out on a QD film for our case, the crosslinkers are expected to be asymmetrically adsorbed onto the QD surfaces; for a QD solution, the cross-linkers would be expected to be distributed more uniformly. We observed that the maximum peak in the EL spectra was not influenced by the crosslinking process (see Supplementary Fig. S3), suggesting that the conduction band of the QD layer shifts upwards simultaneously with the valence band. Whether QD films are crosslinked or not, subsequent thermal annealing has little effect on the energy band levels (f2–f5).

Figure 4 shows the EL characteristics of QD-LEDs fabricated with different crosslinking and thermal annealing conditions. An as-coated QD layer without further treatment was not examined because it was partially damaged during spin-coating of the sol–gel TiO_2 upper layer. From the data, it is apparent that crosslinking the QD layer greatly improves the luminance and luminous efficiency of samples 1–3 (Fig. 4b and c). In sample 1, the QD-LED device was prepared by only crosslinking the QD layer after spin-coating without thermal annealing. In samples 2 and 3, QD films were crosslinked and annealed at 80 °C (sample 2) or 180 °C (sample 3), respectively, for 30 min under nitrogen. In sample 4, the QD layer was annealed at 180 °C for 30 min without crosslinking. According to the UPS results, the energy band offset between the QDs and the HTL was reduced from 1.5 to 0.9 eV for our devices and consequently leads to an increase by over a factor of 10 in the maximum luminous efficiency (samples 3 and 4) because of more efficient hole injection and enhanced charge balance. Even though the thermal treatment did not change the energy band levels of the QD layer (Table 1), it considerably improved the luminance and luminous efficiencies (samples 1–3). Therefore, thermal annealing temperature is an additional key parameter influencing device performance. In Fig. 4a, the current density was mainly governed by the annealing temperature and not the crosslinking. This is explained by the fact that 20% of organic surfactants and crosslinkers within the QD layer are removed during thermal annealing at 180 °C for 30 min according to TGA analysis (see Supplementary Fig. S4). By removing a portion of the electrically insulating organic residues surrounding the QDs, the contact resistance at the QD–HTL and QD–ETL interfaces is effectively decreased. In addition, thermal annealing provides tight contact between the QDs and HTL, which improves hole injection and charge balance. The temperature dependence of the maximum luminance and current density was investigated in detail for the crosslinked QD-LED (Fig. 4d). The current density and maximum luminance gradually increased with temperature up to 210 °C, as expected. Beyond 210 °C, the maximum luminance for the QD-LEDs decreases in spite of increased current density. This trend is caused by degradation of the QDs, which is corroborated by the rapid decrease in PL intensity for QD films annealed beyond 210 °C.

A distinctive feature of our crosslinked QD-LEDs is the significantly low turn-on voltage, which improves power efficiency. At a video brightness of 500 cd m^{-2}, the operating voltage of the device is 3.8 V, which is much lower than that for QD-LEDs with organic ETLs (~10.5 V) (ref. 11). Because of the low operating voltage, the maximum power efficiency is as high as 2.41 lm W^{-1} at 100 cd m^{-2} and 1.85 lm W^{-1} at 1,000 cd m^{-2}. In addition, the luminous efficiency has a maximum value of 2.53 cd A^{-1} at 4 V and remains greater than 2 cd A^{-1} over a wide luminance range of 30–4,000 cd m^{-2}, as shown in Fig. 5. The lifetime of the QD-LED is

Table 1 | Ionization potential results for QD films from He II ultraviolet photoelectron spectroscopy.

QD film	Secondary cutoff, $E_{s,cutoff}$ (eV)	Valence band edge, $E_{v,edge}$ (eV)	Ionization potential* (eV)	Corresponding devices in Fig. 4
As-coated (f1)	36.59	2.63	6.85	—
Crosslinked (f2)	35.77	1.21	6.25	Sample 1
Crosslinked/annealed at 80 °C (f3)	35.90	1.33	6.23	Sample 2
Crosslinked/annealed at 180 °C (f4)	35.55	0.96	6.23	Sample 3
Annealed at 180 °C (f5)	36.67	2.70	6.84	Sample 4

*Ionization potential = 40.81 eV – ($E_{s,cutoff}$ – $E_{v,edge}$).

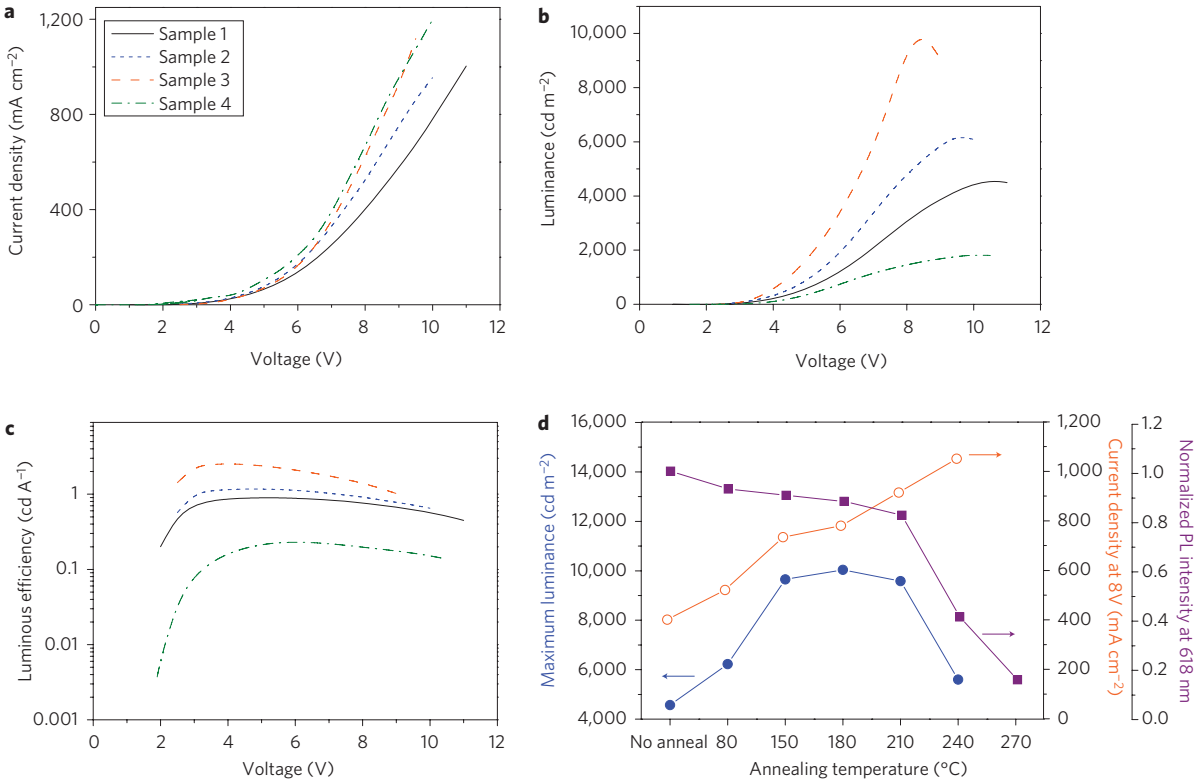

Figure 4 | Electroluminescence performance of QD-LEDs. a–c, Current density–voltage, luminance–voltage and luminous efficiency–voltage characteristics for the QD-LEDs with different QD manipulations: the QD layer crosslinked after spin-coating (sample 1), crosslinked and annealed at 80 or 180 °C, respectively, for 30 min under nitrogen (samples 2 and 3), and annealed at 180 °C for 30 min without crosslinking (sample 4). **d**, Maximum luminance and current density at fixed bias (8 V) for the QD-LEDs and the PL intensity for QD films as a function of annealing temperature after crosslinking the QD layer.

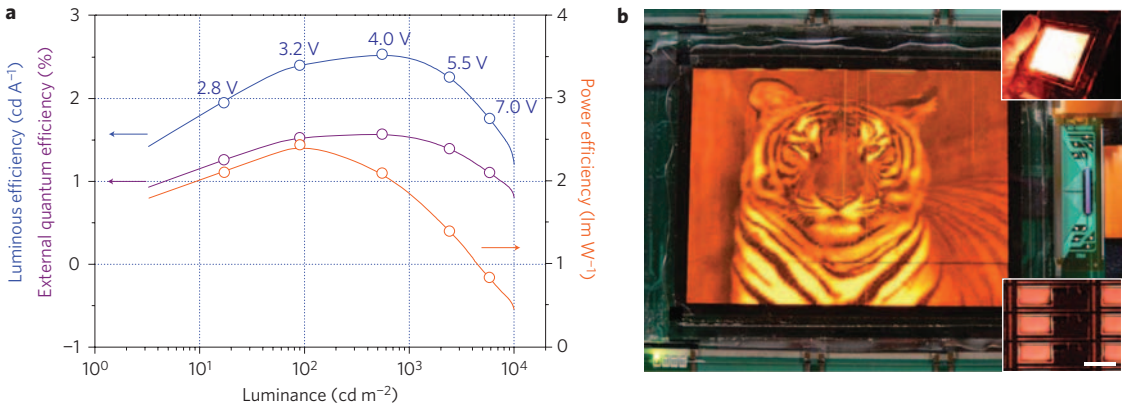

Figure 5 | Efficiency and electroluminescence image of QD-LEDs. a, Luminous efficiency, external quantum efficiency and power efficiency as a function of luminance. **b**, Display image of a 4-inch crosslinked QD-LED using an a-Si TFT backplane with a 320 × 240 pixel array for the active matrix drive. The upper right inset is an image of light emission from all pixels under operation at 500 cd m^{-2} and the lower right inset shows each pixel. Scale bar, 100 μm.

50.5 h at the initial luminance of 1,000 cd m^{-2} (see Supplementary Fig. S5). We have also constructed a display device using the cross-linked QD-LED using an a-Si thin-film transistor (TFT) backplane as an active matrix drive (Fig. 5b). The device has uniform brightness with less than 5% variation over a 4-inch display area.

In conclusion, this work demonstrates that a high-performance colloidal QD-LED can be achieved using specific crosslinking and thermal annealing of the QD layer and the use of a sol–gel processed TiO_2 electron transport layer. Controlling the energy levels of the QD layer through surface manipulation provides a useful way to solve the problem of large potential barriers between the valence level of commonly used colloidal QDs and the ITO work function; this provides more flexibility when developing the device structure and materials. These results bring us one step closer to developing colloidal QD-LEDs suitable for application in high-performance, easy-to-fabricate, large-area commercial devices such as flat panel displays and illumination sources.

Methods

QD-LED fabrication and characterization. A patterned ITO glass was first cleaned using various solvents and then UV-ozone treated. A HIL, PEDOT:PSS (Baytron P VP AI4083) was spin-coated onto the patterned ITO glass, and the film then baked at 200 °C for 5 min in a nitrogen glove box after baking at 110 °C for 5 min in air. TFB (H.W. Sands Corp.) as HTL was spin-coated, using m-xylene as the solvent, on top of the PEDOT:PSS layer and then annealed at 180 °C for 30 min in a nitrogen glove box. QDs in cyclohexane solution (10 mg ml^{-1}) were spin-coated on top of the TFB layer at 2,000 rpm for 30 s. QD spin-coating and crosslinking were performed under ambient conditions. For QD crosslinking, a 20 mM methanol solution of 1,7-diaminoheptane was heated to 60 °C. QD films were then dipped into the crosslinking solution for 15 min and subsequently soaked in pure methanol for 5 min. After rinsing with isopropanol and drying with a nitrogen stream, the films were annealed at 180 °C for 30 min in a nitrogen glove box. A TiO_2 sol–gel precursor (DuPont tyzol BTP) was diluted to 5 wt% in butanol for spin-coating the ETL. Spin-coating was performed at 2,000 rpm for 30 s and then subsequently annealed at 100 °C for 30 min under ambient conditions. We deposited aluminium on top of the ETL using a thermal evaporator. Finally, devices were shielded with encapsulation glass in a nitrogen glove box.

EL spectra, current density–voltage (J–V), and luminance–voltage (L–V) characteristics were recorded using a Topcon SR3 spectroradiometer coupled with an Advantac R6243DC voltage and current source. All measurements were performed under ambient conditions. The lifetimes of the QD-LEDs were tested at room temperature using a McScience Polaronix Lifetime Test System.

Received 5 November 2008; accepted 21 April 2009; published online 24 May 2009

References

1. Colvin, V. L., Schlamp, M. C. & Alivisatos, A. P. Light-emitting diodes made from cadmium selenide nanocrystals and a semiconducting polymer. *Nature* **370,** 354–357 (1994).
2. Dabbousi, B. O., Bawendi, M. G., Onitsuka, O. & Rubner, M. F. Electroluminescence from CdSe quantum-dot/polymer composites. *Appl. Phys. Lett.* **66,** 1316–1318 (1995).
3. Schlamp, M. C., Peng, X. & Alivisatos, A. P. Improved efficiencies in light emitting diodes made with CdSe(CdS) core/shell type nanocrystals and a semiconducting polymer. *J. Appl. Phys.* **82,** 5837–5842 (1997).
4. Mattoussi, H. *et al.* Electroluminescence from heterostructures of poly(phenylene vinylene) and inorganic CdSe nanocrystals. *J. Appl. Phys.* **83,** 7965–7974 (1998).
5. Coe, S., Woo, W.-K., Bawendi, M. & Bulović, V. Electroluminescence from single monolayers of nanocrystals in molecular organic devices. *Nature* **420,** 800–803 (2002).
6. Tessler, N., Medvedev, V., Kazes, M., Kan, S. & Banin, U. Efficient near-infrared polymer nanocrystal light-emitting diodes. *Science* **295,** 1506–1508 (2002).
7. Chaudhary, S., Ozkan, M. & Chan, W. C. W. Trilayer hybrid polymer–quantum dot light-emitting diodes. *Appl. Phys. Lett.* **84,** 2925–2927 (2004).
8. Coe-Sullivan, S., Steckel, J. S., Woo, W.-K., Bawendi, M. G. & Bulović, V. Large-area ordered quantum-dot monolayers via phase separation during spin-casting. *Adv. Funct. Mater.* **15,** 1117–1124 (2005).
9. Caruge, J.-M., Halpert, J. E., Bulović, V. & Bawendi, M. G. NiO as an inorganic hole-transporting layer in quantum dot light-emitting devices. *Nano Lett.* **6,** 2991–2994 (2003).
10. Mueller, A. H. *et al.* Multicolor light-emitting diodes based on semiconductor nanocrystals encapsulated in GaN charge injection layers. *Nano Lett.* **5,** 1039–1044 (2005).
11. Sun, Q. *et al.* Bright, multicolored light-emitting diodes based on quantum dots. *Nature Photon.* **1,** 717–722 (2007).
12. Caruge, J. M., Halpert, J. E., Wood, V., Bulović, V. & Bawendi, M. G. Colloidal quantum-dot light-emitting diodes with metal-oxide charge transport layers. *Nature Photon.* **2,** 247–250 (2008).
13. Redecker, M., Bradley, D. D. C., Inbasekaran, M., Wu, W. W. & Woo, E. P. High mobility hole transport fluorene-triarylamine copolymers. *Adv. Mater.* **11,** 241–246 (1999).
14. Lim, J. *et al.* Preparation of highly luminescent nanocrystals and their application to light-emitting diodes. *Adv. Mater.* **19,** 1927–1932 (2007).
15. Kim, J. Y. *et al.* New architecture for high efficiency polymer photovoltaic cells using solution-based titanium oxide as an optical spacer. *Adv. Mater.* **18,** 572–576 (2006).
16. Hikmet, R. A. M., Talapin, D. V. & Weller, H. Study of conduction mechanism and electroluminescence in CdSe/ZnS quantum dot composites. *J. Appl. Phys.* **93,** 3509–3514 (2003).
17. Kepler, R. G. *et al.* Electron and hole mobility in tris(8-hydroxyquinolinolato-N1,O8) aluminum. *Appl. Phys. Lett.* **66,** 3618–3620 (1995).
18. Soreni-Harari, M. *et al.* Tunning energy level in nanocrystal quantum dots through surface manipulations. *Nano Lett.* **8,** 678–684 (2008).
19. Coe-Sullivan S., Woo, W.-K., Steckel, J. S., Bawendi, M. & Bulović, V. Tuning the performance of hybrid organic/inorganic quantum dot light-emitting devices. *Org. Electron.* **4,** 123–130 (2003).

Acknowledgements

The authors thank J. Lee, J. M. Lee, J. Chung and I. Song for helpful discussion, S. Jun and H. Jang for providing quantum dots and J. W. Kim, Y. T. Chun, J.-Y. Kwon and Y. G. Lee for fabricating the QD–LED device with the a-Si TFT backplane.

Author contributions

K.-S.C., E.K.L., W.-J.J. and B.L.C. carried out the experiment and contributed to the writing of the paper. E.J. synthesized the quantum dots. T.-H.K., S.J.L., S.-J.K., J.Y.H. and B.-K.K. assisted with the experiment and the device analysis. J.M.K. contributed to the writing of the paper and the project planning.

Additional information

Supplementary information accompanies this paper at www.nature.com/naturephotonics. Reprints and permission information is available online at http://npg.nature.com/reprintsandpermissions/. Correspondence and requests for materials should be addressed to B.L.C.

nature photonics

ARTICLES

PUBLISHED ONLINE: 24 MAY 2009 | DOI: 10.1038/NPHOTON.2009.93

Manipulation of multiphoton entanglement in waveguide quantum circuits

Jonathan C. F. Matthews‡, Alberto Politi‡, André Stefanov† and Jeremy L. O'Brien*

On-chip integrated photonic circuits are crucial to further progress towards quantum technologies and in the science of quantum optics. Here we report precise control of single photon states and multiphoton entanglement directly on-chip. We manipulate the state of path-encoded qubits using integrated optical phase control based on resistive elements, observing an interference contrast of 98.2 ± 0.3%. We demonstrate integrated quantum metrology by observing interference fringes with two- and four-photon entangled states generated in a waveguide circuit, with respective interference contrasts of 97.2 ± 0.4% and 92 ± 4%, sufficient to beat the standard quantum limit. Finally, we demonstrate a reconfigurable circuit that continuously and accurately tunes the degree of quantum interference, yielding a maximum visibility of 98.2 ± 0.9%. These results open up adaptive and fully reconfigurable photonic quantum circuits not just for single photons, but for all quantum states of light.

Controlling quantum systems is not only a fundamental scientific endeavour, but also holds promise for profound new technologies[1–3]. Quantum photonics already provides enhanced communication security[3–7]; it has demonstrated increased precision by beating the standard quantum limit in metrology[8–11] and the diffraction limit in lithography[12,13], it holds great promise for quantum computation[14,15], and it continues to advance fundamental quantum science. The recent demonstrations of integrated quantum circuits[16–18] are key steps towards these new technologies and for further progress in fundamental science applications.

Technologies based on harnessing quantum-mechanical phenomena require methods to precisely prepare and control the state of quantum systems. Manipulation of a path-encoded qubit—a single photon in an arbitrary superposition of two optical paths, which is the natural encoding for waveguides[16,17]—requires control of the relative phase ϕ between the two optical paths and the amplitude in each path.

The integrated waveguide device shown schematically in Fig. 1a applies the unitary operation $U_{MZ} = U_{DC}e^{i\phi\sigma_Z/2}U_{DC}$: each 50% splitting ratio (reflectivity $\eta = 0.5$) directional coupler implements $U_{DC} = ie^{-i\pi\sigma_Z/4}He^{-i\pi\sigma_Z/4}$, which transforms the logical qubit states according to $U_{DC}|0\rangle = \frac{1}{\sqrt{2}}(|0\rangle + i|1\rangle)$ and $U_{DC}|1\rangle = \frac{1}{\sqrt{2}}(i|0\rangle + |1\rangle)$, where the Hadamard gate $H = (\sigma_X + \sigma_Z)/\sqrt{2}$ and $\{\sigma_X, \sigma_Y, \sigma_Z\}$ are the single-qubit Pauli operators, while control over the relative optical phase ϕ between the two optical paths implements the phase gate $e^{i\phi\sigma_z/2}$. A single-photon input into mode a is transformed into a superposition across modes c and d:

$$|1\rangle_a|0\rangle_b \rightarrow \frac{1}{\sqrt{2}}(|1\rangle_c|0\rangle_d + i|0\rangle_c|1\rangle_d) \quad (1)$$

(a single-photon input into mode b is transformed into the same superposition but with a relative π phase shift). The relative optical phase is then controlled by the parameter ϕ, so that

$$\frac{1}{\sqrt{2}}(|1\rangle_c|0\rangle_d + i|0\rangle_c|1\rangle_d) \rightarrow \frac{1}{\sqrt{2}}(|1\rangle_c|0\rangle_d + ie^{i\phi}|0\rangle_c|1\rangle_d) \quad (2)$$

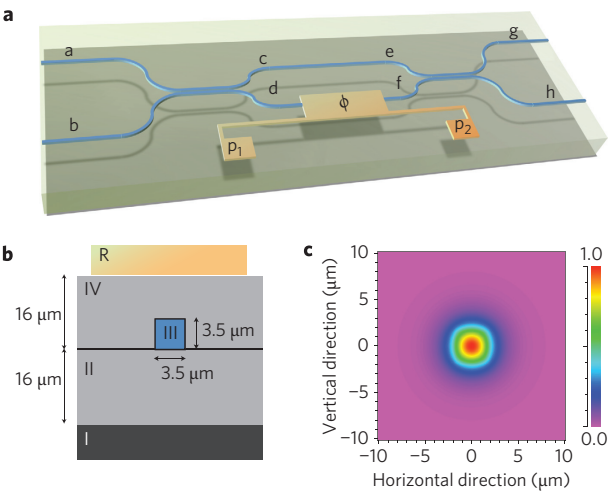

Figure 1 | Manipulating quantum states of light on a chip. a, Schematic of a waveguide circuit with the relative optical phase ϕ controlled by applying a voltage V across the contact pads p_1 and p_2 (not to scale). **b**, Illustration of the cross-section of one waveguide located beneath a resistive heater. **c**, The simulated intensity profile of the guided single mode in the silica waveguides at a wavelength of 780 nm.

before the two modes are recombined at the second $\eta = 0.5$ coupler. This is of course a quantum mechanical description of a Mach–Zehnder (MZ) interferometer operating at the single photon level—something that is well understood in terms of bright coherent light. The device shown in Fig. 1a can also be used to manipulate the phase of multiphoton, entangled states of light.

Two additional relative phase controllers before and after this device would enable arbitrary one-qubit unitary operations[19], including state preparation and measurement. First note the relations $\sigma_X e^{i\phi\sigma_Z/2} = e^{-i\phi\sigma_Z/2}\sigma_X$ and $U_{MZ} = ie^{i\phi\sigma_Y/2}\sigma_X$. For some real ϕ_1, ϕ_2, ϕ_3, arbitrary qubit operations can be decomposed as $U_{arb} = e^{i\phi_3\sigma_Z/2}e^{i\phi_2\sigma_Y/2}e^{i\phi_1\sigma_Z/2}$; arbitrary qubit preparation from the logical basis is applied by $U_{prep} = e^{i\phi_3\sigma_Z/2}e^{i\phi_2\sigma_Y/2}$.

Centre for Quantum Photonics, H. H. Wills Physics Laboratory & Department of Electrical and Electronic Engineering, University of Bristol, Merchant Venturers Building, Woodland Road, Bristol, BS8 1UB, UK; †Present address: Federal Office of Metrology METAS, Lindenweg 50, CH-3003, Bern-Wabern, Switzerland; ‡These authors contributed equally to this work. *e-mail: Jeremy.OBrien@bristol.ac.uk

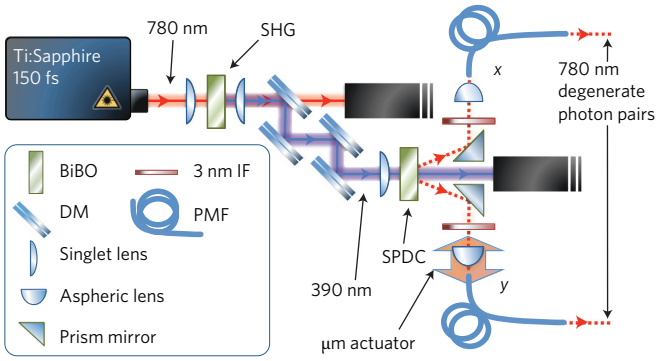

Figure 2 | Multiphoton state preparation. Pulsed, coherent 390 nm light pumps a Type-I nonlinear bismuth borate BiB_3O_6 (BiBO) crystal for spontaneous parametric down-conversion. Depending on the average pump power, we produce two- and four-photon states of 780 nm degenerate photons in two paths. (See Methods for further details.) SHG, second harmonic generation; IF, interference filter; DM, dichroic mirror; PMF, polarization maintaining fibre; SPDC, spontaneous parametric down-conversion.

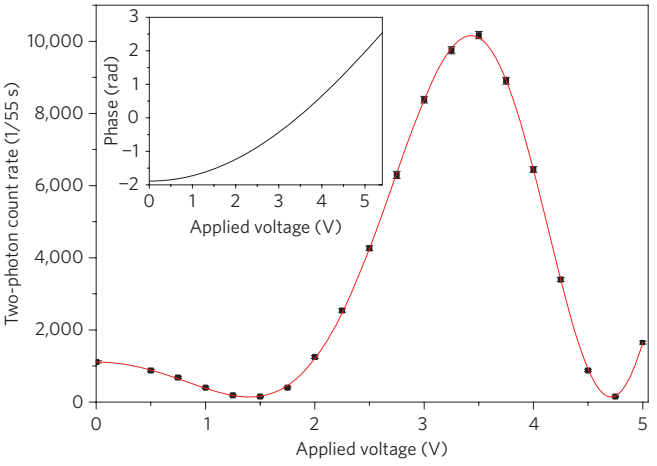

Figure 3 | Calibration of voltage-controlled phase shift. The two-photon interference pattern generated from simultaneous detection of a single photon at both outputs *g* and *h* as the voltage applied across the device was varied between 0 and 5 V. Error bars are given by Poissonian statistics. Inset: plot of the phase–voltage relationship determined from this calibration.

The inverse (or time-reversed) operation $U^{\dagger}_{\mathrm{prep}}$ provides arbitrary projective measurement[1]. By combining several such devices across N waveguides, it is possible to realize any arbitrary N-mode unitary operator[19].

We begin by demonstrating a device that implements U_{MZ}, in which the phase shift ϕ is controlled by the voltage applied to a lithographically defined resistive heater. We then use this device to manipulate one-, two- and four-photon entangled states relevant to quantum metrology. Finally, we demonstrate how such a device can be used to realize a reconfigurable photonic quantum circuit.

Results

Voltage-controlled phase shift. Waveguide devices, as illustrated in the cross-section in Fig. 1b, were fabricated on a 4-inch silicon wafer (material I), onto which a 16-μm layer of thermally grown undoped silica was deposited as a buffer to form the lower cladding of the waveguides (II). A 3.5-μm layer of silica doped with germanium and boron oxides was then deposited by flame hydrolysis; the material of this layer constitutes the core of the stucture and was patterned into 3.5-μm-wide waveguides using standard optical lithographic techniques (III). The 16-μm upper cladding (IV) was composed of phosphorus and boron-doped silica with a refractive index matched to that of the buffer. Simulations indicated single-mode operation at 780 nm, as shown in Fig. 1c. A final metal layer was lithographically patterned on top of the devices to form resistive elements (R) and the metal connections and contact pads (p_1 and p_2) shown in Fig. 1a.

When a voltage was applied between p_1 and p_2, the current in R generated heat, which dissipated into the device and locally raised the temperature T of the core and cladding material of the waveguide section directly below. To a first approximation, the change in refractive index n of silica is given[20] by $\mathrm{d}n/\mathrm{d}T = 1 \times 10^{-5}/\mathrm{K}$ (independent of compositional variation), which in turn alters the mode group index of the light confined in the waveguide beneath R. The devices were designed to enable a continuously variable phase shift $\phi \in [-\pi/2, \pi/2]$ and operate at room temperature. A consequence of the miniature and monolithic structure of the chip is that no strict global temperature control of the device is required for stability (see Supplementary Information).

The voltage-controlled phase inside the waveguide circuit, shown schematically in Fig. 1a, was determined by a nonlinear relation $\phi(V)$, which we calibrated using a two-photon interference effect (see Supplementary Information): ideally, the maximally path entangled state of two photons

$$\frac{1}{\sqrt{2}}(|2\rangle_c|0\rangle_d + |0\rangle_c|2\rangle_d) \tag{3}$$

is generated inside the device[21–27] on inputting the state $|1\rangle_a|1\rangle_b$, which we produced using the setup shown in Fig. 2. After the phase shift this entangled state is transformed to $\frac{1}{\sqrt{2}}(|2\rangle_e|0\rangle_f + e^{i2\phi}|0\rangle_e|2\rangle_f)$. Figure 3 shows the results of this calibration, in which the rate of simultaneous detection of two photons at outputs g and h is plotted as a function of the applied voltage V across p_1 and p_2. The phase voltage relationship was verified to be a polynomial function of the form

$$\phi(V) = \alpha + \beta V^2 + \gamma V^3 + \delta V^4 \tag{4}$$

where the parameters were found by means of best-fit (see Supplementary Information); the resulting relationship is plotted in the inset of Fig. 3. In comparison to simply using one-photon 'classical' interference, this 'quantum calibration' harnesses the reduced de Broglie wavelength[4–6] of two-photon interference[21–27] to wider sample the pattern of phase-dependent interference, thereby giving greater precision in the $\phi(V)$ calibration. This approach is particularly useful because the range of ϕ we could implement was limited by the maximum voltage that can be applied across the electrodes. The phase shift was found to be stable on a timescale of several hours (see Supplementary Information).

Multiphoton entangled state manipulation. Having obtained $\phi(V)$, we were able to analyse the sinusoidal interference pattern arising from single-photon detections at outputs g and h when launching single photons into input a and controlling $\phi(V)$. Ideally, the probability of detecting photons varies as

$$P_g = 1 - P_h = \frac{1}{2}[1 - \cos(\phi)] \tag{5}$$

yielding sinusoidal interference fringes with a period of 2π. The observed fringes (Fig. 4a) show a high contrast $C = (N_{\max} - N_{\min})/(N_{\max} + N_{\min})$ of $C = 0.982 \pm 0.003$. From this contrast, and assuming no mixture or complex phase is introduced, it is possible to calculate the average fidelity F between the realized and ideal output state $U_{\mathrm{MZ}}|0\rangle = \cos(\phi/2)|0\rangle + i\sin(\phi/2)|1\rangle$. Averaging over the range $\phi \in [-\pi/2, \pi/2]$ we find $\bar{F} = 0.99984 \pm 0.00004$.

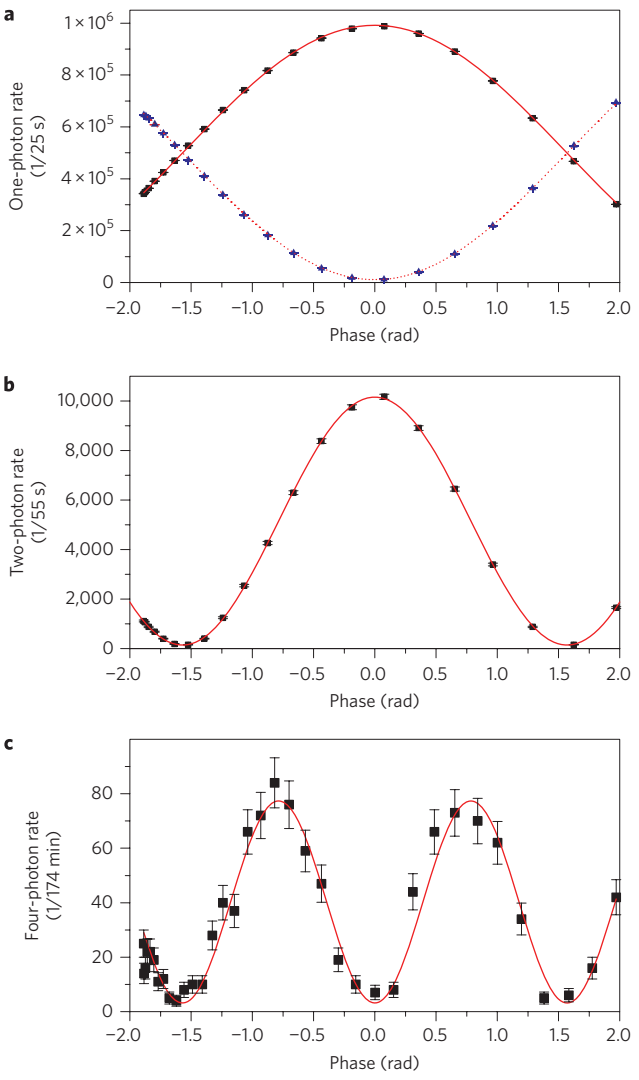

Figure 4 | Integrated quantum metrology. a, One-photon count rates at the outputs g (blue triangles, dotted fit) and h (black squares, solid fit) as the phase $\phi(V)$ is varied on inputting the one-photon state $|1\rangle_a|0\rangle_b$. **b**, Two-photon coincidental detection rate between the outputs g and h when inputting the two-photon state $|1\rangle_a|1\rangle_b$ and varying the phase $\phi(V)$. **c**, Four-photon coincidental detection rate of the output state $|3\rangle_g|1\rangle_h$ when inputting the four-photon state $|2\rangle_a|2\rangle_b$. Error bars are given by Poissonian statistics.

These devices also enable us to manipulate and analyse multiphoton entangled states. For example, the state (3) should ideally be transformed according to $\frac{1}{\sqrt{2}}(|2\rangle_e|0\rangle_f + e^{2i\phi}|0\rangle_e|2\rangle_f)$. To confirm the correct on-chip control of this entangled state, simultaneous detection of a single photon at each output g and h was recorded as a function of ϕ; this ideally yields a '$\lambda/2$' interference fringe described by

$$P_{g,h} = \frac{1}{2}(1 + \cos 2\phi) \tag{6}$$

with period π—half the period of the one-photon interference fringes. The two-photon interference fringe shown in Fig. 4b plots the measured simultaneous detection rate as a function of ϕ. The contrast is $C = 0.972 \pm 0.004$, which is greater than the threshold $C_{\text{th}} = 1/\sqrt{2}$ required to beat the standard quantum limit[28], as described below. Note that although a two-photon interference fringe was used to calibrate the phase shift, this calibration is not required to claim a $\lambda/2$ interference fringe; this is simply confirmed by comparison with the one-photon fringe, which can be done even without calibrating the phase.

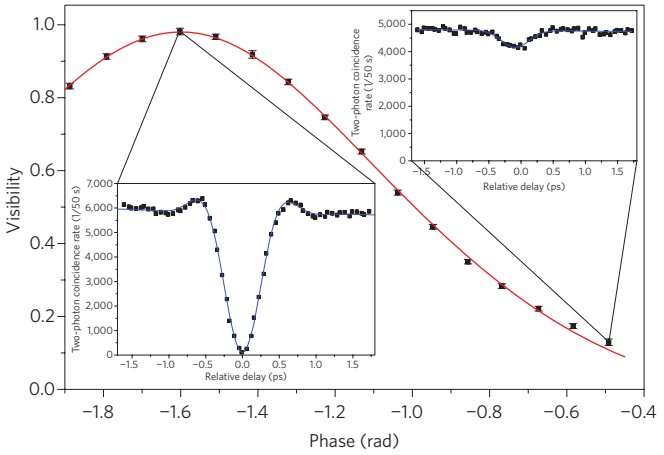

Figure 5 | A reconfigurable quantum circuit. Visibility of the Hong–Ou–Mandel experiment performed using the integrated MZ interferometer as a continuously variable beamsplitter with effective reflectivity $\eta = \sin^2(\phi/2)$. The solid line is a theoretical fit that includes a small phase offset and a small amount of mode mismatch as the only two free parameters that modify equations (10) and (11). Error bars are given by confidence intervals on the best-fit parameter. Left inset: High-visibility two-photon interference. Right inset: Low-visibility two-photon interference. Both inset plots are displayed as a plot of two-photon rate versus the relative optical delay between the interfering photons and fitted with a function that takes into account the non-Gaussian shape of the interference filter used in the experiment. Error bars for each inset are given by Poissonian statistics.

The interference fringe shown in Fig. 4b arises from the two-photon maximally path entangled state that is an equal superposition of N photons in one mode and N photons in another mode: $|N\rangle|0\rangle + |0\rangle|N\rangle$ (ref. 29). Such a state evolves under a ϕ phase shift in the second mode to $|N\rangle|0\rangle + e^{iN\phi}|0\rangle|N\rangle$ and can in principle be used to estimate an unknown phase ϕ with a sensitivity $\Delta\phi = 1/N$, better than the standard quantum limit $\Delta\phi = 1/\sqrt{N}$ (the limit attainable with classical schemes). By inputting the four-photon state $|2\rangle_a|2\rangle_b$, nonclassical interference at the first directional coupler ideally produces the state [6,28,30]

$$\sqrt{\frac{3}{4}}(|4\rangle_c|0\rangle_d + |0\rangle_c|4\rangle_d)/\sqrt{2} + \frac{1}{\sqrt{4}}|2\rangle_c|2\rangle_d \tag{7}$$

At the second directional coupler, quantum interference means that only the $|4\rangle|0\rangle + |0\rangle|4\rangle$ part of this state gives rise to $|3\rangle_g|1\rangle_h$ and $|1\rangle_g|3\rangle_h$ in the output state of the interferometer. By varying the phase ϕ in the interferometer, the probability of detecting either of the states $|3\rangle_g|1\rangle_h$ or $|1\rangle_g|3\rangle_h$ is given by

$$P_{3g,h} = P_{g,3h} = \frac{3}{8}(1 - \cos 4\phi) \tag{8}$$

and yields a '$\lambda/4$' interference fringe with period $\pi/2$. We measured the four-photon interference fringe shown in Fig. 4c, which plots the rate of simultaneous detection of four photons corresponding to the state $|3\rangle_g|1\rangle_h$ (by cascading three detectors using 1×2 fibre-beamsplitters at the output g) against the phase ϕ. The contrast of this four-photon interference is $C = 0.92 \pm 0.04$, which is greater than the threshold to beat the standard quantum limit[28].

Reconfigurable quantum circuits. Quantum interference of photons[31] at a directional coupler (or beamsplitter) lies at the

heart of the multiphoton interference fringes shown in Fig. 4 and is the crucial underlying physical process in linear optical networks for quantum-information science. The reflectivity η of a coupler determines the degree of quantum interference, thereby making η the critical parameter for quantum operation. The directional couplers in the device shown schematically in Fig. 1 were lithographically set to $\eta = 1/2$. More general photonic circuits, including optical entangling logic gates[14,16,32,33], are composed of a number of different reflectivity couplers, whereas adaptive schemes whose function depends on the input state, such as Fock state filters[34–36], make use of devices equivalent to a single coupler with variable η. Reconfigurable photonic circuits, including routing of photons, can be realized by combining such variable η devices. By controlling the phase ϕ within our devices, we implement the unitary operation

$$U_{\mathrm{MZ}} \doteq \begin{pmatrix} \sin(\phi/2) & \cos(\phi/2) \\ \cos(\phi/2) & -\sin(\phi/2) \end{pmatrix} \qquad (9)$$

acting on the two input waveguides[19]. This operation is equivalent to a single coupler with variable reflectivity

$$\eta = \sin^2 \frac{\phi}{2} \qquad (10)$$

We performed multiple quantum interference experiments[31] in which two photons were launched into inputs a and b of the device. While scanning through the relative arrival time with an off-chip optical delay, we measured the rate of simultaneous detection of a single photon at both outputs g and h. Each experiment resulted in a quantum interference 'dip' in this rate of simultaneous photon detection, centred around zero delay (see insets to Fig. 5). The depth of such a dip indicates the degree of quantum interference, which can be quantified by the visibility $V = (N_{\max} - N_{\min})/N_{\max}$. Ideally,

$$V_{\mathrm{ideal}} = \frac{2\eta(1-\eta)}{1-2\eta+2\eta^2} \qquad (11)$$

The main panel in Fig. 5 plots the quantum interference visibility observed for different values of ϕ and hence η. The insets of Fig. 5 show two examples of the raw data used to generate this curve: (right) $\phi = -0.49 \pm 0.01$ rad, $V = 0.129 \pm 0.009$; (left) $\phi = -1.602 \pm 0.01$ rad, $V = 0.982 \pm 0.009$. The average relative visibility $V_{\mathrm{rel}} = V/V_{\mathrm{ideal}}$ for all the data in Fig. 5 is $\overline{V_{\mathrm{rel}}} = 0.980 \pm 0.003$.

Discussion

Integrated optics has been developed primarily by the telecommunications industry for devices that allow high-speed information transmission, including optical switches, wavelength division multiplexers and modulators. Quantum optics appears destined to benefit from existing integrated optics technologies, as well as drive new developments for its own needs. The reconfigurable quantum circuit we demonstrate could be used as the fundamental element to build a large-scale circuit capable of implementing any unitary operation on many waveguides. A thermal-based 32×32 waveguide switch has been demonstrated[37]. Implementing an arbitrary unitary on this number of modes would require a comparable number of resistive elements. This is well beyond anything conceivable with bulk optics. The millisecond timescales available with thermal switching are suitable for reconfigurable circuits, for state preparation, quantum measurement, quantum metrology[2] and perhaps even full-scale quantum computing[38]. Other applications demanding fast switching, such as adaptive circuits for quantum control and feedforward, will require subnanosecond switching, which is possible using electro-optic materials such as $LiNbO_3$, used to make modulators operating at tens of gigahertz[39].

In addition to the demonstrations presented here, these devices may be used for other quantum states of light, for the fundamental sciences of quantum optics[40–42] and quantum information[43–46]. In particular, phase control will be particularly important for homodyne detection required for phase estimation[47] and adaptive measurements[48] with squeezed states of light. Our results point towards adaptive and arbitrarily reconfigurable quantum networks capable of generating, manipulating and characterizing multiphoton states of light with near-unit fidelity. Possible future applications span all of quantum information science from metrology to information processing.

Methods

Devices. The bend radius of curves in the directional couplers in the waveguide circuit are 15 mm at the tightest curvature, the effective interaction length of each directional coupler is 2.95 mm, and each path within the interferometer is 9.7 mm (defined from the end of the first directional coupler to the beginning of the second directional coupler). The maximum optical path difference with the maximum voltage we apply is $\sim\lambda/2$ (that is, ~390 nm). The physical length of the chip from input facet to output facet is 26 mm.

Multiphoton generation. The experiments reported were conducted using degenerate single-photon pairs at a wavelength of 780 nm produced by means of spontaneous parametric downconversion (SPDC). The nonlinear crystal used was a type-I phase-matched bismuth borate BiB_3O_6 (BiBO) pumped by a 390 nm 150 fs pulsed laser focused to a waist of $\omega_0 \approx 40$ μm. The 390 nm pump was prepared using a further BiBO crystal, phase-matched for second harmonic generation (SHG) to double the frequency of a 780 nm mode-locked Ti:sapphire laser focused to a waist of $\omega_0 \approx 40$ μm; four successive dichroic mirrors (DM) were used to purify the pump beam spectrally. Degenerate photon pairs were created by the SPDC crystal and passed through 3 nm interference filters (IF), which filtered each photon to a coherence length of $l_c = \lambda^2/\Delta\lambda \approx 200$ μm. The photons were collected into two single-mode polarization maintaining fibers (PMFs) coupled to two diametrically opposite points x and y on the SPDC cone. In the case of low average pump power, the state $|1\rangle_x|1\rangle_y$ was produced with a rate of 100 s^{-1}. On increasing the average pump power, the multiphoton production rate from the downconversion process was no longer negligible such that it is possible to produce two degenerate pairs of photons in the state $|2\rangle_x|2\rangle_y$.

Coupling to devices. The photons coupled into PMF were launched into the chip and collected at the outputs using two arrays of eight PMFs, with 250 μm spacing, to match that of the waveguides. The photons were detected using fiber coupled single photon counting modules (SPCMs). The PMF arrays and chip were directly buttcoupled, with index matching fluid, to obtain an overall coupling efficiency of ~60% through the device (input plus output insertion losses ~40%).

Received 15 January 2009; accepted 23 April 2009; published online 24 May 2009

References

1. Nielsen, M. A. & Chuang, I. L. *Quantum Computation and Quantum Information* (Cambridge Univ. Press, 2000).
2. Giovannetti, V., Lloyd, S. & Maccone, L. Quantum-enhanced measurements: beating the standard quantum limit. *Science* **306,** 1330–1336 (2004).
3. Gisin, N., Ribordy, G., Tittel, W. & Zbinden. Quantum cryptography. *Rev. Mod. Phys.* **74,** 145–195 (2002).
4. www.secoqc.net
5. www.idQuantique.com
6. www.magiqtech.com
7. www.smartquantum.com
8. Mitchell, M. W., Lundeen, J. S. & Steinberg, A. M. Super-resolving phase measurements with a multiphoton entangled state. *Nature* **429,** 161–164 (2004).
9. Walther, P. *et al.* de Broglie wavelength of a non-local four-photon state. *Nature* **429,** 158–161 (2004).
10. Nagata, T., Okamoto, R., O'Brien, J. L., Sasaki, K. & Takeuchi, S. Beating the standard quantum limit with four-entangled photons. *Science* **316,** 726–729 (2007).
11. Higgins, B. L., Berry, D. W., Bartlett, S. D., Wiseman, H. M. & Pryde, G. J. Entanglement-free Heisenberg-limited phase estimation. *Nature* **450,** 393–396 (2007).
12. Boto, A. N. *et al.* Quantum interferometric optical lithography: exploiting entanglement to beat the diffraction limit. *Phys. Rev. Lett.* **85,** 2733–2736 (2000).
13. Kawabe, Y., Fujiwara, H., Okamoto, R., Sasaki, K. & Takeuchi, S. Quantum interference fringes beating the diffraction limit. *Opt. Express* **15,** 14244–14250 (2007).
14. Knill, E., Laamme, R. & Milburn, G. J. A scheme for efficient quantum computation with linear optics. *Nature* **409,** 46–52 (2001).

15. O'Brien, J. L. Optical quantum computing. *Science* **318,** 1567–1570 (2007).
16. Politi, A., Cryan, M. J., Rarity, J. G., Yu, S. & O'Brien, J. L. Silica-on-silicon waveguide quantum circuits. *Science* **320,** 646–649 (2008).
17. Marshall, G. D. *et al.* Laser written waveguide photonic quantum circuits. <http://arxiv.org/abs/0902.4357> (2009).
18. Clark, A. S. *et al.* All-optical-fiber polarization-based quantum logic gate. *Phys. Rev. A* **79,** 030303 (2009).
19. Reck, M., Zeilinger, A., Bernstein, H. J. & Bertani, P. Experimental realization of any discrete unitary operator. *Phys. Rev. Lett.* **73,** 58–61 (1994).
20. Kenichi, I. & Yokubun, Y. *Encyclopedic Handbook of Integrated Optics* (CRC Press, 2006).
21. Ou, Z. Y., Zou, X. Y., Wang, L. J. & Mandel, L. Experiment on nonclassical fourth-order interference. *Phys. Rev. A* **42,** 2957–2965 (1990).
22. Rarity, J. G. *et al.* Two-photon interference in a Mach–Zehnder interferometer. *Phys. Rev. Lett.* **65,** 1348–1351 (1990).
23. Kuzmich, A. & Mandel, L. Sub-shot-noise interferometric measurements with two-photon states. *Quant. Semiclass. Opt.* **10,** 493–500 (1998).
24. Fonseca, E. J. S., Monken, C. H. & Pádua, S. Measurement of the de Broglie wavelength of a multiphoton wave packet. *Phys. Rev. Lett* **82,** 2868–2871 (1999).
25. Edamatsu, K., Shimizu, R. & Itoh, T. Measurement of the photonic de Broglie wavelength of entangled photon pairs generated by spontaneous parametric down-conversion. *Phys. Rev. Lett.* **89,** 213601 (2002).
26. Eisenberg, H. S., Hodelin, J. F., Khoury, G. & Bouwmeester, D. Multiphoton path entanglement by non-local bunching. *Phys. Rev. Lett.* **94,** 090502 (2005).
27. Resch, K. J. *et al.* Time-reversal and super-resolving phase measurements. *Phys. Rev. Lett.* **98,** 223601 (2007).
28. Okamoto, R. *et al.* Beating the standard quantum limit: phase super-sensitivity of *N*-photon interferometers. *New J. Phys.* **10,** 073033 (2008).
29. Lee, H., Kok, P. & Dowling, J. P. A quantum Rosetta stone for interferometry. *J. Mod. Opt.* **49,** 2325–2338 (2002).
30. Steuernagel, O. de Broglie wavelength reduction for a multiphoton wave packet. *Phys. Rev. A* **65,** 033820 (2002).
31. Hong, C. K., Ou, Z. Y. & Mandel, L. Measurement of subpicosecond time intervals between two photons by interference. *Phys. Rev. Lett.* **59,** 2044–2046 (1987).
32. O'Brien, J. L., Pryde, G. J., White, A. G., Ralph, T. C. & Branning, D. Demonstration of an all-optical quantum controlled-NOT gate. *Nature* **426,** 264–267 (2003).
33. Lanyon, B. P. *et al.* Simplifying quantum logic using higher-dimensional Hilbert spaces *Nat. Phys.*, **5,** 134–140 (2009).
34. Sanaka, K., Resch, K. J. & Zeilinger, A. Filtering out photonic Fock states. *Phys. Rev. Lett.* **96,** 083601 (2006).
35. Resch, K. J. *et al.* Entanglement generation by Fock-state filtration. *Phys. Rev. Lett.* **98,** 203602 (2007).
36. Okamoto, R. *et al.* An entanglement filter. *Science* **323,** 483–485 (2009).
37. Mino, S. Recent progress on PLC technologies for large-scale integration. *Optical Fiber Communication and Optoelectronics Conference, 2007 Asia*, 27 (2007).
38. Kieling, K., Ruddolph, T. & Eisert, J. Percolation, renormalization, and quantum computing with nondeterministic gates. *Phys. Rev. Lett.* **99,** 130501 (2007).
39. Wooten, E. L. *et al.* A review of lithium niobate modulators for fiber-optic communications systems. *IEEE J. Sel. Top. Quant. Electron.* **6,** 69–82 (2000).
40. Lobino, M. *et al.* Complete characterization of quantum-optical processes. *Science* **322,** 563–566 (2008).
41. Furusawa, A. *et al.* Unconditional quantum teleportation. *Science* ***282,*** 706–709 (1998)
42. Parigi, V., Zavatta, A., Kim, M. & Bellini, M. Probing quantum commutation rules by addition and subtraction of single photons to/from a light field. *Science* **317,** 1890–1893 (2007).
43. Braunstein, S. L. & van Loock, P. Quantum information with continuous variables. *Rev. Mod. Phys.* **77,** 513–577 (2005).
44. Ourjoumtsev, A., Tualle-Brouri, R., Laurat, J. & Grangier, P. Generating optical Schrodinger kittens for quantum information processing. *Science* **312,** 83–86 (2006).
45. Menicucci, N. C., Flammia, S. T. & Pfister, O. One-way quantum computing in the optical frequency comb. *Phys. Rev. Lett.* **101,** 130501 (2008).
46. O'Brien, J. L. Quantum computing over the rainbow. *Physics* **1,** 23 (2008).
47. Pezzé, L., Smerzi, A., Khoury, G., Hodelin, J. F. & Bouwmeester, D. Phase detection at the quantum limit with multiphoton Mach–Zehnder interferometry. *Phys. Rev. Lett.* **99,** 223602 (2007).
48. Berry, D. W. & Wiseman, H. M. Adaptive phase measurements for narrowband squeezed beams. *Phys. Rev. A.* **73,** 063824 (2006).

Acknowledgements

We thank A. Laing, T. Nagata, S. Takeuchi and X. Q. Zhou for helpful discussions. This work was supported by IARPA, EPSRC, QIP IRC and the Leverhulme Trust.

Additional information

Supplementary information accompanies this paper at www.nature.com/naturephotonics. Reprints and permission information is available online at http://npg.nature.com/reprintsandpermissions/. Correspondence and requests for materials should be addressed to J.L.O'B.

nature photonics

ARTICLES

PUBLISHED ONLINE: 24 MAY 2009 | DOI: 10.1038/NPHOTON.2009.94

Rapid and precise absolute distance measurements at long range

I. Coddington*, W. C. Swann, L. Nenadovic and N. R. Newbury*

The ability to determine absolute distance to an object is one of the most basic measurements of remote sensing. High-precision ranging has important applications in both large-scale manufacturing and in future tight formation-flying satellite missions, where rapid and precise measurements of absolute distance are critical for maintaining the relative pointing and position of the individual satellites. Using two coherent broadband fibre-laser frequency comb sources, we demonstrate a coherent laser ranging system that combines the advantages of time-of-flight and interferometric approaches to provide absolute distance measurements, simultaneously from multiple reflectors, and at low power. The pulse time-of-flight yields a precision of 3 μm with an ambiguity range of 1.5 m in 200 μs. Through the optical carrier phase, the precision is improved to better than 5 nm at 60 ms, and through the radio-frequency phase the ambiguity range is extended to 30 km, potentially providing 2 parts in 10^{13} ranging at long distances.

Multiple satellites flying in a precision formation can effectively act as a single distributed instrument and provide entirely new capabilities for space-based sciences. Formations would enable higher-resolution searches for extraterrestrial planets by providing a large synthetic aperture, enable direct imaging of a black hole by supporting an X-ray telescope distributed across satellites, or enable tests of general relativity through accurate measurements of satellite spacing in a gravitational field[1–11]. The formation acts as a single instrument only if the relative spacing and pointing of the satellites is tightly maintained, which is made possible by comparing distance measurements between multiple reference points on the satellites and feeding back to the satellite position and pointing.

In intrasatellite ranging, and similarly in manufacturing applications[12], there are three critical parameters: precision/accuracy, ambiguity range and update rate. High precision is particularly important in maintaining the pointing; for example, coherent combining of 1-m sub-apertures to form a synthetic aperture of 100-m diameter requires a relative pointing accuracy of less than (λ/100 m) rad for each sub-aperture, which in turn requires distance measurements at the sub-aperture edges with less than $\lambda \times$ (1 m/100 m) accuracy, or a few nanometres at optical wavelengths. The ambiguity range characterizes the measurement range window; longer distances are aliased back to within the ambiguity range. Larger ambiguity range requires less *a priori* distance knowledge. Finally, fast millisecond-scale update rates are needed for effective feedback. Many of these requirements push or exceed the capabilities of current 'stand off' ranging technology, but are achievable using an optical frequency comb, as shown here.

Generally speaking, laser ranging is the determination of the phase shift on a signal after traversing a given distance. Crudely, shorter-wavelength signals offer greater resolution, and longer-wavelength signals offer greater ambiguity range. For instance, the widely used continuous-wave (c.w.) laser interferometer measures the phase of optical wavelengths to achieve sub-nanometre resolution[13–15]. However, measurements are limited to relative range changes as the ambiguity range equals half the laser wavelength. Alternatively, laser radar (LIDAR) measures distance through pulsed or radio-frequency (rf)-modulated waveforms. (For pulsed systems, one simply measures the time-of-flight.) These systems offer large ambiguity ranges but with ~50–100 μm resolution[12,16–18].

Multiwavelength interferometry (MWI) combines measurements at several optical wavelengths, which effectively generates a longer 'synthetic wavelength', and therefore a reasonable ambiguity range while maintaining sub-wavelength resolution[19–26]. However, these systems are vulnerable to systematic errors from spurious reflections, and extending the ambiguity range beyond a millimetre can require slow scanning. Nevertheless, with extensive care in minimizing spurious reflections, the MSTAR[27] system has successfully used MWI for sub-micrometre ranging.

Femtosecond optical frequency combs offer an intriguing solution to the intrasatellite ranging problem[28,29]. From the early work by Minoshima and colleagues[18], combs have been incorporated into precision ranging systems using the various approaches discussed above[23–26,30–33]. In particular, the comb output has been used directly in several experiments to take advantage of its coherence in both the rf and optical domains[27,33,34]. Building on this earlier work, we demonstrate here a comb-based coherent LIDAR that provides a unique combination of precision, speed and large ambiguity range.

Results

Measurement concept. In this work the pulsed nature of a comb is combined with the coherence of the carrier, allowing for a time-of-flight measurement simultaneously with an interferometric measurement based on carrier phase[30,33,34]. We implement this approach with dual coherent frequency combs and achieve a nanometre level of precision with an ambiguity range of 1.5 m in 60 ms at low light levels and with high immunity to spurious reflections. The ambiguity range is easily extended to 30 km. Finally, the time-resolved signal also permits measurements between multiple reference planes in a single beam path. This host of features is unavailable in any other single system.

Our approach follows the footprint of MSTAR as well as related spectroscopy work[35–40], in that we use of a pair of stabilized femtosecond laser frequency combs having pulse trains of slightly different repetition periods (T_r and $T_r - \Delta T_r$). In Fig. 1, we focus on the time-domain picture. One comb serves as the 'signal' source and

National Institute of Standards and Technology, 325 Broadway M.S. 815 Boulder, Colorado 80305, USA. *e-mail: ian@nist.gov; nnewbury@boulder.nist.gov

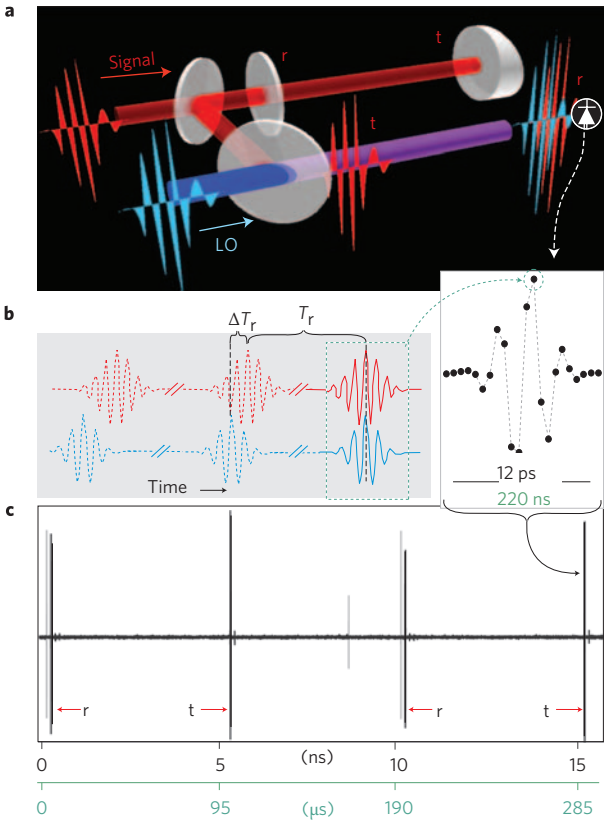

Figure 1 | Ranging concept. a, A high-repetition-rate 'signal' source transmits pulses that are reflected from two partially reflecting planes (glass plates): the reference (r) and the target (t). The reference is a flat plate and yields two reflections, the first of which is ignored. Distance is measured as the time delay between the reflections from the back surface of the reference flat and the front of the target. **b**, The signal pulses are detected through linear optical sampling against a local oscillator (LO). The LO generates pulses at a slightly different repetition rate. Every repetition period (T_r), the LO pulse 'slips' by ΔT_r relative to the signal pulses, and samples a slightly different portion of the signal. Consecutive samples of the overlap between the signal and LO yield a high-resolution measurement of the returning target and reference pulses. Actual data are shown on the right side, where each discrete point corresponds to a single digitized sample and only the immediate overlap region is shown. **c**, The measured voltage out of the detector in both real time (lower scale) and effective time (upper scale) for a target and reference plane separated by 0.76 m. A full 'scan' of the LO pulse across the signal pulse is accomplished every ~200 μs in real time and every ~10 ns in effective time. Two such scans are shown to illustrate the fast, repetitive nature of the measurement. Also seen are two peaks in grey which are spurious reflections of the launch optics.

samples a distance path defined by reflections off a target and reference plane. The second comb serves as a broadband local oscillator (LO), and recovers range information in an approach equivalent to linear optical sampling[41,42] (that is, a heterodyne cross-correlation between the signal and LO). The heterodyne detection provides shot-noise limited performance so that even weak return signals can be detected and the information in the carrier phase is retained. Similar to a down-sampling oscilloscope, measurements can be made with slow detectors and electronics (50–100 MHz) and are easily mapped back into the original femtosecond timescale. An entire scan of the signal return, shown in Fig. 1c, is completed every $T_{update} = T_r^2/\Delta T_r$. For our experiment the two frequency combs operate at repetition rates of 100.021 and 100.016 MHz, giving $T_r \approx 10$ ns, $T_{update} = 1/5{,}190$ Hz ≈ 200 μs

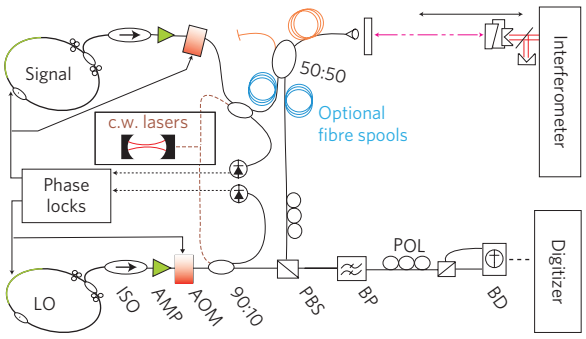

Figure 2 | Schematic of the experimental set-up. Two erbium fibre frequency combs are each phase-locked to two c.w. reference lasers at 1,535 and 1,550 nm (ref. 38). For each laser an intercavity piezo-electric transducer and external acousto-optic modulator (AOM) provide modulation for one lock, and pump current modulation is sufficient for the second. A c.w. interferometer is used to monitor the relative target position. The signal pulse trains are combined with the LO on a polarizing beamsplitter (PBS), optically filtered with a 3-nm bandpass (BP) at 1,562 nm, directed to a balanced detector (BD), and finally digitized at 14 bits synchronously with the LO. The total detected signal power per reflection is ~0.4 μW, or 4 fJ per pulse. ISO, isolator; AMP, erbium fibre amplifier; POL, polarization control; 90:10 and 50:50 are splitter ratios. Optional (1.14-km) fibre spools are included in two configurations, matched pairs (blue) and bidirectional (orange).

and $\Delta T_r \approx 0.5$ ps. A 3-nm bandpass filter limits the transmitted optical bandwidth to much less than $1/(4\Delta T_r)$ in order to meet the Nyquist condition for sampling (discussed later). Figure 2 shows a detailed schematic.

Given the digitized signal in Fig. 1c, the distance between target and reference reflections is calculated by the use of Fourier processing. Mathematically, the LO and signal electric field pulse trains are $\sum_n e^{in\theta_{LO}} E_{LO}(t - nT_r)$ and $\sum_n e^{in\theta_S} E_S(t - n(T_r - \Delta T_r))$, respectively, where $E_{LO(S)}$ is the electric field of a single pulse, n is the pulse index and $\theta_{LO(S)}$ is the carrier-envelope offset phase. For the nth pulse the detected voltage signal is proportional to the temporal overlap between the LO and delayed signal pulses, given by $V(t_{eff}) = \int E^*_{LO}(t)[E_S(t + t_{eff} - \tau_r) + e^{i\psi} E_S(t + t_{eff} - \tau_t)]dt$, where the effective time is $t_{eff} = n\Delta T_r$, ψ accounts for the π differential phase shift upon reflection as well as the relative Gouy phase, τ_r and τ_t are the delays on the reference and target pulses, respectively, and we assume for simplicity that $\theta_{LO} = \theta_S$. To find the relative delay $\tau = \tau_t - \tau_r$ between the target and reference reflection peaks in Fig. 1c, we time-window the separate contributions to $V(t_{eff})$ from the reference and target(s) to find $V^r(t_{eff})$ and $V^t(t_{eff})$. The Fourier transforms of the two are simply related by $\tilde{V}^t(\nu) = e^{i\varphi(\nu) + i\psi} \tilde{V}^r(\nu)$, with the relative spectral phase of $\varphi(\nu) = 2\pi\tau\nu$. Converting from τ to measured distance L, and including the dispersion of the air path, gives the relative spectral phase

$$\varphi(\nu) = 4\pi L/\lambda_c + (4\pi L/v_{group})(\nu - \nu_c) \quad (1)$$

where ν_c is the carrier frequency, v_{group} is the group velocity at the carrier frequency, and λ_c is the carrier wavelength, calculated at measured atmospheric conditions[43].

A simple linear fit $\varphi = \varphi_0 + b(\nu - \nu_c)$ gives the time-of-flight measurement through $L_{tof} = b(v_{group}/4\pi)$ and the high-precision interferometric distance measurement through $L_{int} = (\varphi_0 + 2\pi m)(\lambda_c/4\pi)$. The $2\pi m$ ambiguity reflects the inherent $\lambda_c/2$ range ambiguity in any interferometric measurement. From equation (1) it is clear the system is identical to MWI with many simultaneously transmitted wavelengths (equal to the number of transmitted comb lines).

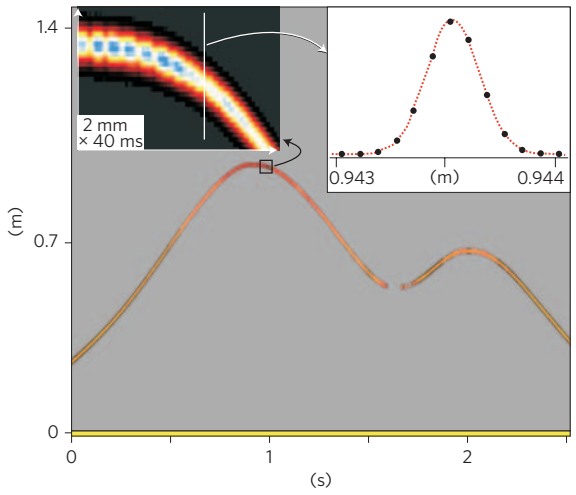

Figure 3 | Real-time image of the range versus time for a moving target (shown in false colour). Every 200 μs, the system scans the entire 1.5-m ambiguity range of the system. Sequential scans are stacked horizontally to yield an image tracking the target motion. The signal at zero distance is the reference plane, and the moving signal represents the target. The upper left inset shows an expanded view where the discrete nature of the sampling is visible. The upper right inset shows a cross-section of the return signal (magnitude squared of the detected electric field). The signal width is set by the 0.42 THz signal $1/e^2$ bandwidth.

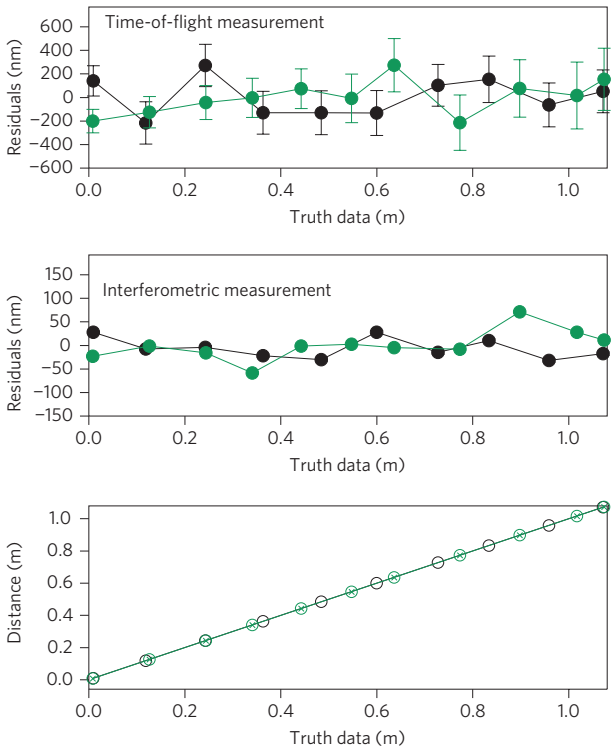

Figure 4 | Residuals of the measured time-of-flight and interferometric range measurements versus truth data from a commercial c.w. interferometer. The averaging period is 60 ms. Error bars are the standard deviation of the mean over the 60-ms period. Data taken with the fibre spool delay line are shown in black, and data without the spool are shown in green; as seen, the addition of the fibre delay has a negligible effect on the measurement. Although the interferometric data are much quieter, they become meaningful only when combined with the time-of-flight data to resolve the 780-nm range ambiguity.

This approach is robust to systematic shifts for several reasons. First and most importantly, the time gating eliminates shifts due to spurious reflections outside of the ±30 ps (±4.5 mm) range window, which can be seen, for example, in Fig. 1c at 8.5 ns and shortly after the reference and target returns. In standard MWI, these spurious reflections are a significant systematic error, because the measured range is effectively a weighted average of all returns. (Either polarization multiplexing or physically separate beam paths are required for the target and reference in MWI.) Second, there are no assumptions about the particular pulse shape. Third, effects due to dispersion are apparent as deviations in the spectral phase, $\varphi(\nu)$, from a linear slope. Fourth, strong self-consistency checks are possible through comparisons of the time-of-flight measurements centred at different carrier frequencies (by tuning the optical bandpass filter) and of the averaged time-of-flight and interferometric range measurements.

Rapid time-of-flight distance measurements of a moving target. Rapid update rates are important in applications such as formation flying or large-scale manufacturing, where the range information is used within a feedback system to orient the components. In our current configuration, it takes 200 μs to scan the entire 1.5-m ambiguity range, and therefore it is possible to capture the motion of a moving target, as is shown in Fig. 3, where sequential 200-μs traces are placed side by side to map the position of a moving target. A Hilbert transform is used to show only the magnitude squared (intensity) of the detected signal. From the time-of-flight, the absolute distance between the reference and target can be determined to within 3 μm for each trace (see Fig. 5 later). Note the dropout of information at ∼1.6 s due to misalignment of the moving cart; for a standard c.w. interferometer with a range ambiguity of one wavelength, such a dropout would ruin the measurement, but here the system easily reacquires the absolute range. An object that moves out of the ambiguity range could be tracked with a simple unwrapping algorithm that should allow one to track an object moving as fast as 3,700 m s^{-1}.

High-precision absolute distance measurements using both time-of-flight and interferometric range measurements. For slowly moving targets, we can average down the time-of-flight measurement sufficiently to hand over to the more precise interferometric range measurement, as described after equation (1). We conducted a series of experiments to demonstrate this capability by comparing the results to 'truth' data supplied by a standard fringe counting interferometric distance meter[13]. In the first experiment, we recorded the reference-to-target distance at discrete steps over a ∼1 m track. In satellite-to-satellite positioning the measurement could be at a range of a kilometre or longer. We therefore conducted two additional experiments with a fibre spool to extend the measurement range. Unfortunately, unlike space, optical fibre is nonlinear, dispersive, birefringent and backscatters the incident light. To counter nonlinearities, we simply chirped the outgoing signal pulse (necessary in any case for chirped-pulse amplification). To counter the dispersive effects, we included ∼700 m of higher-dispersion fibre at the output of the LO laser but within the phase-locked loop, so that the effective delay on the two comb outputs remained, but their relative dispersion was approximately equal at the detector. The most important remaining effect was Rayleigh backscatter from the outgoing pulse, because it cannot be time-gated from the signal. In one experiment, we avoided this problem by using two identical ∼1.14-km spools—one for the outgoing and one for the return signal—and measured the reference-to-target distance at the end of the 1.14-km fibre delay. These data mimic those needed to make remote measurements of

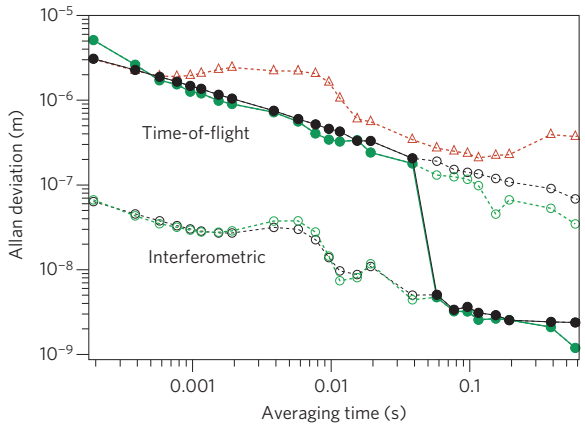

Figure 5 | Precision (Allan deviation) of the distance measurement versus averaging time. Three different measurements are shown: (i) an ~1 m reference-to-target distance without any fibre delay (black circles), (ii) an ~1 m reference-to-target distance with a 1.14-km fibre delay (green circles) and (iii) an ~1.14 km distance across a bidirectional fibre spool (red triangles). The Allan deviation is evaluated over a 5-s data run that is composed of a series of individual data points at the 200 μs update rate. For both reference-to-target distance measurements (with and without the fibre delay), both the time-of-flight and interferometric measurements are given. Solid circles show the experimental precision, which experiences a significant jump around 60 ms when the time-of-flight measurement is sufficiently stable compared to $\lambda_c/4$ and can be combined with the interferometric measurement. At shorter averaging times the interferometric data are still available, but provide only relative position information. For the 1.14-km distance measurement across the bidirectional fibre spool (red triangles), the precision of the time-of-flight distance is scaled to the group velocity of air. In this case, the uncertainty is dominated by actual length changes in the fibre and a 300-nm flicker floor from Rayleigh backscatter.

the pointing of a satellite, or the angle of a machined surface, through trilateration.

As shown in Fig. 4, we found no difference in system performance for the reference-to-target distance measurements with and without the 1.14-km fibre delay. For both our data and the truth data, the range was calculated for identical atmospheric conditions (air temperature, pressure and humidity) so that they shared a common $\sim 1 \times 10^{-7}$ uncertainty from variations in the atmospheric conditions[13]. An independently measured 1-μm drift in the air path (due to temperature change) was subtracted out of the data. At 60 ms averaging, the statistical error on the time-of-flight measurement was below 200 nm, with a systematic error evaluated at less than 100 nm. Because this uncertainty is below $\pm\lambda_c/2$, the distance measurement could be handed over to the interferometric range measurement, which had only a 20–30 nm scatter versus the truth data, consistent with the dominant uncertainty calculated from the estimated ~0.1 °C temperature variations between the two air paths[43] (see Fig. 2).

Figure 5 shows the precision of both the time-of-flight and interferometric measurements versus averaging time. Both with and without the fibre delay, the precision of the time-of-flight distance is $\sigma_{tof} = 3\ \mu m\ (T_{update}/T)^{1/2}$, where T is the averaging period. This scatter is about twice that expected from the measured white noise on the signal and results from ~20 fs residual timing jitter between the combs. The precision of the interferometric distance is roughly $\sigma_{int} = 100\ nm\ (T_{update}/T)^{1/2}$, reaching 5 nm at 60 ms and continuing to drop below 3 nm at 0.5 s. It is limited by the residual carrier phase jitter between the combs. For both range measurements, tighter phase-locking or post-correction of the data from monitoring of the error signals will improve the precision[40,44,45].

Finally, in a third experiment, we replaced the dual fibre spools with a single, bidirectional spool and measured the delay between a reference reflection before the 1.14-km fibre spool and the target. The relative uncertainty, also shown in Fig. 5, is limited by Rayleigh backscattering, which gave rise to a 'flicker' noise floor of ~300 nm, which was too large to permit a confident 'handover' to the interferometric range measurement. At longer times, the uncertainty increases due to actual ~1 μm s^{-1} fibre length changes from temperature effects.

The comb repetition rate of $T_r^{-1} \approx 100$ MHz sets the ambiguity range of our system to $R_A = T_r\, v_{group}/2 = 1.5$ m, adequate for most practical situations, but clearly lower than the fibre delay, equivalent to 1.8 km of air. To remove this ambiguity, we switched the roles of the signal and LO lasers and used the Vernier effect. Because of the difference in repetition rates, a distance measured normally and a second distance measured with the lasers switched differs by $m\Delta R_A$, where $\Delta R_A = \Delta T_r\, v_{group}/2$ is the difference in ambiguity ranges, and m is an integer giving the number of ambiguity ranges by which the true distance exceeds R_A. Therefore, with the two measurements, we can find m and resolve any ambiguity up to the now larger ambiguity range of $v_{group}/(2\Delta f_r) = 30$ km, where $\Delta f_r = (T_{update})^{-1} \approx 5$ kHz is the difference in comb repetition rates . Applying this technique to the fibre spool we measured a fibre length of 1,139.2 m, in good agreement with a standard optical time-domain reflectometry measurement (using the same group index) of 1,138.4 ± 1 m.

The limit to the fractional accuracy in the time-of-flight and interferometric range measurements is ultimately the fractional accuracy in the rf timebase and optical frequency, respectively. Here, we rely on an rf time base (hydrogen maser) that can support better than 1×10^{-13} fractional ranging resolution, that is, 3 nm in 30 km or below the systematic uncertainty. The fractional accuracy of the carrier frequency will depend on the underlying c.w. reference laser, which can be stabilized to a calibrated reference cavity, a molecular reference, or a self-referenced frequency comb[46,47]. (Here, we stabilized the carrier frequency to a reference cavity with ~30 kHz wander and monitored the exact frequency with a self-referenced frequency comb.) The fractional accuracy provided by a reference cavity or molecular reference is sufficient for nanometre-scale measurements at short ranges, or for differential range measurements at long ranges. Nanometre-scale absolute ranging at long distances would require a fully self-referenced comb[46], with its significant added technical complexity. Of course, for extreme precision at very long ranges, the entire system could be based on an optical clock[47], providing an increase of greater than 1×10^4 in accuracy, with effectively unlimited operation distances.

Discussion

The data above illustrate the ability of this system to measure the range between multiple reflections over a large range window (ambiguity range) at a short update rate and at long ranges. Equally important are the built-in checks on hidden systematics by comparing time-of-flight and interferometric range measurements. Although the detection and processing is straightforward, the clear technical challenge lies in the dual, coherent frequency comb sources, particularly for satellite applications. Optical frequency combs have been proposed previously for future space missions using optical clocks, but current combs remain mainly laboratory instruments, albeit with continued progress in environmentally robust fibre-based combs[46,48,49]. Fortunately, the comb source requirements here are simpler in two regards than those for the fully self-referenced octave-spanning combs needed to support current optical clocks. First, although the combs are phase-locked to hertz-level linewidths here, the absolute linewidth actually need only be below Δf_r to cover the full 1.5-m ambiguity range.

(Narrower linewidths are required only for extremely long-range operation beyond $v_{group}/\Delta f_r \approx 30$ km.) Second, the comb output need only span ~10–20 nm optical bandwidth rather than a full octave. Nevertheless, significant engineering will be required to space-qualify such a system. We do note that the basic technique is not limited to fibre-based mode-locked lasers, and other passively mode-locked lasers[50] may provide a route to a more robust and compact system.

As stated earlier, for either large-scale manufacturing or formation flying, it is often the angle or pointing of a target object that is most critical[12]. The pitch and yaw of the object can be determined through trilateration, where the angle is calculated from the distance to several reference points spanning the target. Our approach is well suited to carrying out this measurement, because the time gating of multiple reflections allows one to collect and process data for all trilateration reference points on the same photodiode and digitizer, saving both space and power. The wide ambiguity range and high update rate can support rapid reconfiguration of the target objects.

For active stabilization of absolute distances, or pointing angles, it would be beneficial to improve the time-of-flight measurement to below $\lambda_c/4$ in a single scan so that interferometric precision could be reached in a single update time, T_{update}. The time-of-flight measurement uncertainty will improve by increasing the signal pulse bandwidth up to the available ~4 THz source bandwidth (assuming a corresponding reduction in the residual comb jitter). However, the pulse bandwidth BW is constrained by the relationship $BW < T_{update}/2T_r^2$ (to achieve adequate sampling), so a larger bandwidth implies a lower update rate. This constraint can be removed by coherently combining multiple detection channels at different wavelength bands across the source. With this approach, nanometre-level precision should be possible at less than a millisecond update rate.

In conclusion, frequency comb based LIDAR offers a host of powerful features—precision, stability, speed, large-range ambiguity, low light level operation, multiplexing capabilities, flexibility and spurious reflection immunity—that, as a whole, are unavailable in existing approaches.

Methods

The linear optical sampling scheme presented here is relatively straightforward, but contains a few technical subtleties. In our linear optical sampling picture, signal and LO pulses arrive at the detector at a rate of ~100 MHz and with varying delays between them. The signal and LO pulse overlap is integrated over the detector response time (~1/100 MHz) to yield a single voltage, which is then synchronously digitized with the LO repetition rate. Sampling is done with a 110 MHz balanced detector that allows us to suppress amplitude noise in the relatively high power LO. To eliminate detector ringing effects, the signal is low-pass filtered at 50 MHz (which also eliminates any nonsensical signal above the Nyquist frequency set by the LO sampling rate). Once the signal and LO are combined on the same detector, the measurement is insensitive to electronic phase shifts as long as the system remains linear. Saturation of detectors and amplifiers is carefully avoided.

For time-of-flight distance measurements with resolution smaller than 200 nm, a few pitfalls arise. In virtual time, the LO samples the signal laser $T_r/\Delta T_r = 19{,}260$ times per signal repetition period, T_r. This gives an effective sample step size of 78 μm. For ease in processing one might be tempted to set up the system so that after every 19,260 samples the signal and the LO have the same phase. However, systematics related to the pulse shape limit our ability to measure the centre of our peaks below a precision of 300 nm with a 78-μm step size. Instead we arrange our phase locks so that the pulses overlap every 19,260 × 51 samples. Averaging sequential frames then allows us to effectively subdivide the 78-μm step size by 51, which is sufficient to achieve sub-100-nm resolution. It was also found that the use of interleaved ADCs (analog-to-digital converters) in the digitizer can lead to 100-nm-level scatter in the data. Fortunately, 100 MHz single ADC digitizers are now widely available.

For the interferometric measurement, we must account for the phase factor ψ, defined in the text as $\psi = \pi + \varphi_{Gouy}$. The factor π arises from the reflection from the air–glass interface at the target. The reference pulse occurs from a glass–air interface and suffers no such phase shift. The Gouy phase shift is dependent on the actual distance and we use a separate measurement of the beam Rayleigh range to calculate this phase shift from the time-of-flight distance data.

In our experiment, the processing is not real time. Rather, we collect the raw data and post-process it on a PC. The processing is done on a 'scan-by-scan' basis. The 19,260 data points from each ~200-μs-long scan are first high-pass-filtered at 5 MHz and then searched for the three largest peaks, the first two of which are from the front and back surfaces of the reference flat and the last one from the target. Two copies of the data are then generated: one with a 60-ps time window (the exact width is not important) around the appropriate reference reflection and one with a 60-ps time window about the target reflection. The 19,260 data points are truncated to a length that has only low numbers in its prime factorization (for example, 19,200) and fast Fourier transformed (FFT). The spectral phase is extracted from the FFT and fit across ~0.4 THz of bandwidth to equation (1) and further processed as described in the text. The most computationally intensive operation is the FFT, and real-time processing of the data should be possible with modern field programmable gate arays.

Received 10 December 2008; accepted 21 April 2009; published online 24 May 2009

References

1. Cash, W., Shipley, A., Osterman, S. & Joy, M. Laboratory detection of X-ray fringes with a grazing-incidence interferometer. *Nature* **407,** 160–162 (2000).
2. White, N. X-ray astronomy—Imaging black holes. *Nature* **407,** 146–147 (2000).
3. Gendreau, K. C., Cash, W. C., Shipley, A. F. & White, N. MAXIM Pathfinder X-ray interferometry mission. *Proc. SPIE—Int. Soc. Opt. Eng.* **4851,** 353–364 (2003).
4. ESA. XEUS: X-ray evolving-universe spectroscopy. *ESA CDF Study Report* **CDF-31(A),** 1–237 (2004).
5. Fridlund, M. Future space missions to search for terrestrial planets. *Space Sci. Rev.* **135,** 355–369 (2008).
6. Fridlund, C. V. M. Darwin-the infrared space interferometry mission. *ESA Bulletin* **103,** <http://www.esa.int/esapub/bulletin/bullet103/fridlund103.pdf> 20–25 (2000).
7. Lawson, P. R. & Dooley, J. A. Technology plan for the terrestrial planet finder interferometer. *Publ. Jet Propulsion Laboratory* **05–5,** 1–149 (2005).
8. Coroller, H. L., Dejonghe, J., Arpesella, C., Vernet, D. & Labeyrie, A. Tests with a Carlina-type hypertelescope prototype. *Astron. Astrophys.* **426,** 721–728 (2004).
9. Lemmerman, L. *et al.* Earth science vision: platform technology challenges. Scanning the present and resolving the future. *Proc. IEEE 2001 International Geoscience and Remote Sensing Symposium* (2001).
10. Turyshev, S. G. & Shao, M. Laser astrometric test of relativity: Science, technology and mission design. *Int. J. Mod. Phys. D* **16,** 2191–2203 (2007).
11. Turyshev, S. G., Lane, B., Shao, M. & Girerd, A. A search for new physics with the BEACON mission. Preprint at <http://arxiv:0805.4033v1> (2008).
12. Estler, W. T., Edmundson, K. L., Peggs, G. N. & Parker, D. H. Large-scale metrology—an update. *CIRP Ann. Manuf. Technol.* **51,** 587–609 (2002).
13. Bobroff, N. Recent advances in displacement measuring interferometry. *Meas. Sci. Technol.* **4,** 907–926 (1993).
14. Nagano, S. *et al.* Displacement measuring technique for satellite-to-satellite laser interferometer to determine Earth's gravity field. *Meas. Sci. Technol.* **15,** 2406–2411 (2004).
15. Pierce, R., Leitch, J., Stephens, M., Bender, P. & Nerem, R. Inter-satellite range monitoring using optical inteferometry. *Appl. Opt.* **47,** 5007–5019 (2008).
16. Beck, S. M. *et al.* Synthetic aperture imaging LADAR: laboratory demonstration and signal processing. *Appl. Opt.* **44,** 7621–7629 (2005).
17. Lucke, R. L., Richard, L. J., Bashkansky, M., Reintjes, J. & Funk, E. E. Synthetic aperture ladar. *Naval Research Laboratory, FR 7218–02-10,051* 1–28 (2002).
18. Minoshima, K. & Matsumoto, H. High-accuracy measurement of 240-m distance in an optical tunnel by use of a compact femtosecond laser. *Appl. Opt.* **39,** 5512–5517 (2000).
19. Dandliker, R., Thalmann, R. & Prongue, D. Two-wavelength laser interferometry using superheterodyne detection. *Opt. Lett.* **13,** 339–341 (1988).
20. Williams, C. C. & Wickramasinghe, H. K. Absolute optical ranging with 200-nm resolution. *Opt. Lett.* **14,** 542–544 (1989).
21. Stone, J. A., Stejskal, A. & Howard, L. Absolute interferometry with a 670-nm external cavity diode laser. *Appl. Opt.* **38,** 5981–5994 (1999).
22. Yang, H. J., Deibel, J., Nyberg, S. & Riles, K. High-precision absolute distance and vibration measurement with frequency scanned interferometry. *Appl. Opt.* **44,** 3937–3944 (2005).
23. Schuhler, N., Salvade, Y., Leveque, S., Dandliker, R. & Holzwarth, R. Frequency-comb-referenced two-wavelength source for absolute distance measurement. *Opt. Lett.* **31,** 3101–3103 (2006).
24. Salvade, Y., Schuhler, N., Leveque, S. & Le Floch, S. High-accuracy absolute distance measurement using frequency comb referenced multiwavelength source. *Appl. Opt.* **47,** 2715–2720 (2008).
25. Jin, J., Kim, Y.-J., Kim, Y. & Kim, S.-W. Absolute length calibration of gauge blocks using optical comb of a femtosecond pulse laser. *Opt. Express* **14,** 5968–5974 (2006).
26. Fox, R. W., Washburn, B. R., Newbury, N. R. & Hollberg, L. Wavelength references for interferometry in air. *Appl. Opt.* **44,** 7793–7801 (2005).

27. Lay, O. P. *et al.* MSTAR: a submicrometer, absolute metrology system. *Opt. Lett.* **28,** 890–892 (2003).
28. Hänsch, T. W. Nobel Lecture: Passion for precision. *Rev. Mod. Phys.* **78,** 1297–1309 (2006).
29. Hall, J. L. Nobel Lecture: Defining and measuring optical frequencies. *Rev. Mod. Phys.* **78,** 1279–1295 (2006).
30. Ye, J. Absolute measurement of long, arbitrary distance to less than an optical fringe. *Opt. Lett.* **29,** 1153–1155 (2004).
31. Joo, K.-N. & Kim, S.-W. Absolute distance measurement by dispersive interferometry using a femotsecond pulse laser. *Opt. Express* **14,** 5954–5960 (2006).
32. Swann, W. C. & Newbury, N. R. Frequency-resolved coherent lidar using a femtosecond fiber laser. *Opt. Lett.* **31,** 826–828 (2006).
33. Joo, K. N., Kim, Y. & Kim, S. W. Distance measurements by combined method based on a femtosecond pulse laser. *Opt. Express* **16,** 19799–19806 (2008).
34. Newbury, N. R., Swann, W. C. & Coddington, I. Lidar with femtosecond fiber-laser frequency combs. *14th Coherent Laser Radar Conference* (Snowmass, Colorado, 2007).
35. Keilmann, F., Gohle, C. & Holzwarth, R. Time-domain and mid-infrared frequency-comb spectrometer. *Opt. Lett.* **29,** 1542–1544 (2004).
36. Schiller, S. Spectrometry with frequency combs. *Opt. Lett.* **27,** 766–768 (2002).
37. Yasui, T., Kabetani, Y., Saneyoshi, E., Yokoyama, S. & Araki, T. Terahertz frequency comb by multifrequency-heterodyning photoconductive detection for high-accuracy, high-resolution terahertz spectroscopy. *Appl. Phys. Lett.* **88,** 241104 (2006).
38. Coddington, I., Swann, W. C. & Newbury, N. R. Coherent multiheterodyne spectroscopy using stabilized optical frequency combs. *Phys. Rev. Lett.* **100,** 013902 (2008).
39. Schlatter, A., Zeller, S. C., Pashcotta, R. & Keller, U. Simultaneous measurement of the phase noise on all optical modes of a mode-locked laser. *Appl. Phys. B* **88,** 385–391 (2007).
40. Giaccari, P., Deschenes, J.-D., Saucier, P., Genest, J. & Tremblay, P. Active Fourier-transform spectroscopy combining the direct RF beating of two fiber-based mode-locked lasers with a novel referencing method. *Opt. Express* **16,** 4347–4365 (2008).
41. Dorrer, C., Kilper, D. C., Stuart, H. R., Raybon, G. & Raymer, M. G. Linear optical sampling. *IEEE Photon. Technol. Lett.* **15,** 1746–1748 (2003).
42. Dorrer, C. High-speed measurements for optical telecommunication systems. *IEEE J. Quantum Electron.* **12,** 843–858 (2006).
43. Ciddor, P. E. & Hill, R. J. Refractive index of air. 2. Group index. *Appl. Opt.* **38,** 1663–1667 (1999).
44. Telle, H. R., Lipphardt, B. & Stenger, J. Kerr-lens, mode-locked lasers as transfer oscillators for optical frequency measurements. *Appl. Phys. B* **74,** 1–6 (2002).
45. Stenger, J., Schnatz, H., Tamm, C. & Telle, H. R. Ultraprecise measurement of optical frequency ratios. *Phys. Rev. Lett.* **88,** 073601 (2002).
46. Newbury, N. R. & Swann, W. C. Low-noise fiber laser frequency combs. *J. Opt. Soc. Am. B* **24,** 1756–1770 (2007).
47. Rosenband, T. *et al.* Frequency ratio of Al^{+} and Hg^{+} single-ion optical clocks; metrology at the 17th decimal place. *Science* **319,** 1808–1812 (2008).
48. Hartl, I., Imshev, G., Fermann, M. E., Langrock, C. & Fejer, M. M. Integrated self-referenced frequency-comb laser based on a combination of fiber and waveguide technology. *Opt. Express* **13,** 6490–6496 (2005).
49. Baumann, E. *et al.* A high-performance, vibration-immune fiber-laser frequency comb. *Opt. Lett.* **34,** 638–640 (2009).
50. Koch, B. R., Fang, A. W., Cohen, O. & Bowers, J. E. Mode-locked silicon evanescent lasers. *Opt. Express* **15,** 11225–11233 (2007).

Acknowledgements

The authors acknowledge technical assistance from C. Nelson and D. Nickel, as well as very helpful discussions with T. Fortier, D. Braje, N. Ashby, I. Bakalski, P. Bender, M. Foster, R. Holzwarth, J. Leitch, A. Newbury, R. Reibel, P. Roos, M. Stephens, J. Stone, C. Wiemer and P. Williams.

Author contributions

I.C., W.C.S. and N.R.N. contributed equally to this work. L.N. assisted with the data analysis.

Additional information

Reprints and permission information is available online at http://npg.nature.com/reprintsandpermissions/. Correspondence and requests for materials should be addressed to I.C. and N.R.N.

Optical fibre splicers

Convenient and reliable joining of optical fibres is essential for building optical networks. **Neil Savage** reports that the machines performing the task are becoming smaller and increasingly sophisticated.

The world is becoming more data-intensive all the time, as consumers download movies to their home computers, businesses replace paper with electronic files, and the appetite for e-mail and online blogs continues to grow. Regardless of the specific application, moving a lot of data around the globe means deploying long fibre-optic networks, and the requirement for optical fibres to be joined together by a process known as splicing.

To join fibres permanently, installers rely on instruments called fusion splicers, which carefully align the cores of two separate fibres and then heat them by an arc-welding process to make them into one. Tolerances are tight, as the cores of single-mode fibres are just a few micrometres across, and splices must be accurate so that little light is lost at the joint. For a splicer to be practical it needs to be rugged, portable, reliable and easy to use.

"They [installers of optical fibre networks] want to have something small and lightweight so they can just walk up, make the splice, and go on to the next," says Daniel Spann, an applications specialist in engineering services for splicers at Corning Cable Systems. The increased deployment of fibre-to-the-home networks, such as Verizon's FiOS offering, is driving the demand for smaller splicers, he says. At the same time, manufacturers are adding features to measure and record alignment data, so that users can demonstrate that the splices meet specifications. And Spann says that more and more users are relying on active alignment systems, which use a built-in camera to image the fibres and make sure that they are positioned correctly in the x, y and z axes before splicing. Such schemes tend to be more accurate than passive alignment, in which fibres are simply slotted into V-shaped grooves and then assumed to be in the correct position for splicing.

Larry Wesson, president of Aurora Optics, says that his company is seeing growing demand from military and aerospace builders, as they incorporate more sensors, communication and computing into vehicles ranging from aeroplanes to tanks. Military users may need to combine data from Global Positioning System and weather satellites with video from battlefield situations and real-time analysis from combat computers. "The Army and the Air Force and the Marines need something that can be carried in backpacks to some remote desert location and brought out like a pair of pliers," Wesson says.

In response, splicer manufacturers are miniaturizing their devices, improving packaging to make them more robust and looking for materials that can withstand harsh environments, temperature fluctuations and electromagnetic interference. Of course, says Wesson, these improvements must be balanced against the other imperative for all customers: keeping the cost down.

PRODUCT ROUND-UP

Ericsson (Stockholm, Sweden) offers the FSU 995 series of fusion splicers for industrial applications. The devices come with features such as thin-core alignment, negative index matching and automatic arc re-centring. The splicers operate at temperatures from 0 °C to –40 °C in relative humidities from 0% to 95%. All three splicers in the series are capable of splicing erbium fibres commonly used in optical fibre amplifiers. Each also comes with a communications package to interface with a personal computer and includes software that allows users to upload and download splicing data to a work station. Typical splice loss is 0.02 dB. The FA version for standard factory applications works with all types of single fibres, as does the HS version for high-strength splicing. The PM version can also splice polarization-maintaining fibres, with a polarization extinction ratio estimated at a mean value of 32.2 dB.
www.ericsson.com

Sumitomo Electric (Osaka, Japan) says that its Type-39 FastCat Core Alignment Fusion Splicer features a dual-automatic heater system that allows auto-start heater and auto-start splice functions. According to Sumitomo, the design reduces the bottleneck of 'heater wait time' by 88%. With an individual heater cycle time of only 30 s (when used with 60-mm-long fibre protection sleeves) and a splice cycle of only 9 s, the FastCat significantly improves splicing efficiency time. The FastCat is a fully automatic, portable, self-contained instrument for creating quick low-loss optical fibre splices in any environment with a typical splice loss of 0.02 dB for identical single-mode fibres. It is designed to work with many fibre types including single-mode, multimode, dispersion-shifted and other speciality fibres. The splicer uses precision high-resolution direct core monitoring (HDCM) technology to form repeatable low-loss splice results.
www.sei.co.jp

AURORA OPTICS

The PRO-730 core-alignment fusion splicer from **Precision Rated Optics** (San Francisco, California, USA) is designed for use in various types of fibre deployment, including on-premises, outside plant and fibre-to-the-home. It works with all popular fibre types and in all weather conditions, operating at temperatures from –25 °C to 50 °C, in relative humidity from 0% to 95% and at altitudes from 0 to 5,000 m. The user-programmable device offers automatic

checking of the fibre end face and automatic calibration. It can store data on 8,000 splices, as well as transmitting data to a computer over an RS232 data interface. The splicer's camera provides a view of both the *x* and the *y* axes, and displays images on a colour LCD monitor at ×200 magnification. It handles cladding diameters of 100 to 150 μm and a standard cleave length of 16 mm. Average splice loss is 0.02 dB for single-mode, 0.01 dB for multimode, 0.04 dB for dispersion-shifted and 0.04 dB for non-zero dispersion-shifted fibre.
www.fiberopticpro.com

OFS OPTICS

OFS (Norcross, Georgia, USA), a division of Furukawa, offers the Fitel S184 series of fusion splicers, featuring three-phase plasma technology for high-strength, high-yield, large-diameter and speciality fibre splicing. The design places three electrodes in a 'Y' configuration to produce an arc zone that the company calls "a ring of fire". The configuration provides a useful wide-area plasma field that is up to 100 times larger than a two-electrode arc system with consistent heating throughout the zone, allowing the device to splice large-diameter fibres with low insertion loss. It also allows a thermally expanded core process to be used for fibres with dissimilar mode field diameter, either before or after splicing, to reduce optical loss significantly. The design also produces temperatures stable enough to allow a flame polish after the splice. Similar to an annealing process, the flame polish removes internal stresses and surface imperfections in the silica that were created during the splicing, thereby increasing the tensile strength of the splice.
www.ofsoptics.com

AFL Telecommunications (Duncan, South Carolina, USA), a subsidiary of Fujikura, says that its FSM-60S fusion splicer is ruggedly constructed to resist shock, dust and rain and can withstand a drop of around 75 cm. The machine splices a fibre in 9 s and heats a 60-mm-long protective splice sleeve in 30 s. It offers automatic arc calibration and fibre identification, dual monitor position with automated image orientation, an auto-start tube heater and the ability to recharge the battery during splicer operation. The user can select the fibre clamping method, either sheath clamp or fibre holders. A colour liquid-crystal display with an anti-reflective coating provides visibility even in bright sunlight. The battery can support up to 160 splicing and heating cycles per charge. Included software allows users to download splice data to a personal computer and download video images from the splicer for enhanced technical support.
www.afltele.com

The OptiSplice CDS fusion splicer from **Corning** (Corning, New York, USA) is designed for connecting networks that require low-loss performance, such as long-haul, cable television, telecommunication and local area network applications. It can splice dissimilar and speciality fibres. The device uses a core detection system based on the images obtained by video cameras on the *x* and *y* axes and aligns the cores in three axes in 13 s. The cameras also store the image information, and the device displays a splice loss estimate on completion of the splice. The device can also automatically choose the best alignment method for a given application. The device handles single-mode and multimode fibres with cladding diameter of 125 μm and coating diameters of 250 to 900 μm. It has 21 factory-optimized programs for a variety of fibre types and can store up to 150 user-defined programs. Typical splice loss is under 0.02 dB for similar single-mode fibres, under 0.05 dB for dissimilar fibres and under 0.01 dB for multimode.
www.corning.com

Aurora Optics (Broad Axe, Pennsylvania, USA) calls its MiniMod the world's smallest hand-held, fully automatic, three-axis aligning fusion splicer. The fusion head measures 4.3 × 8.1 × 11.9 cm and weighs 0.5 kg, and the electronics module and display measures 7.6 × 14 × 19 cm and weighs 0.6 kg. It is designed for fibre-to-the-home applications and meets military specifications for ruggedness. In addition to real-time three-axis alignment, it provides fibre-end angle measurement and gross defect detection. It can store the data for up to 10,000 splices and hold 100 different splicing programs. The MiniMod operates in any orientation—horizontal, vertical or even upside down. It handles all standard single-mode and multimode fibre types with core diameters from 3 to 200 μm and cladding diameters of 100 to 140 μm in automatic alignment mode, and up to 250 μm in manual mode. Typical splice loss is 0.03 dB or less on single-mode fibre. It operates at temperatures from –10 °C to 55 °C, at relative humidity from 0 to 95% and at altitudes up to 5,000 m.
www.aurora-optics.com/home.htm

GAO FIBREOPTICS

The 720B single-fibre fusion splicer from **GAO FibreOptics** (Toronto, Ontario, Canada) features a digital colour display with simultaneous *x* and *y* views. It offers a 9-s splice time, with a 40-s protective tube heating time. It automatically checks the fibre-end face and calibrates parameters. Users can input their own splice programs, and the device will store up to 8,000 splice results. It works on a variety of fibres with cladding diameters from 100 to 150 μm and coating diameters from 100 to 1,000 μm, with a standard cleave length of 16 mm. It operates in both automatic and manual splice mode. The device provides average splice loss of 0.02 dB for single-mode, 0.01 dB for multimode, 0.04 dB for dispersion-shifted and 0.04 dB for non-zero dispersion-shifted fibre, with a return loss of >60 dB. It operates at temperatures from -25 °C to 50 °C, at relative humidities from 0 to 95%, and at altitudes to 4,000 m. It can be powered by an a.c. adaptor or an internal battery that provides up to 150 cycles of continuous splice and heat.
www.gaofiberoptics.com

NEIL SAVAGE is a freelance science and technology journalist based in Lowell, Massachusetts, USA.

The mention of a company's name or product is not an endorsement by Nature Photonics, *and* Nature Photonics *takes no responsibility for the accuracy of the product information or the claims made by companies.*

Reflection revisited

Light is often thought to reflect from a flat surface at the same angle at which it is incident. *Nature Photonics* spoke to Han Woerdman about the observation of angular deviations of reflected beams.

Could you tell me about the early history of reflection of light?

The Greek philosophers are thought to be the first known to have invented the concept of a light ray. The law of reflection itself, which is a follow-up of the concept of the ray, dates back to Euclid around 300 BC and his book *Catoptrics*. This work was then translated by Arab philosophers in the early middle ages and that is the way it came to the west. Newton should also be mentioned here, as in Newton's *Opticks* the law of reflection is one of his axioms.

And what happened in more modern times?

In 1943, the two German scientists Goos and Hänchen performed an experiment showing that in total internal reflection a light beam acquires a lateral shift; this can be seen as a positional deviation of the law of reflection. Because of the Second World War, this work was not published until 1947. That was the starting point of much theoretical work, leading to diffractive corrections to ray optics. The Goos–Hänchen was one of them; several others were predicted, including the angular deviation of the law of reflection. The first experimental demonstration thereof, although with a couple of limitations, was done in the microwave domain in 2006 by Nimtz and collaborators.

What was your motivation for the research?

Our work on the angular shift came out of our work on surface-plasmon-assisted transmission of entangled photons through a gold hole array, which appeared in *Nature* in 2002. We wanted to develop a deep understanding of surface plasmon behaviour, so we went back to the case of a uniform surface to study the effect of a non-local response on the optical reflection from gold. This turned out to be far too small an effect to see, but it gave us the motivation to study the exact nature of optical reflection. The general motivation for investigating the effect at shorter wavelengths than microwave is application-associated.

LEIDEN UNIVERSITY

Left to right: Martin van Exter; Han Woerdman; Michele Merano.

Why does the angular deviation in the reflection occur?

The essence is that a 'ray' is an artificial construct that does not exist in real life. Its closest physical implementation is a beam of light. Such a beam can be viewed as a set of plane waves travelling at different angles. If the beam strikes a surface that has a reflectivity that is less than perfect ($R < 100\%$) then you generally have angular dependence of the reflectivity. That is, each of the plane waves experiences a different strength of reflection, which serves to reshape the reflected beam and alter its direction of propagation into the far field. In our setup a beam is reflected by an air–glass interface and its transverse position is measured with a calibrated split detector.

What were the main challenges in performing the experiment?

The optical source was the main issue. We started out with a semiconductor laser as a light source, but this gave poor results. We then used superluminescent light-emitting diodes which gave a big improvement for two reasons. First is that they have low temporal coherence (the bandwidth is 20 nm), which means that the unavoidable reflections in the optical train do not produce optical speckle. The second reason is that the diode has no cavity and has no transverse modes, so the beam pointing stability is better than that of a semiconductor laser.

Another important point is that in some of the experiments we modulate the polarization. It turns out that it is difficult to modulate the polarization without also slightly modulating the position and angle of the beam. We thought that a single-mode fibre as a spatial filter would solve this problem, but it did not guarantee the spatial stability we required. As a result, we turned to a liquid-crystal-based polarization modulator which works well but depolarizes, say, 1% of the light.

What are the implications of your findings?

Although the angular deviation is usually small (typically 10^{-2} to 10^{-5} rad), if you have a detector or a relevant optical component that is many Rayleigh lengths from the beam focus, the effect can become important. Applications in which this effect may come into play include angular metrology in general and cantilever-based surface microscopy. Other applications that come to mind are interferometry, including situations that may arise in the Laser Interferometer Space Antenna (LISA) or the Laser Interferometer Gravitational-wave Observatory (LIGO).

INTERVIEW BY DAVID PILE

Han Woerdman and his team have a Letter on angular deviations of a light beam upon reflection on page 337 of this issue.